

INFORMATION TO USERS

This manuscript has been reproduced from the microfilm master. UMI films the text directly from the original or copy submitted. Thus, some thesis and dissertation copies are in typewriter face, while others may be from any type of computer printer.

The quality of this reproduction is dependent upon the quality of the copy submitted. Broken or indistinct print, colored or poor quality illustrations and photographs, print bleedthrough, substandard margins, and improper alignment can adversely affect reproduction.

In the unlikely event that the author did not send UMI a complete manuscript and there are missing pages, these will be noted. Also, if unauthorized copyright material had to be removed, a note will indicate the deletion.

Oversize materials (e.g., maps, drawings, charts) are reproduced by sectioning the original, beginning at the upper left-hand corner and continuing from left to right in equal sections with small overlaps. Each original is also photographed in one exposure and is included in reduced form at the back of the book.

Photographs included in the original manuscript have been reproduced xerographically in this copy. Higher quality 6" x 9" black and white photographic prints are available for any photographs or illustrations appearing in this copy for an additional charge. Contact UMI directly to order.

UMI

A Bell & Howell Information Company
300 North Zeeb Road, Ann Arbor MI 48106-1346 USA
313/761-4700 800/521-0600



**MICROSTRUCTURE EVOLUTION AND ITS INFLUENCE
ON THERMAL EXPANSION AND TENSILE
PROPERTIES OF THE SUPERALLOY IN738LC
AT HIGH TEMPERATURES**

A Dissertation

**Submitted to the Graduate Faculty of the
Louisiana State University and
Agricultural and Mechanical College
in partial fulfillment of the
requirements for the degree of
Doctor of Philosophy**

in

**The Interdepartmental Program
in
Engineering Science**

by

Ercan Balikci

B.S., Marmara University, Istanbul, Turkey, 1988

M.S., Marmara University, Istanbul, Turkey, 1991

May, 1998

UMI Number: 9836852

**UMI Microform 9836852
Copyright 1998, by UMI Company. All rights reserved.**

**This microform edition is protected against unauthorized
copying under Title 17, United States Code.**

UMI
300 North Zeeb Road
Ann Arbor, MI 48103

ACKNOWLEDGMENTS

I would like to express my gratefulness to Dr. Aravamudhan Raman, my major professor, for his sincere and tenacious supervision in advising me during my doctoral study. I will always consider myself fortunate for having worked under his guidance because of his modest personality and particularly honest scientific approach that he conveyed to me.

I also express my thanks to Dr. R. A. Mirshams of Southern University, Baton Rouge, LA for his contribution to my Ph. D. work, particularly by allowing me to use the very essential equipment available at Southern University.

I am also grateful to Dr. G. Z. Voyiadjis and Dr. S. S. Pang, my minor professors, Dr. E. MA, Dr. H. Wong, and Dr. P. Adams for their help during my study. My thanks are also extended to Dr. Z. X. Li of Lockheed Martin Co., New Orleans, LA for allocating his time for priceless discussions.

I thank NASA's LaSpace Program in the State of Louisiana for extending partial support on this research, Don Larsen of Howmet Corporation, Whitehall, MI, for providing cost consideration for specimens, Drs. P. Rodriguez, S.L. Mannan, and V.S. Raghunathan of Indira Gandhi Center For Atomic Research, Madras, India, for enabling me to spend some time in their laboratories and for carrying out the composition analysis, and Dr. Fogel and Dr. Eaton of LSU for supporting my travel to India for collaborative research and studies.

Thanks are also expressed to Mugla University, Mugla, Turkey and YOK (Higher Education Council of Turkey) for providing financial support during my doctoral studies at LSU.

Finally, the author expresses grateful appreciation to the personnel at HTML of Oak Ridge National Laboratory (ORNL), Oak Ridge, TN for enabling the author use their facilities for carrying out the mechanical tests at 1200°C.

TABLE OF CONTENTS

ACKNOWLEDGMENTS	ii
LIST OF TABLES	vii
LIST OF FIGURES	viii
LIST OF NOMENCLATURE	xiii
ABSTRACT	xiv
CHAPTER	
I. INTRODUCTION	1
I.1. General	1
I.2. Literature Information on the Superalloy IN738LC	3
I.2.1. Microstructure Development.....	3
I.2.2. Texture Development (Preferred Orientation).....	7
I.2.3. Tensile Properties.....	9
I.2.4. Fracture Behavior.....	12
I.2.5. Thermal Expansion Characteristics.....	13
I.3. Objectives of the Present Research	15
II. EXPERIMENTAL	17
II.1. Materials	17
II.2. Microstructure Development and Characterization	17
II.3. High Temperature Tensile Tests	24
II.4. Fractography of the Specimens after the Tensile Tests	25
II.5. Linear Thermal Expansion Tests	25
III. RESULTS AND DISCUSSIONS:	
MICROSTRUCTURE DEVELOPMENT AND CHARACTERIZATION	29
III.1. Microstructure Evolution in Polycrystalline Superalloy	
IN738LC in the Range 650-1120°C	29
III.1.1. Solution Treatments.....	29
III.1.2. Effect of Single and Double Agings on the Microstructure.....	31
III.2. Microstructure Evolution in Polycrystalline Superalloy	
IN738LC in the Range 1120-1250°C	38
III.2.1. Agings after the 1200°C/4h/AAC solution treatments,	
(Type-I).....	40
III.2.2. Agings after the 1200°C/4h/AAC + 1120°C/24h/FC	
heat treatments, (Type-II).....	43
III.2.3. Agings after 1250°C/4h + 1140°C/t/WQ	
heat treatments, (Type-III).....	46

III.2.4.	Agings after 1140°C/4h/WQ + 1160°C/t/WQ heat treatments, (Type-IV).....	46
IV.	RESULTS AND DISCUSSIONS: PRECIPITATE GROWTH/DISSOLUTION MECHANISM AND KINETICS IN IN738LC.....	48
IV.1.	In the Range 650-1120°C.....	48
IV.2.	In the Range 1120-1250°C.....	52
IV.3.	Precipitate Coarsening Mechanisms.....	68
IV.3.1.	The “Precipitate Agglomeration Model (PAM)”.....	81
V.	RESULTS AND DISCUSSIONS: PREFERRED ORIENTATIONS IN THE SUPERALLOY IN738LC.....	86
V.1.	Results.....	86
V.2.	Discussion.....	93
VI.	RESULTS AND DISCUSSIONS: HIGH TEMPERATURE TENSILE PROPERTIES OF POLYCRYSTALLINE SUPERALLOY IN738LC.....	97
VI.1.	In the Range RT-850°C with Various Precipitate Microstructures... 97	97
VI.1.1.	Results.....	98
VI.1.2.	Discussion.....	102
VI.2.	Tensile Properties of Polycrystalline Superalloy IN738LC with the Fine-Size Precipitate Microstructure at 1200°C.....	111
VII.	RESULTS AND DISCUSSIONS: FRACTURE BEHAVIOR OF POLYCRYSTALLINE SUPERALLOY IN738LC.....	114
VII.1.	Results.....	114
VII.2.	Discussion.....	118
VIII.	RESULTS AND DISCUSSIONS: MICROSTRUCTURE EFFECT ON THE THERMAL EXPANSION COEFFICIENT OF POLYCRYSTALLINE IN738LC.....	124
VIII.1.	Results.....	124
VIII.2.	Discussion.....	126
IX.	CONCLUSIONS.....	132
IX.1.	Microstructure Development.....	132
IX.2.	Preferred Orientation.....	136
IX.3.	Tensile Properties.....	137
IX.4.	Fracture Behavior.....	138
IX.5.	Thermal Expansion.....	139
X.	SUGGESTIONS FOR FUTURE WORK IN THIS RESEARCH AREA..	141

REFERENCES	142
VITA	149

LIST OF TABLES

Table 1. Chemical composition of the as-received IN738LC.....	18
Table 2. Heat treatment schedules for the IN738LC.....	19
Table 3. Size of the γ' precipitates in FC and WQ conditions after aging for 24h at the given temperature subsequent to 1200°C/4h solution treatment.....	53
Table 4. Size data of the γ' precipitates after various heat treatments. (size is given in nm).....	53
Table 5. Preferred orientations and lattice parameters of FCC phases in the aged IN738LC alloy specimens.....	88
Table 6. Preferred orientation (PO) data and lattice parameters of $L1_2$ phases in some Ni-aluminide-type alloys deduced from XRD patterns....	92
Table 7. Tensile Properties of IN738LC with various precipitate microstructures.....	100
Table 8. Tensile Properties of IN738LC extracted from plots given in the literature.....	110
Table 9. Grain and precipitate sizes, preferred orientation, experimental elasticity modulus, α , and $d\alpha/dT$ of the microstructures tested.....	127

LIST OF FIGURES

Figure 1. Crystal structure of a) FCC Ni-rich matrix and b) $L1_2$ Ni_3Al	4
Figure 2. Different possible dislocation precipitate interactions [63] a) by-passing and cutting b) cutting.....	10
Figure 3. Micrographs showing the matrix grain morphology in a) radial section b) axial section and c) precipitate microstructure of the as-received IN738LC. Dark regions in (c) are the γ' precipitates (Magnification: a, b; 4X, c; 15kX).....	18
Figure 4. The plot showing the cooling curve that was obtained in the heat treatments under furnace cooling (FC) conditions.....	21
Figure 5. Heating profile used in the thermal expansion tests.....	27
Figure 6. Microstructures after the solution treatment at 1120°C / 2h. (Magnification: 15kX) a) FC-condition b) AC-condition c) AAC-condition d) WQ-condition.....	32
Figure 7. Refined microstructure after 1200°C / (4, 24, 72, 240h) / (AAC, WQ) solution treatment. (Magnification: 15kX).....	32
Figure 8. Effect of single and double aging after 1120°C / 2h / WQ on the microstructure. (Magnification: 15kX a) single aging at 850°C / 24h / FC b) single aging at 750°C / 24h / FC c) double aging at 850°C / 12h + 750°C / 12h / FC).....	33
Figure 9. Microstructures after aging at different temperatures after 1200°C / 4h / AAC. (Magnification: 15kX) a) single aging at 650°C / 24h / FC b) single aging at 750°C / 24h / FC c) single aging at 850°C / 24h / FC d) single aging at 950°C / 24h / FC e) single aging at 1050°C / 24h / FC f1), f2) single aging at 1120°C / 24h / FC.....	35

Figure 10. Microstructures after aging at different temperatures after 1250°C / 4h / AAC. (Magnification: 15kX)		
a) single aging at 950°C / 24h / FC		
b) single aging at 1050°C / 24h / FC		
c) single aging at 1200°C / 24 h / WQ		
d) single aging at 1200°C / 24 h / FC.....	36	
Figure 11. Microstructures after aging at different temperatures after 1200°C /4h / AAC (Magnification: 15kX)		
a) single aging at 850°C / 24h / WQ		
b) single aging at 950°C / 24h / WQ		
c) single aging at 1050°C / 24h / WQ		
d) single aging at 1070°C / 24h / WQ		
e) single aging at 1090°C /24h / WQ		
f) single aging at 1120°C / 24h / WQ		
g) single aging at 1120°C / 48h / WQ.....	37	
Figure 12. Microstructures after different double agings after 1200°C / 4h / AAC (Magnification: 15kX)		
a) double aging at 950°C / 12h + 650°C / 12h / FC		
b) double aging at 950°C / 12h + 750°C / 12h / FC		
c) double aging at 950°C / 12h + 850°C / 12h / FC.....	38	
Figure 13. The duplex-size γ' precipitate microstructure obtained through Type-I heat treatment- 1200°C / 4h / AAC + 1140°C / t / WQ (Magnification: 15kX).		
a) t = 1 min.	b) t = 3 min.	c) t = 5 min.
d) t = 30 min.	e) t = 2h	f) t = 4h
g) t = 12h	h) t = 24h	i) t = 48h
j) t = 96h.....		41
Figure 14. The duplex- size γ' precipitate microstructure obtained after Type-I aging at 1150°C / 24h / WQ subsequent to the solution treatment of 1200°C / 4h / AAC. (Magnification: 15kX).....		42
Figure 15. The duplex-size γ' precipitate microstructure obtained through Type-II heat treatment 1200°C / 4h / AAC + 1120°C / 24h / FC + 1140°C / t / WQ. (Magnification 15kX)		
a) t = 1-3 min.	b) t = 5 min.	c) t = 30 min.
d) t = 2h	e) t = 4h	f) t = 12h
g) t = 24h.....		45

Figure 16. The partially fine precipitate microstructure obtained through Type-II heat treatment 1200°C / 4h / AAC + 1120°C / 24h / FC + 1160°C / t / WQ. t=15, 30, and 60 s. (Magnification: 15kX).....	46
Figure 17. The microstructure obtained through Type-IV heat treatment 1200°C / 4h / AAC + 1140°C / 4h / WQ + 1160°C / t / WQ (Magnification: 15kX) a) t= 15 s b) t= 30 s c1) t= 60 s c2) same specimen as c1 showing different area.....	47
Figure 18. Plot of log(d) vs. 1/T of gamma prime precipitate size derived from Figs. 9&11 and data given in Table 3 (d is average precipitate size after the heat treatment 1200°C/4h/AAC + T/24h/(WQ or FC), where T is the aging temperature)....	50
Figure 19. The plot of precipitate size vs. aging time for Type-I heat treatment at 1140°C, (1200°C/4h/WQ + 1140°C/t/WQ), along with analogous plot of precipitate size data for Type-II heat treatment at 1140°C, (1200°C/4h/WQ + 1120°C/24h/FC + 1140°C/t/WQ).....	54
Figure 20. The plot of log(d) vs. 1/T, derived using the precipitate size data after Type-I heat treatment at 1120, 1140, and 1150oC for 24h/WQ (data given in Table 3 an 4 for the corresponding microstructures).....	55
Figure 21. Micrographs showing the precipitate agglomeration modes. (Magnification: 15kX) a) in the duplex-size precipitate microstructure (1120°C / 2h / AAC + 750°C / 24h / FC) b) agglomeration of adjacent precipitates in single-size precipitate microstructure. (1250°C / 4h / AAC + 1200°C / 24h / FC) c) micrograph showing the agglomeration of smaller precipitates (as in b) and later their coalescence into the bigger ones; also, possible coalescence of the adjacent four coarse precipitates (right top) and of three coarse ones (bottom left) along <100> direction is noticeable.....	70
Figure 22. Plot of log(d) vs. 1/T of γ' size derived from data given in Table 3 and Table 4 for WQ condition (Partially reproduced from Fig. 18).....	76
Figure 23. Plot of Q vs. T, the curve fit is from the best fit curve of Fig. 22 including the data point corresponding to 1140°C.....	76

Figure 24. The plot of d_{cf} vs. T.....	78
Figure 25. Evenly distributed cuboidal precipitates in the matrix. The area encapsulated with dashed lines shows the unit cell used to calculate the spacing (s) between the precipitates.....	78
Figure 26. Plot of s vs. T.....	79
Figure 27. Plot of d vs. s.....	79
Figure 28. Plot of Q_{cf} vs. d_{cf} and s_{cf}	81
Figure 29. Plot of Q_{cf} vs d_{cf}^3	83
Figure 30. XRD patterns of different precipitate microstructures. a) As-received (4 th batch) b) SSS (1 st batch) c) F (1 st batch) d) M (5 th batch) e) C (1 st batch) f) D (1 st batch) g) AD (5 th batch).....	89
Figure 31. Anomalous XRD patterns of different precipitate microstructures. a)SSS (Rpt. 1 st batch), showing {131} and {111} PO b) SSS (5 th batch), showing {200} PO c) F (4 th batch), showing {131} and {220} PO.....	90
Figure 32. Various precipitate microstructures of IN738LC chosen for Tensile testing and thermal expansion studies (Magnification: 15kX). a) fine-size ppts. (F; ~70 nm) b) medium-size ppts. (M; ~450 nm) c) coarse-size ppts. (C; ~700 nm) d) duplex-size ppts. (D; ~50 and 450 nm).....	97
Figure 33. 0.2% offset Yield strength with a) low strain rate ($5 \times 10^{-5} \text{ s}^{-1}$) b) high strain rate (10^{-3} s^{-1}).....	103
Figure 34. Tensile strength with a) low strain rate ($5 \times 10^{-5} \text{ s}^{-1}$) b) high strain rate (10^{-3} s^{-1}).....	103
Figure 35. Elasticity Modulus with a) low strain rate ($5 \times 10^{-5} \text{ s}^{-1}$) b) high strain rate (10^{-3} s^{-1}).....	104

Figure 36. Strain Hardening Coefficient with	
a) low strain rate ($5 \times 10^{-5} \text{ s}^{-1}$)	
b) high strain rate (10^{-3} s^{-1}).....	104
Figure 37. % Elongation, δ with	
a) low strain rate ($5 \times 10^{-5} \text{ s}^{-1}$)	
b) high strain rate (10^{-3} s^{-1}).....	105
Figure 38. Strain rate sensitivity of yield strength for the various microstructures.....	105
Figure 39. Fractographs showing the intergranular fracture with the microstructure	
a) F	
b) C.....	115
Figure 40. Fractographs showing the intergranular fracture with cracks possibly following the columnar matrix grain boundary	
a) C	
b) M.....	115
Figure 41. Fractographs showing the faceted-cleavage and dimple-ductile fracture observed at room temperature with	
a) SSS	
b) F	
c) D	
d) D	
e) M	
f) C.....	116
Figure 42. Fractographs showing the quasi-cleavage and dimple-ductile fracture observed at 650°C with	
a) F	
b) D	
c) F (at periphery)	
d) D (at periphery)	
e) M	
f) C.....	119
Figure 43. Fractographs showing the flowery, quasi-cleavage, and cleavage fracture observed at 750°C with	
a) F	
b) D	
c) M and C	
d) C.....	120
Figure 44. Plot of energy-to-break in the tensile tests with	
a) low strain rate ($5 \times 10^{-5} \text{ s}^{-1}$)	
b) high strain rate (10^{-3} s^{-1}).....	121
Figure 45. Coefficient of Linear Thermal Expansion of IN738LC with various precipitate microstructures.....	125

LIST OF NOMENCLATURE

IN738LC: A Ni-base superalloy containing low carbon; patented trade mark of International Nickel Co., USA

$L1_2$: FCC superlattice of the Cu_3Au type

γ' : $Ni_3Al(Ti, Nb)$ precipitate phase in Ni-base superalloys with the $L1_2$ structure

ppt.: abbreviation used for precipitate.

SFE: Stacking fault energy

APB: Antiphase boundary

FC: Furnace-cooled

AC: Air-cooled

AAC: Accelerated air-(blowing air)-cooled

WQ: Water-quenched

HIPing: Hot isostatic pressing

SEM: Scanning electron microscopy

SE: Secondary electron

BSE: Back scattered electron

EPMA: Electron probe micro analyzer

EDS: Energy dispersive spectroscopy

PO: Preferred orientation

ABSTRACT

Three major aspects of the superalloy IN738LC are studied in this dissertation: i) precipitate microstructure evolution, ii) tensile mechanical properties, and iii) thermal expansion characteristics.

IN738LC is a Ni-base, γ' Ni₃Al(Ti) precipitate-strengthened alloy. This alloy includes ~20-43 volume % γ' and also some (Ta,Ti)C at the grain boundaries and in the matrix.

Different heat treatments were carried out to study the precipitate evolution mechanisms and kinetics in this superalloy. It was found that the proper solution treatment producing the single-phase supersaturated solid solution condition is 1235°C/4h/WQ. Solution treatment at 1200°C/4h/WQ, however, produces a refined precipitate microstructure. Aging treatments after both of these solution treatments give similar microstructures.

The precipitates grow in cuboidal form after agings at 1120-1130°C/24h. However, longer aging times (>48h) yield a duplex-size precipitate morphology in this temperature range. Likewise, the duplex-size morphology develops at 1140°C, but in a much shorter time (5 min.), and it is stable in the range 1140-1150°C. Activation energy calculations showed that the precipitate microstructure becomes more unstable and it dissolves into the matrix when the temperature increases above 1150°C, and in the range 1160-1225°C, a unimodal stable, fine-size precipitate microstructure develops.

XRD studies showed that different precipitate microstructures possess different preferred orientations. Precipitates tend to have the {220} or {200} orientation. Whereas most of the precipitate microstructures have single texture, the duplex-size precipitate

microstructure has the $\{111\}$ and $\{200\}$ preferred orientations for the matrix and the precipitates, respectively.

Tensile mechanical and thermal expansion tests proved that the size and morphology of the precipitate phase is very effective in determining the magnitude of these properties. Generally, microstructures having fine-size precipitates show higher yield strength, and elasticity modulus; in contrast, microstructures with coarser precipitates exhibit more elongation, strain-harden more, and acquire higher tensile strength. Tensile fracture is usually of the cleavage type with fine precipitates and ductile with the coarse ones. Thermal expansivity of the microstructures with fine precipitates is in general less than that of the microstructures with coarse precipitates.

CHAPTER I. INTRODUCTION

I.1. General

Superalloys are widely used in a variety of applications at temperatures ranging from 650°C to 1100°C in aggressive atmospheres, such as those experienced in rocket and jet engines, land-based gas turbines, and high temperature catalytic reactors, etc. In order to function satisfactorily in such severe environments, these alloys are required to possess at high temperatures good corrosion resistance, optimal thermal properties, strength coupled with ductility, creep and fatigue resistance, and optimal impact and wear resistance.

Ni-base superalloy IN738LC is one of the most widely used high temperature materials in severe corrosive environments and highly stressed regions. This superalloy is a very attractive candidate for high temperature utilization because of its endurance to these service conditions. Useful properties of the superalloy IN738LC are obtained through solid solution strengthening of the FCC nickel-base matrix and by dispersing γ' $\text{Ni}_3\text{Al}(\text{Ti},\text{Nb})$ intermetallic precipitate phase having the ordered FCC L1_2 structure with suitable shape, size, and volume fraction in it. The elements Al, Ti, and Nb in this intermetallic compound may substitute each other in the crystal structure.

The utilization temperature of the superalloy IN738LC is, in fact, strongly dependent on the microstructure stability, as is the case for all of the materials used in high temperature applications. Therefore, microstructure control and stabilization is very necessary for effective utilization of the superalloy IN738LC at high temperatures, for any change in the microstructure could vastly influence its properties. Interrelationships between the microstructure and the mechanical properties should be well understood.

This dissertation encompasses the work done on the superalloy IN738LC. Three different properties of this superalloy are studied at high temperatures. Precipitate strengthening nature of this material makes these property studies more complex and sophisticated. The properties studied are 1) precipitate microstructure evolution, 2) high temperature tensile properties, and 3) high temperature thermal expansion characteristics. Complementary to the tensile property study, the fractography of the test samples is also carried out.

Tensile test is an incipient but efficient way of obtaining information about materials, for it provides data on primary material properties such as elasticity modulus, yield and tensile strengths, ductility, and toughness under static loading conditions. Furthermore, this information can be employed as a base for the analysis of more complicated material behaviors, e.g., fatigue, creep, and crack growth.

Thermal expansion is an important design factor in the systems for high temperature applications. Low thermal expansion is required for superalloys, since they are utilized with very low tolerances at high temperatures. Usually, matching thermal expansions are necessary for mutually working components. High thermal conductivity is another important physical property that superalloys need to meet in order to remove the heat fast. These physical properties secure the high temperature superalloys against thermal shocks.

Even though the superalloy IN738LC is being used in high temperature applications mainly as turbine blades, the literature data on this superalloy is not sufficient. Especially, there is no complete work in the literature considering various precipitate size and morphologies and relating these to the thermal and/or mechanical

properties of this superalloy. The work presented in this dissertation provides the basic data on the microstructure evolution in this alloy and its influence on the thermal expansion characteristics and the tensile properties with respect to various precipitate microstructures. Therefore, it will be a useful addition to the scientific literature on the basic thermal and mechanical properties of the superalloy IN738LC.

I.2. Literature Information on the Superalloy IN738LC

Materials scientists tailor the microstructure and choose such materials that have microstructure stability and optimum physical and mechanical properties for applications under severe service conditions at high temperatures. Attempts to obtain and characterize various microstructures in materials with a view to obtain different properties have occupied the attention of materials scientists throughout the years.

I.2.1. Microstructure Development

IN738LC is a brand name for a polycrystalline Ni-base, low carbon, investment-cast superalloy, which is used for blades and discs in turbines, both in power generation and aeroengines. This superalloy was patented in August, 1969 by C. G. Bieber and J. J. Galka [1], assignors to the International Nickel Company, Inc., NY. IN738LC has about 43% γ' $\text{Ni}_3\text{Al}(\text{Ti}, \text{Nb})$ intermetallic precipitate phase in Ni-rich solid solution matrix [2-11]. The crystal structure of the matrix (conventional FCC) and of γ' (ordered FCC superlattice, $L1_2$) precipitate phase are shown in Fig. 1. The single phase γ' Ni_3Al persists with the long-range-order up to its melting point of 1380°C, which is still above the liquidus range (1340-1375°C) of the superalloy IN738LC [12]. However, there is no study done to determine the melting point of the precipitate phase (with Ti and Nb in substitution for Al) in the alloy.

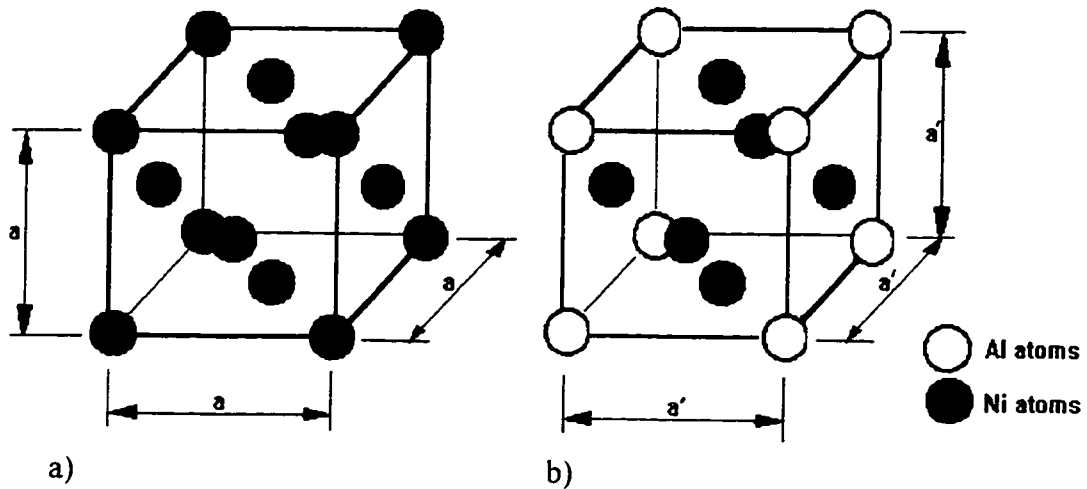


Figure 1. Crystal structure of a) FCC Ni-rich matrix and b) $L1_2$ Ni_3Al

The microstructural studies showed that the superalloy IN738LC has a negligible amount of fine $M_{23}C_6$ -type carbides at the grain boundaries and large blocky MC-type carbides at the grain boundaries as well as in the matrix. Carbide formation during different cooling rates from the melt was studied by Liu et al [13, 14]. They reported that slow cooling rates produce more and large blocky type MC carbides, and carbide refinement was observed with fast cooling rates and after cooling from temperatures close to 1595°C , which is far above the melting range (1340 - 1375°C) of this superalloy. Dominant MC-type carbides were also reported in Refs. [15-18]. Particularly, (Ta, Ti)C-type carbides were reported in Ref. [12]. These types of carbides melt above 1525°C .

IN738LC is conventionally produced via investment casting. After the casting, the superalloy is usually HIPed (Hot Isostatic Pressed) to remove microporosity. HIPing is ordinarily carried out at around 1200°C for 2 hours in a neutral environment. Thereafter, the alloy may be age hardened. The commercially suggested standard aging treatment for

this superalloy consists of two steps, solutionizing and aging. The solution treatment is carried out at 1120°C for 2 hours, and then cooling to room temperature is usually by blowing air, by so called accelerated air cooling (AAC), or by water quenching (WQ). The aging is a reheating of the material to 850°C and holding for 24 hours and finally furnace cooling (FC) to room temperature. Through this aging process, a bimodal γ' precipitate microstructure consisting of a cuboidal (~450 nm in size) and a spheroidal (~80 nm in size) morphology is obtained [15].

More complicated heat treatment procedures have been developed to suppress the formation of spheroidal precipitates and, as a result, to obtain a unimodal-cuboidal precipitate microstructure. These heat treatments are usually two step agings subsequent to a proper solution treatment. After the solution treatment at about 1120-1250°C for 2-4 hours, the first aging is carried out at a temperature around 950-1100°C, and the alloy thereafter is cooled to a lower aging temperature. The second aging is undertaken at a lower temperature (650-950°C) for a period of time, and later the alloy is cooled to room temperature. A wide range of holding times from 12 to 200 hours at higher and lower aging temperatures is reported in the literature. Various cooling rates are also given in the literature after both aging treatments.

Many researchers observed that with slow cooling rates after final aging, spheroidal precipitates tend to become cuboidal by long enough aging time. In Refs. [11,19], it is reported that the required time for this transformation is about 100-200 hours at around 1000°C, and a two step aging is necessary for the formation of a unimodal-cuboidal precipitation.

A number of experimental and theoretical studies have been carried out to understand the coarsening features of the second phase precipitate particles [20-47]. Various investigators considered the coarsening behavior of positively or negatively misfitting precipitates in the matrix. Precipitate evolution progresses toward the minimization of the total free energy of the system, which has two contributing-factors: the interfacial surface energy and the elastic strain energy. Results have suggested that the elastic strain energy due to the elastic self-energy and the configurational energy of the particles could play an effective role during the coarsening of precipitates. At the early stages of coarsening, the interfacial energy dominates the morphological evolution, while after the precipitates reach a critical size, the elastic strain energy term takes over. Directional alignment of the coarsening precipitates along the elastically soft directions, $\langle 100 \rangle$ in the Ni alloy systems, has also been reported, and it has again been attributed to the tendency to minimize the free energy of the system.

Microstructure control and stabilization is very necessary for effective utilization of the superalloys at high temperatures. Developing suitable processes to reduce the grain size and prevent the grain growth, which improve the mechanical properties of materials, is important in industrial applications. The usual way of obtaining reduced (refined) grain size in a metallic material is through thermo-mechanical treatments. Normal thermo-mechanical processes yield a recrystallized microstructure having reduced grain size through the interactions between the grain boundary and the precipitate [48]. The final microstructure is mainly affected by the dissolution or reformation of the precipitates. A recently developed method to obtain refined microstructure is thermal cycling. In this method also the grain size reduction is owed to the grain boundary and precipitate

interactions [49]. It is reported in Ref. [49] that a thermal cycling treatment produced a refined microstructure whose grain size was half that of the original. Radhakrishnan et al. [50] reported that grain boundary liquation can arrest the grain growth, enabling the reduced grain size. Formation of mosaic (fine) subgrains during annealing, caused by dislocation alignment, is also well known [51]. It is also reported that during fusion welding, high peak temperatures cause precipitate refinement and dissolution [52].

Second phase particle (precipitate) dissolution has been an issue for a long time. Different mechanisms have been proposed for the dissolution of particles into the matrix. Aaron and Kotler [53] considered the interactions and concentration gradients in the precipitate - matrix interface to account for the dissolution of the precipitate phase. They also studied the curvature effects on the dissolution kinetics. Vermolen and Zwaag [54] proposed a three-step model for second phase particle dissolution: decomposition of the particles, crossing of the boundary, and long distance diffusion. They also pointed out that interface interactions are the rate controlling processes for the dissolution of compound type particles, such as Ni_3Al .

I.2.2. Texture Development (Preferred Orientation)

Whenever materials are processed (thermally or mechanically), preferred orientation of certain sets of atomic planes or texturing is known to occur. Texture formation is of great interest to materials scientists, since vast directional variations in properties of the preferentially oriented microstructures are possible. Under different conditions, in general, two different types of textures have been obtained - annealing textures and cold work textures.

Grains, recrystallized after cold working, generally align preferentially along the active slip planes in them [55]. It is known that the amount of cold work and the annealing temperature affect the recrystallization textures. Beck who studied the annealing texture formation observed [56] that for FCC materials preferred orientation could be related to the interface mobility of the growing grains. He also discussed the oriented nucleation and growth of recrystallized grains in contrast with higher grain boundary mobility resulting in preferentially oriented textures. Beck concluded that some planes might be more mobile in reality than the others, even though the theoretical mobility of several different planes may be equal. Hence, onset of preferred orientation during annealing does not necessarily require any oriented nucleation. It is indicated also that the oriented nucleation and subsequent growth and/or the selective growth of grains due to higher mobility of certain planes may be both responsible for the formation of annealing textures in materials [57].

Cube texture formation in Al-Mn alloys was studied by Koppelaar et al. [58]. The authors observed that the amount of the cube texture (100) increases with increasing annealing temperature. Also, the above texture develops and proceeds at the expense of some of the other possible textures, such as (123)[421].

In contrast, the cold work textures are those preferred orientations produced by the preferential flow of grains during plastic deformation. Cross slip has been taken into consideration in the FCC materials for the formation of cold work textures. In Ref. [59], it was reported that whenever cross slip does not happen, 'alloy' type $\{110\}\langle 112\rangle$ texture forms in Al; otherwise the $\{112\}\langle 111\rangle$ rolling texture prevails under heavy cold deformation situations.

Change in texture orientation during annealing has been studied in the superalloy MA 957 [60]. It was found that this alloy exhibits a [110] texture in the as-extruded condition, but this is not present after recrystallization. At high zone-annealing speeds the alloy showed [113] texture, with an increasing proportion of [111] texture being present at slower speeds. These findings were attributed to solute segregation and interfacial mobility. A [100] texture formation during the solidification of castings of X750 superalloy has also been observed [61]. A similar preferred orientation also was reported for the superalloy MA6000 during annealing. Among the possible reasons listed for cube texture formations are reduction in grain boundary energy, grain rotations, and growth of suitably oriented annealing twins [62].

I.2.3. Tensile Properties

As already stated, the superalloy IN738LC is strengthened by the γ' precipitates of $\text{Ni}_3\text{Al}(\text{Ti}, \text{Nb})$ basic composition and $L1_2$ crystal structure. Single-phase intermetallic alloy Ni_3Al shows anomalous increase in strength with increasing temperature at around 750°C [6, 63-69]. Anomalous strengthening with the γ' precipitates is also observed in IN738LC, but it is not as pronounced as in the case of pure Ni_3Al . In general, if a superalloy has high volume fraction of the γ' precipitate phase, it tends to show a significant anomalous strengthening behavior with increasing temperature as the γ' phase itself.

The models explaining the mechanism of strengthening in particle reinforced systems consider the dislocation - obstacle interactions and the effect of these interactions on the dislocation motion. Main dislocation - obstacle interactions are given in Fig. 2 [63].

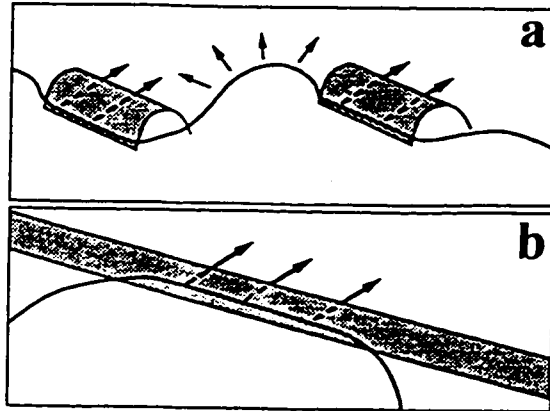


Figure 2. Different possible dislocation precipitate interactions [63]

- a) bypassing and cutting
- b) cutting

The obstacles (pinning particles: precipitates, carbides, and dispersoids, etc.) could be either discontinuous or continuous. In the former case, the efficiency of the obstacles is determined by the interparticle distance or the strength of the particles. When the inter-particle distance is large enough, the dislocations can bypass the pinning particles by bowing (Orowan mechanism) in the free spaces, as seen in Fig. 2a. Clearly, decreasing the interparticle separation will increase the pinning efficiency of the particles. In the latter case (continuous obstacles), however, stress anomalies arise from only the higher strength of the particles, since the only interaction is the cutting of the particles by moving dislocations.

It is now well accepted that an anomalous increase in strength of Ni_3Al found at around 750°C is due to the locking of screw dislocations of $\{111\}$ octahedral planes on $\{100\}$ cubic planes of the ordered FCC crystal [6, 63-68]. The models proposed to explain these anomalous properties differ only in accounting for the type of obstacles and the way these obstacles are overcome. The anomalous strengthening observed in IN738LC is also attributed to a similar mechanism that gives rise to the strengthening at high temperatures in Ni_3Al [6].

C. G. Bieber, who is one of the developers of the IN738LC, and J.R. Mihalisin did the first study on the tensile properties of the superalloy IN738LC [15]. They reported that the main deformation mechanism was through dislocation looping around the γ' precipitates. No cutting of the precipitates was observed even at 982°C, but as the temperature increased from room temperature to 982°C, densification of the interface dislocations was observed. These observations were attributed to the strong precipitate phase. However, their results did not show any anomalous strengthening at any elevated temperature, which is somehow unaccountable.

Among the very few other studies on the tensile properties of IN738LC, the dislocation structure after tensile loading is given in Ref. [2]. Under the testing conditions of low applied stress and low strain rates, the dislocations were usually observed in the γ -matrix, few dislocation networks in the γ/γ' interface, and no dislocation in the γ' particles. In the intermediate to high stress and strain rate regime, however, the dislocations were mainly confined in the γ' particles, and stacking faults lying on $\{111\}$ planes within the γ' particles were observed. It was also reported in Ref. [2,70] that the precipitate size and morphology are effective on the structure and movement of dislocations.

Ziebs et al. [9] reported that IN738LC strain hardens at $T \leq 600^\circ\text{C}$ and at 750°C only if the strain rate is equal to or higher than 10^{-3} s^{-1} . At high strain rates shearing of the precipitates and formation of denser dislocations were observed. They also reported an anomalous strengthening in the range $600\text{-}850^\circ\text{C}$ depending on the strain rate used. As the strain rate increased, the peak of the anomalous strengthening shifted to higher temperatures. Similar observations were also reported in Refs. [6,71]. An increase in the

magnitude of the peak stress with higher strain rates was also reported for the superalloy MAR-M200 in Ref. [71].

The Study of Bettge et al. on the tensile properties of IN738LC is reported in Ref. [6]. In their study, the alloy showed much higher strength at room temperature, a minimum in strength at around 450°C, and another maximum at around 750°C, which was yet lower than the strength at room temperature. Above 750°C the strength decreased steadily. This observed strength-temperature dependency of IN738LC alloy is attributed to three different deformation mechanisms functioning at different temperatures. These mechanisms are summarized as follows: At 20°C- formation of low temperature stacking faults (SF); at 450°C- cutting of γ' precipitates by anti-phase boundary (APB)-coupled dislocation pairs, and at 750-950°C- climb-assisted Orowan looping (bypassing the γ' precipitates). Occurrence of a given mechanism indicated above depends on the γ' size, temperature, stress, and strain rate.

The strain rate dependency of strength in IN738LC is also reported. This fact is attributed to the change in the deformation mechanism from precipitate cutting to Orowan looping [6, 70, 72,73]. The strain rate dependency of γ' precipitate-strengthened alloys is more evident at high temperatures. This is attributed to the diffusive motion of APBs behind dislocations, which have cross-slipped to cube planes. This suggests that the deformation is more diffusion dependent at high temperature.

I.2.4. Fracture Behavior

Carbides formed in IN738LC affect its mechanical and fracture properties. Observation of intergranular fracture in this superalloy is attributed to large MC-type grain boundary carbides [17,18,74,75]. It is reported in Ref. [17] that blocky MC

carbides are stress raisers and play a role as crack initiation sites. Decohesion of carbide - matrix interface, leading to crack nucleation, was also observed at 950°C.

Precipitate formation at the grain boundaries could serve as crack arresting sites. Such precipitates could also deflect the advancing cracks, which creates a serrated grain boundary fracture. In fact, according to the study given in Ref. [76], the large grain boundary precipitates are more effective strengtheners under fatigue conditions than the finer ones dispersed in the matrix. Moreover, a study on the superalloy IN738LC under fatigue loading conditions showed that the γ' morphology is not influential on the type of fracture encountered in the temperature range from 650 to 950°C [77].

The crack is stated to follow the $\{111\}$ path at room temperature [78], whereas the fracture occurs through the $\{100\}$ planes at temperatures above 650°C under fatigue loading [78,79]. While propagating in the matrix, the crack prefers the $\{100\}$ path, and when it meets the precipitates, crack branching takes place, and the crack either crosses the precipitate [79,80] or propagates along the interface where the dislocation density is high [3,7,79]. When the crack cuts through the precipitates, it still follows the $\{100\}$ path [75,77-80], though the propagation slows down. Observation of the faceted fracture surfaces is actually a result of the crack path on $\{100\}$ planes. Generally, at any temperature of low ductility, cleavage-type fracture was reported [7,18].

1.2.5. Thermal Expansion Characteristics

Gas turbines and aerospace engines, where the superalloy IN738LC is extensively utilized, operate most efficiently under close tolerances, which makes thermal expansion an important design factor. Similar thermal expansion coefficients in mutually interacting

components are oftentimes necessary. Usually, a low coefficient, acceptable to minimize thermal stresses, is preferred.

Thermal expansion of materials is due to the enhanced lattice vibration of the crystal structure. Hence, the thermal expansion coefficient α of materials is a structure sensitive property. In thermodynamics respect, α is related to the specific heat as

$$\alpha = (\varphi\chi_T/3V)C_v \quad (1)$$

which is the Gruneisen's rule [81], where φ denotes the Gruneisen's coefficient, χ_T the isothermal compressibility, V the molar volume of the solid, and C_v the molar volume specific heat. As shown in Eq. (1), α is linearly related to the specific heat.

Thermal expansion is very sensitive to the nearest neighbor interactions, bond type and length, planar atomic density, and the electron configuration of the crystals [82-84]. These are the basic reasons why two materials with the same crystal structure would show different elastic properties and hence thermal expansion. In polycrystalline aggregates, grain boundary type is also an important factor affecting the thermal expansion coefficient of the material [85]. Different reversible elastic properties can be interrelated (e.g., thermal expansion coefficient with the elasticity modulus) because the factors determining them are similar elastic parameters.

It is reported for Ni_3Al in Ref. [86] that the thermal expansivity of this material is composition insensitive, because the lattice contribution to its specific heat is also composition insensitive at low temperatures. However, the experimental thermal expansion data of the iron-nickel Invar casting alloy [87] showed that its coefficient of linear thermal expansion is strongly composition dependent and that slight variations in chemical composition leads to abrupt changes in thermal expansion coefficient. Amount

and distribution of Ni was the main determining factor of the thermal expansion variations. Inhomogeneous segregation of Ni caused anisotropic thermal expansions in different parts of the material. These observations point to the importance of processing methods, which can vastly affect the thermal expansivity of materials [88].

Observations of directionally varying thermal expansion were also reported. These types of variations could be due to structural anisotropy or to some directionally localized defects, such as microcracks, jogs, and voids. Microcrack formation during processing of the materials may deteriorate the mechanical properties and lead to different thermal expansion coefficients in different directions [88-90]. Also, in Ref. [91], it is observed that the differences in lattice mismatch give rise to varying thermal expansion coefficients, perhaps still as a result of microcrack formation in the structure and constraints at the interface. Effect of vacancy density on thermal expansion is given in Ref. [92]. The known vacancy contribution to the specific heat, in turn, relates to thermal expansion. Also, texture formation in the microstructure may significantly affect the modulus of elasticity and the thermal expansion coefficient of the materials in different directions.

1.3. Objectives of the Present Research

Correlation of microstructure to the mechanical and physical properties deserves a careful investigation, especially for those materials having complex microstructure that are utilized at high temperatures, such as the superalloy IN738LC.

The focus of this study is to establish a relationship between the developed microstructures and the physical (thermal expansion) and mechanical (tensile) properties of the superalloy IN738LC for high temperature applications.

Establishing a relationship between the microstructure and the physical and mechanical properties of the alloy will help in:

- i) proposing a heat treatment procedure that develops the optimum microstructure(s) for high temperature service,
- ii) originating a data source on the thermal expansion characteristics and the tensile properties at high temperatures as a function of precipitate size and its distribution in the matrix.
- iii) proposing a temperature range in which the superalloy can be used effectively, and conversely, the temperature range where the alloy cannot be subjected to structural applications due to its microstructural instability leading to property degradation.

CHAPTER II. EXPERIMENTAL

II.1. Materials

The material used in this study is the polycrystalline superalloy IN738LC, which is a brand name for a low carbon investment cast Ni-base superalloy. This material was provided by Howmet Corporation, Whitehall, Michigan, in the form of rods with 15 mm diameter and 110 mm length. The cast rods were HIPed (hot isostatically pressed) at 2165°F (1185°C) for 2 hours to remove microporosity and then cooled to room temperature. The processing was undertaken in a neutral atmosphere. After being HIPed, the superalloy was solution treated at 2050°F (~1120°C) for 2 hours. Following the solution treatment, an argon-backfill cooling to room temperature was given, with the cooling rate approximately equivalent to air-cooling. Aging was carried out at 1550°F (843°C) for 24 hours, and cooling to room temperature was again by argon backfilling. HIPing and aging were carried out by the supplier. The as-received stock had followed the above heat treatments. The chemical composition of the as-received material is given in Table 1, and its matrix grain morphology and precipitate microstructure are shown in Fig. 3.

II.2. Microstructure Development and Characterization

For various aging heat treatments undertaken in this study, small samples of triangular shape with ~4 mm thickness and ~6mm edge length, cut from the as-received cylindrical bars, were wrapped individually with a stainless steel foil and then sealed in silica tubes under vacuum. Stainless steel wrapping was to prevent any possible reaction between the silica tube and the sample.

Table 1. Chemical composition of the as-received IN738LC

Element	Ni	Cr	Co	Mo	W	Ta	Nb	Al	Ti	B	Zr	C
wt.%	balance	15.7- 16.3	8.0- 9.0	1.5- 2.0	2.40- 2.80	1.5- 2.0	0.60- 1.10	3.20- 3.70	3.20- 3.70	0.007- 0.012	0.03- 0.08	0.09- 0.13

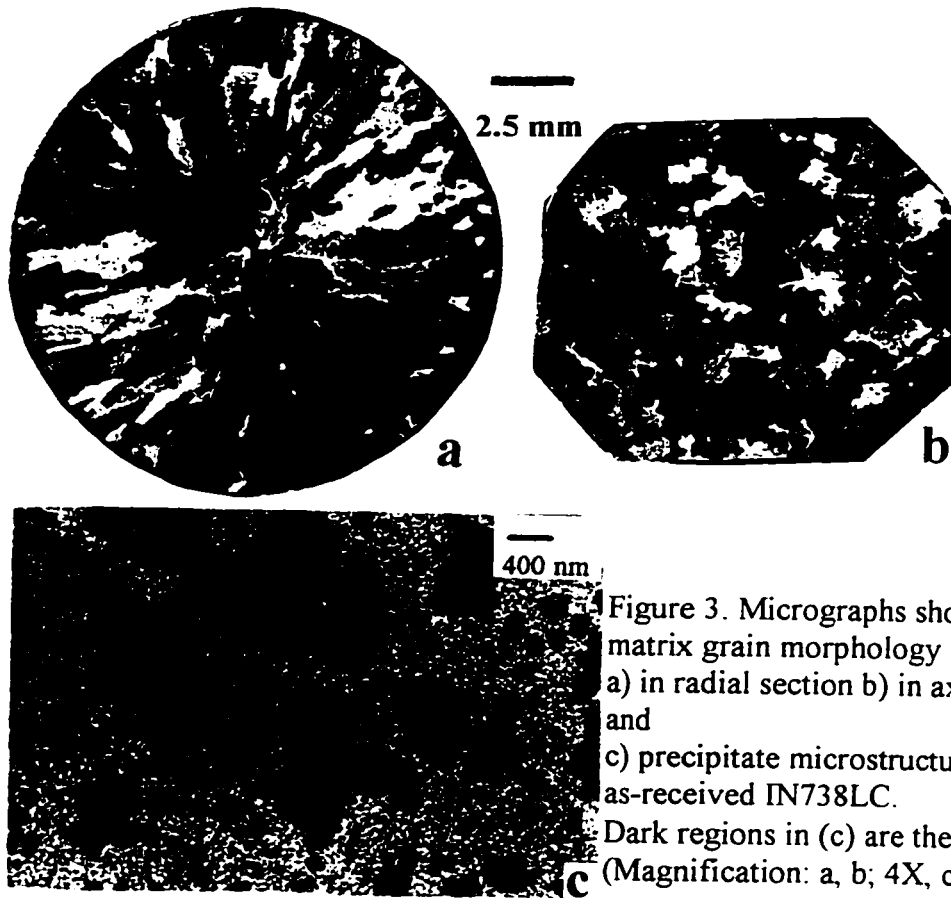


Figure 3. Micrographs showing the matrix grain morphology in a) in radial section b) in axial section and c) precipitate microstructure of the as-received IN738LC.

Dark regions in (c) are the γ' precipitates (Magnification: a, b; 4X, c; 15kX)

Table 2. Heat Treatment schedules for the IN738LC

Solution treatment	aging treatment
1120°C / 2 h / WQ	
1120°C / 2 h / AC	
1120°C / 2 h / AAC	
1120°C / 2 h / FC	
1120°C / 2 h / AAC	750°C / 24 h / FC
1120°C / 2 h / AAC	850°C / 24 h / FC
1120°C / 2 h / AAC	850°C / 12 h + 750°C / 12 h / FC
1200°C / 4 h / quenched in iced salt water	
1200°C / t / WQ (t= 4, 24, 72, 240 h)	
1200°C / t / AAC (t= 4, 24 h)	
1200°C / 4 h / FC	
1200°C / 4 h / AAC	650°C / 24 h / FC
1200°C / 4 h / AAC	750°C / 24 h / FC
1200°C / 4 h / AAC	850°C / 24 h / FC
1200°C / 4 h / AAC	950°C / 24 h / FC
1200°C / 4 h / AAC	1050°C / 24 h / FC
1200°C / 4 h / AAC	1120°C / t / FC (t= 24, 48, 72 h)
1200°C / 4 h / AAC	950°C / 12 h + 850°C / 12 h / FC
1200°C / 4 h / AAC	950°C / 12 h + 750°C / 12 h / FC
1200°C / 4 h / AAC	950°C / 12 h + 650°C / 12 h / FC
1200°C / 4 h / AAC	850°C / 24 h / WQ
1200°C / 4 h / AAC	950°C / 24 h / WQ
1200°C / 4 h / AAC	1050°C / 24 h / WQ
1200°C / 4 h / AAC	1070°C / 24 h / WQ
1200°C / 4 h / AAC	1090°C / 24 h / WQ
1200°C / 4 h / AAC	1120°C / 24 h / WQ
1200°C / 4 h / AAC	1130°C / 24 h / WQ
1200°C / 4 h / AAC	1140°C / t / WQ (t= 1, 3, 5, 30 min.; 2, 4, 12, 24, 48, 96 h)
1200°C / 4 h / AAC	1150°C / 24 h / WQ
1200°C / 4 h / AAC	1160°C / 24 h / WQ
1200°C / 4 h / AAC	1170°C / 24 h / WQ
1200°C / 4 h / AAC	1180°C / 24 h / WQ
1200°C / 4 h / AAC	1120°C / 24 h / FC + 1140°C / t / WQ (t= 1, 3, 5, 30 min.; 2, 4, 12, 24 h)
1200°C / 4 h / AAC	1120°C / 24 h / FC + 1160°C / t / WQ (t= 15, 30, 60 s; 5, 30 min.; 2, 4, 12, 24 h)
1200°C / 4 h / AAC	1120°C / 24 h / FC + 1200°C / t / WQ (t= 1, 3, 5, 30 min.; 2, 4, 12, 24 h)
1200°C / 4 h / AAC	1140°C / 4 h / WQ + 1160°C / t / WQ (t= 15, 30, 60 s)
1225°C / 4 h / WQ	
1225°C / 4 h / AAC	
1235°C / t / WQ (t= 30 min.; 2, 4 h)	
1250°C / 4 h / WQ	
1250°C / 4 h / AAC	
1250°C / 4 h / FC	
1250°C / 4 h / AAC	650°C / 24 h / FC
1250°C / 4 h / AAC	750°C / 24 h / FC
1250°C / 4 h / AAC	850°C / 24 h / FC
1250°C / 4 h / AAC	950°C / 24 h / FC
1250°C / 4 h / AAC	1050°C / 24 h / FC
1250°C / 4 h / AAC	1120°C / 24 h / FC
1250°C / 4 h / AAC	1200°C / 24 h / FC
1250°C / 4 h / AAC	1200°C / 24 h / WQ
1250°C / 4 h / transfer to	1140°C / t / WQ (t= 1, 3, 5, 30 min.)

Heat treatment schedules chosen in this study are given in Table 2. Solution treatment given to precipitate hardenable alloys consists of heating the alloy at a high enough temperature to dissolve the solute atoms in the matrix crystal structure. The alloys are then quenched thereafter (cooled to room temperature) in suitable media to retain excess amount of solute atoms in solid solution at room temperature. Heat treatment is a procedure of heating the samples to different temperatures for different time periods, then cooling to room temperature using a specific cooling mode, through quenching in iced salt water, water quenching (WQ), air cooling (AC), accelerated air cooling - in blowing air- (AAC), and furnace cooling -by switching off the furnace- (FC).

Different treatments were carried out to determine the proper solutionizing procedure. After proper solution treatment, the aging consisted of reheating the samples under similar conditions (wrapped and sealed under vacuum) to different temperatures for different time periods. The samples were held at a chosen temperature for different time periods and cooled to room temperature by FC or WQ. The cooling rate curve for FC treatments is given in Fig. 4. WQ is a fast cooling process involving high cooling rates around thousand degrees per second.

For precipitate microstructure studies, the samples were ground using grinding paper with coarse (120) to fine (600) grit size, and polished on rotating wheels with fine alumina powder of size down to 0.05 micron. After cleaning, they were etched with a solution of composition 33% HNO₃ + 33% acetic acid + 33% H₂O + 1% HF. Matrix grain morphology was revealed by etching with a solution of composition: 50 ml HCl + 50 ml H₂O₂ + 10 g Cu₂SO₄. A Hitachi S-2460N type scanning electron microscope (SEM) was used to characterize the size and morphology of the γ' precipitates. Back

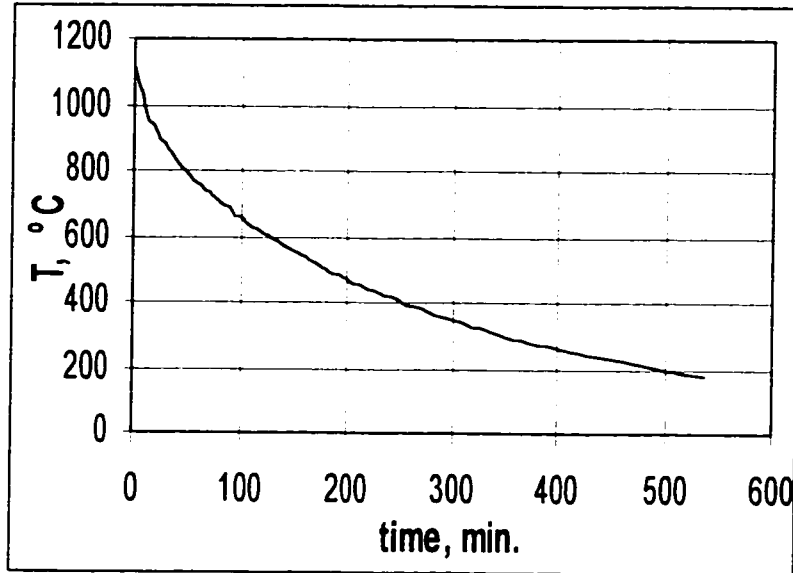


Figure 4. The plot showing the cooling curve that was obtained in the heat treatments under furnace cooling (FC) conditions.

scattered electron (BSE) mode was used in SEM because of its higher energy and composition sensitivity. Magnification was maintained the same in all cases at 15000X (15kX; 1.5 mm in the precipitate micrographs = 100 nm) to enable the comparison of precipitate sizes.

Qualitative chemical composition analysis of the γ' precipitates was carried out with a CAMECA SX50 electron probe microanalyzer (EPMA), equipped with a gas flow proportional detector, at Indira Gandhi Center for Atomic Research (IGCAR), Madras, India. A precise quantitative chemical analysis of the precipitates could not be made due to their extreme small size.

Structure and orientation studies were carried out on five different, but analogous batches of specimens after obtaining different precipitate microstructures. About one mm thick rounds (radial section) and rectangles (axial section) of samples with these

microstructures were cut using a diamond cut-off wheel. In most cases, samples were cut parallel to the radial plane of the rounds after heat treatments, corresponding to the radial section of the as-received bars. However, in a few cases, specimens were prepared by cutting parallel to the axial plane of the cylindrical bars. Heat treatment was undertaken after cutting the specimens in a few cases.

The specimens were then subjected to X-ray diffraction (XRD) analysis using Cu K_{α} X-rays in a computer-controlled Siemens D5000 Diffractometer, equipped with a Kevex Psi Peltier-cooled silicon detector. The scan range was between 5° and 100° of 2θ in all cases. Preferred orientation information and lattice parameters of phases were extracted from the XRD patterns of different samples. Preferred orientation is detected from the presence of significantly strong diffraction lines, unlike in the diffraction pattern of specimens with random (no preferred) orientation. In many instances, only one strong diffraction peak from a particular family of atomic planes was obtained indicating the presence of a clear preferred orientation.

Several $Ni_3Al(Ti,Nb)$ type alloys were also prepared and studied through XRD in order to evaluate the extension of the $L1_2$ -type superlattice, the changes in the lattice parameter and annealing texture, if any. These alloys were arc-melted in the form of small buttons under argon and sliced in the form of thin discs to undertake the heat treatment and XRD studies.

Also, Energy dispersive spectroscopy (EDS) technique was utilized in the composition analysis of the inclusions observed at the fracture surfaces of the broken tensile specimens.

Volume fraction of the γ' precipitates in various conditions was measured from the micrographs loaded in a PC using Image Tool image analysis program developed by UTHSCSA (University of Texas Health Science Center in San Antonio, TX). Precipitate size measurements were undertaken on SEM micrographs. Reported precipitate sizes were obtained after measuring the sizes of all of the precipitates in a representative micrograph and later averaging them. In the microstructures, the precipitate size pertained to average diameter in oval-shaped or near spheroidal particles, average cube edge in cuboidal particles, and average edge length in rectangular particles. Thus, the average sizes of differently shaped particles are utilized. The maximum and minimum sizes in a given microstructure as well as the number of particles averaged in each case were also noted down.

After the microstructure development and characterization studies, four different precipitate microstructures were chosen to investigate the physical (thermal expansion) and mechanical (tensile) properties of the superalloy IN738LC at high temperatures. These precipitate microstructures are included in a later chapter. Also, the representative micrographs of the matrix grain morphology in the radial and axial sections of IN738LC, similar in all of the microstructures tested, are given in Fig. 3a and 3b. Note that the matrix grains are large columnar-type in the radial section and nearly equiaxed in the axial section. The reason for choosing various precipitate microstructures is to investigate the microstructure - physical (thermal expansion) and mechanical (tensile) property relationship of this superalloy covering all possible microstructures (varying precipitate size and morphology) that can be assumed to be appropriate for high temperature applications. Solution-treated single-phase supersaturated solid-solution (SSS) material

with no precipitate was also included in thermal expansion and tensile tests in order to have the data for the SSS matrix. Single phase Ni₃Al was also included in the thermal expansion tests since it represents the γ' precipitate phase. Two identical specimens with similar heat treatment schedule were tested in each case under similar conditions.

II.3. High Temperature Tensile Tests

An MTS 810 Test Star servohydraulic Material Testing System (MTS, Minneapolis, MN) was used for tensile testings. This equipment has a digital control system, and is capable of performing most monotonic and dynamic tests of metallic, ceramic, and plastic materials. Maximum load capacity in this system is 50 KiP. Test Star 2 data acquisition software, developed by MTS and loaded in a 200 MHz - PC, was employed to obtain and evaluate the test data. An ATS (Applied Test Systems, Inc., Butler, PA) three zone high temperature furnace, equipped with a ceramic-probe, high temperature extensometer, is attached to the system, enabling the high temperature testings. The maximum temperature that can be attained with this furnace system is 1000°C.

For the tensile test and the specimen preparation, ASTM E8 and ASTM E21 standards [93] were adopted. In the current study cylindrical solid-type specimens were machined to the ASTM specifications. The gage diameter of the specimen was chosen to be 0.2 in., and the gage length was set to be 1.25 in.

After machining to the dimensions, the specimens were subjected to selected heat treatment schedules as explained in section II.2 to obtain five different predetermined microstructural conditions.

The tensile properties of the superalloy IN738LC with four different precipitate microstructures were evaluated at room temperature (RT), 650°C, 750°C, and 850°C, respectively. Two different static strain rates (10^{-3} s^{-1} and $5 \times 10^{-5} \text{ s}^{-1}$) were used. Two specimens were tested for each microstructure, strain rate, and temperature. Thus, sixteen specimens with different precipitate microstructures were tested at each temperature, and overall sixty four specimens with precipitate microstructure were tested and evaluated. Eight additional specimens (four at RT in the single-phase solution treated condition and four with only the fine-size precipitates at 1200°C) were tested with the two strain rates given above. Hence, the total number of specimens tested was seventy two. The tensile and yield strengths, elasticity modulus, ductility and strain hardening exponent, strain rate sensitivity, energy-to-break, etc. parameters were determined and their variations were analyzed.

II.4. Fractography of the Specimens after the Tensile Tests

Fractography of the specimens tested at room temperature (RT), 650, and 750°C was carried out using SEM. Secondary electron (SE) mode was utilized in this study. Energy dispersive spectrometry (EDS) technique was utilized to characterize the inclusions encountered on the fracture surfaces. The fracture mode was analyzed in each selected case.

II.5. Linear Thermal Expansion Tests

The dimensions of the thermal expansion specimens were chosen according to ASTM E228 [94], “Standard Test Method for Linear Thermal Expansion of Solid Materials with a Vitreous Silica Dilatometer”. For an accurate measurement of linear thermal expansion, the initial specimen length, L_0 , should be such that $\Delta L/L_0$ will be at

least $\pm 20 \mu\text{m}/\text{m}$, where ΔL is the dimensional change in the length. Since the sensitivity of LVDT (Linear Variable Differential Transformer) of the dilatometer used in this work is $10 \mu\text{in}$, the initial length of the specimen must be at least 0.5 in. In this research work, the length of round specimens was ~ 1.0 in. Additionally, a 1.0 in. long silica spacer was used with the test specimen in order to have a 2 in. length because the space between the end of the silica sample holder and the push rod was suitable for a 2 in. specimen length.

A Harrop Thermodilatometric Analyzer (Model TD-720) was used in measuring the linear thermal expansion of the specimens. The dilatometer module is made up of a heating/cooling chamber consisting of a wire-wound, non-shunted heating element, with a coil for liquid nitrogen inside and an insulated stainless steel canister. The measuring head consists of a compound slide assembly, LVDT, micrometer head, probe rod, and probe rod suspension assembly, all mounted on a low-expansion invar alloy support rod, which minimizes errors caused by changes in ambient temperature. The compound slide assembly permits the movement of the probe rod so that it may accommodate samples of different lengths. The probe rod is suspended on a set of leaf springs such that there is no sliding friction or bearing points to probe rod movement. This suspension system allows very low level loading of the sample. A micrometer screw allows precise displacement of the LVDT about the core, simulating core movement and allowing calibration checks.

The temperature control unit was a WEST 2050 microprocessor-controlled programmer/controller, designed to control temperature and time to a predetermined heating profile. The profile can range in complexity from simple one fixed set point up to four stages, each comprising a ramp and a dwell (soak). A cycling facility is provided to repeat the profile as desired.

A 386 PC, loaded with LABTECH 8.1 software and a CRYDAS 8 data acquisition board, manufactured by Cyber Research Inc., was used for data acquisition. The data evaluation and the linear coefficient of thermal expansion (CLTE) calculations were performed in a 486 PC, loaded with Stanford Graphics version 3.0, provided by Visual Numerics Inc.

Calibration of the test equipment was carried out using a 2 in. long standard alumina sample.

Before the thermal expansion tests, specimens were subjected to suitable heat treatment procedures to obtain four different precipitate microstructures and the single phase supersaturated solid solution in IN738LC.

The linear thermal expansion tests were carried out with specimens of the four different precipitate microstructures and single phase supersaturated solid solution matrix of IN738LC and with a single phase Ni_3Al intermetallic alloy at four different temperatures, 550, 650, 750, and 850°C. The heating profile for the thermal expansion tests is given in Fig. 5.

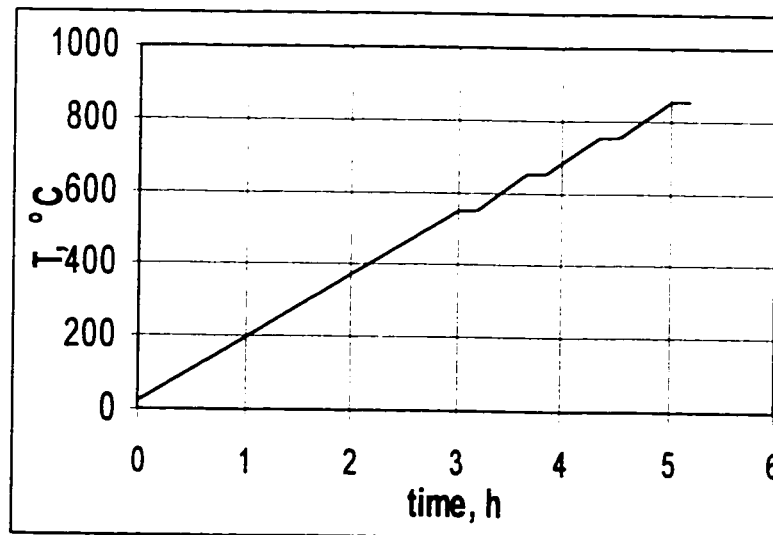


Figure 5. Heating profile used in the thermal expansion tests

The heating rate was chosen to be 3°C/min based on recommendations of the ASTM E228 standard [94]. At every temperature dwell, the specimen was held for 10 min to obtain a stable data. Two specimens were tested for each aforementioned microstructure. The average value of the two test results was used to calculate the linear thermal expansion ΔL from room temperature to a given high temperature and the expansion coefficient α ($= \Delta L/L_0\Delta T$) for the specimen of a certain microstructure. This value is plotted against the dwell temperature to yield α vs. T plot.

CHAPTER III. RESULTS AND DISCUSSIONS: MICROSTRUCTURE DEVELOPMENT AND CHARACTERIZATION

III.1. Microstructure Evolution in the Polycrystalline Superalloy IN738LC in the Range 650-1120°C.

Chemical composition analysis showed that the precipitates in IN738LC are of the $L1_2$ -ordered $Ni_3Al(Ti, Nb)$, γ' phase. The volume fraction of the precipitates in this alloy is 40-43% in the FC condition, which matches with the value given in the literature [2-11]. Much lower volume fractions were obtained in the analogous WQ samples (e.g., 23% at 1120°C/WQ and 30% at 1050-1090°C/WQ). However, several other findings of this study did not concur with what has been cited in the literature, especially in precipitate growth kinetics and morphology. Also, absence of a complete set of literature data on the heat treatments and microstructures of IN738LC did not facilitate a good comparison between the findings of this study and the ones in the literature.

III.1.1. Solution Treatments

Solution treatments were carried out at five different temperatures, 1120°C, 1200°C, 1225°C, 1235°C, and 1250°C, with different holding times, with a view to determine the proper temperature and time for a complete dissolution of γ' and formation of the single phase solid solution. It was determined that the 1120°C/2h solution treatment, commonly given in the literature [8,9], produces a bimodal precipitate microstructure. This solution treatment, hence, is not the proper one for a complete γ' dissolution. In fact, after solutionizing at this temperature for 2 hours, it was observed that the microstructure was not disturbed appreciably from that of the as-received material. Elongation of precipitates into oval or spheroidal ones (Fig. 6a,b) and

agglomeration of small precipitates into bigger ones (Fig. 6c,d) can be noticed, resulting in a depletion of fine precipitates near the big ones.

After solution treatment at 1200°C/4h/WQ, γ' precipitate refinement was observed, as seen in Figure 7. However, this temperature also was not high enough for a complete dissolution of γ' in the matrix. Increasing the holding time at solutionizing did not affect the solution-treated microstructure. This fact was established after 1200°C/(24, 72, 240h)/WQ solution treatments, which gave a similar refined precipitate microstructure as the 1200°C/4h/WQ solution treatment. Also, it was observed that subsequent cooling to room temperature by AAC, WQ, and iced-salt-water-quenching resulted in a similar microstructure, and no difference could be observed. Hence, the microstructure in Figure 7 is assumed to represent the equilibrium condition that evolves during or after solutionizing at 1200°C.

Finally, it could be determined that the solution treatments at 1235°C or at 1250°C for 4 hours are the proper ones for a complete γ' dissolution in the matrix. The 1250°C/4h solution treatment is also given in Reference [11] for a complete dissolution of the precipitates in the superalloy SC16, a derivative of IN738LC. A single solid solution phase with no γ' precipitates was observed (within the limits of the SEM) after these solution treatments, and this was true for cooling to room temperature by AAC or WQ. Consequently, for IN738LC, 1235°C is taken as the lowest solutionizing temperature, with 4 hours holding time, for a complete γ' dissolution and formation of a single phase solid solution.

On the contrary, furnace cooling (FC) from 1200°C/4h and 1250°C/4h gave precipitates larger in size than for analogous AAC and WQ conditions. However,

precipitates do not grow to a size larger than that of 1120°C/2h solution treatment. This result establishes the fact that precipitate growth occurs during solutionizing up to 1120°C, beyond which precipitate refinement sets in. Normally, such precipitate or, in general, grain refinement is obtained via thermo-mechanical processes. However, precipitate refinement by solutionizing is a recently discovered phenomenon. This has also been observed by some researchers in certain high temperature materials through only thermal processes [48,49,51]. Precipitate refinement in IN738LC at high temperatures in the range 1120-1250°C is a topic discussed in detail in the following section, III.2.

III.1.2. Effect of Single and Double Agings on the Microstructure

III.1.2.1. Agings after the solution treatment at 1120°C for 2 hours

In general, there was no difference in the microstructure after single aging or double aging at lower temperatures subsequent to the 1120°C/2h solution treatment. The duplex size γ' microstructure of the as-received material had not been disturbed greatly. The micrographs in Figure 8 show this very clearly. This finding is contradictory to the results given in Refs. [2,6,9], which indicate that with single aging after the above solution treatment, bimodal (spherical and cuboidal) precipitates and with double aging unimodal-cuboidal precipitates form. However, the results of the present study show that there is no effect of double aging on the precipitate morphology, and single aging at any lower temperature for 24h after the 1120°C/2h solution treatment does not produce any cuboidal precipitate either.

III.1.2.2. Agings after the solution treatments at 1200°C/4h and 1250°C/4h

Microstructures obtained after agings at different temperatures subsequent to 1200°C/4h/AAC or 1250°C/4h/AAC solution treatments were nearly similar in γ' morphology and size, as can be observed in Figures 9d,e and 10a,b.

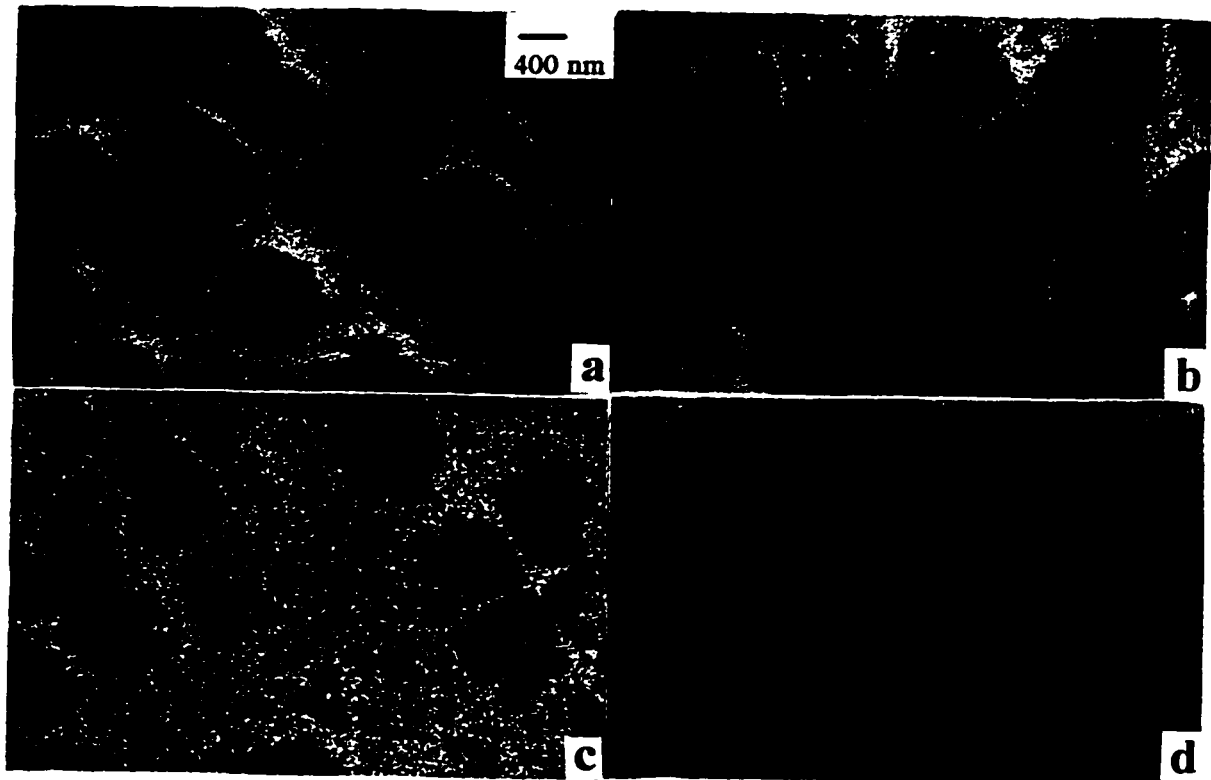


Figure 6. Microstructures after the solution treatment at 1120°C / 2h.
(Magnification: 15kX)

- a) FC-condition b) AC-condition
c) AAC-condition d) WQ-condition

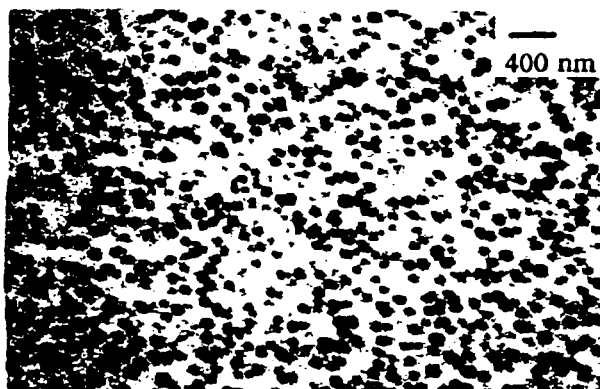
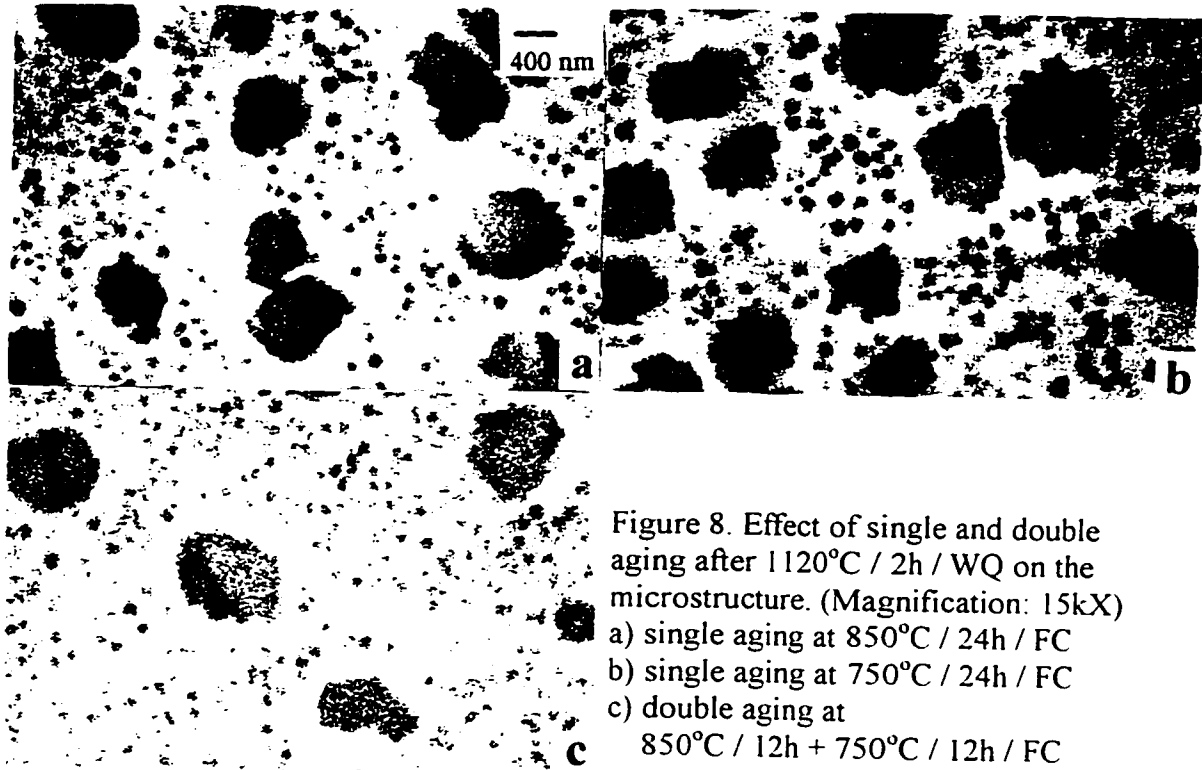
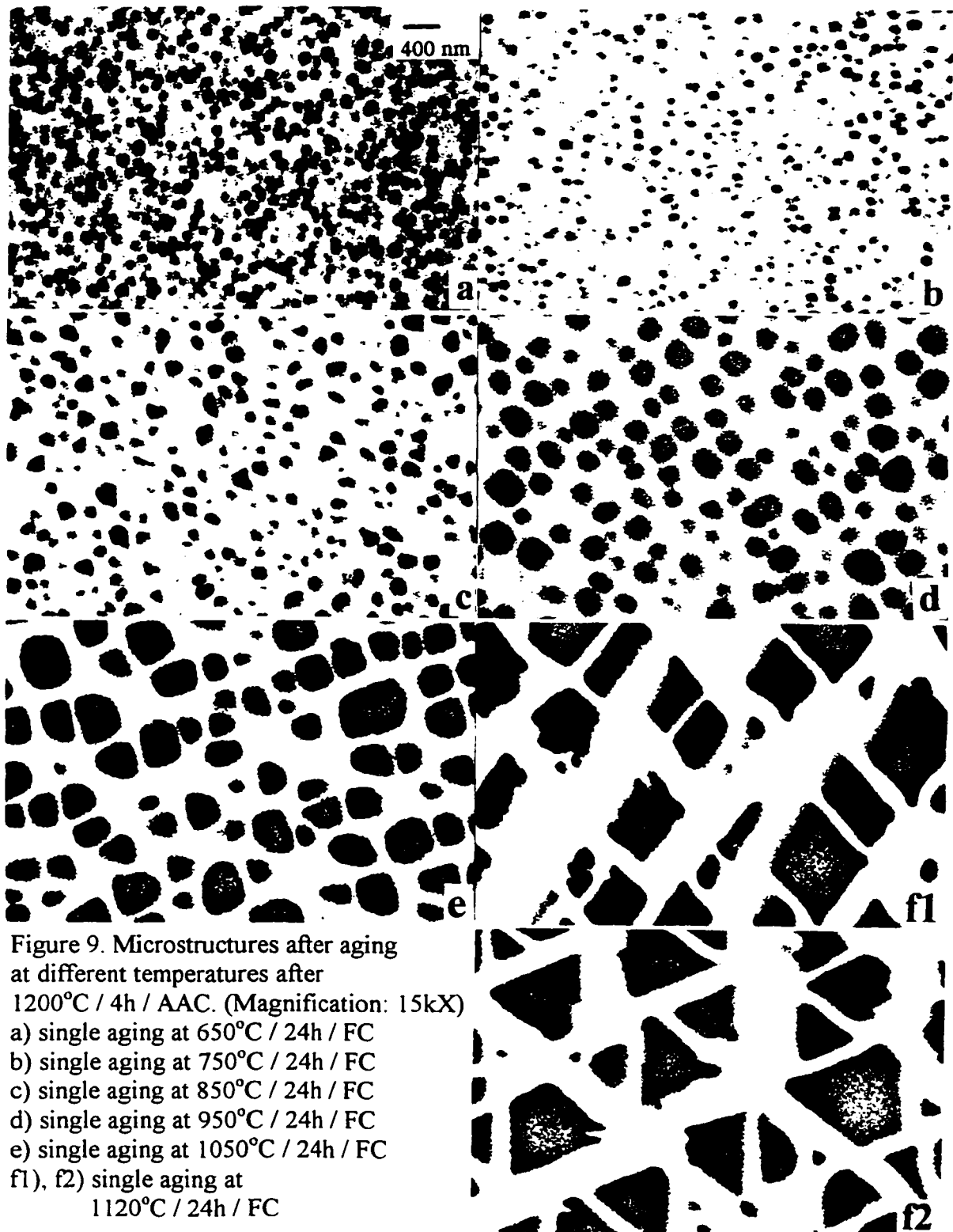


Figure 7. Refined microstructure after
1200°C / (4, 24, 72, 240h) / (AAC, WQ)
solution treatment. (Magnification: 15kX)



A very important result obtained with these heat treatments is that a unimodal-cuboidal precipitation is possible with single aging as opposed to the information available in some publications, according to which a unimodal-cuboidal precipitation is possible only with double aging [2,3]. The micrographs in Figures 9 and 11 are clearly indicative of the fact that with a single aging at a fixed temperature at and above 1050°C, unimodal-cuboidal-precipitates form. Malow et al. [11] had also obtained similar results as in the present work; however, they found that unimodal-cuboidal precipitation occurs only after 110 hours with single aging at 1000°C, i.e., it requires a much longer time at lower temperatures. Kusabiraki et al. [19] also reported a similar finding for Nimonic-105 and stated that after aging for 100 hours in the range 800-950°C the γ' precipitates showed a

partial change to cuboidal shape and after 200 hours the precipitates were completely cuboidal in shape. The results in the present study show that a cuboidal precipitation is possible with a 24-hour single aging at 1050°C. Also, in Ref. [11], it is stated that after a two-step aging, fast cooling rates give bimodal precipitates, and slow cooling rates (e.g., FC) give unimodal-cuboidal precipitates. A similar result observed in this study is noteworthy. FC gives nearly cuboidal and WQ gives nearly spheroidal precipitates after single aging at 950°C/24h, Figures 9d and 11b, respectively. Nevertheless, in this study, it was also observed that regardless of cooling rate, either by fast cooling or slow cooling, a unimodal-cuboidal precipitation occurs after aging for 24 hours at and above 1050°C. In the cases of agings below 1050°C and cooling by FC, the precipitates are nearly spheroidal, and as can be seen in Fig. 9d, aging at 950°C/24h/FC is a transition from an incomplete to a nearly cuboidal shape. This transition at 950°C/24h was not observed after cooling by WQ, and the precipitates were spheroidal after agings at and below 950°C and cuboidal above it. This observation indicates that for aging at ~950°C, longer holding times might produce complete cuboidal precipitation in concurrence with the findings of Kusabiraki et al. [19]. Contrary to the information given in Ref. [11], micrographs in Figure 12 show that double agings carried out at lower temperatures do not change the microstructure, and the microstructure of the higher temperature aging is kept undisturbed after the second aging at a lower temperature. In all these cases nearly spheroidal morphology of the γ' precipitates is evident.



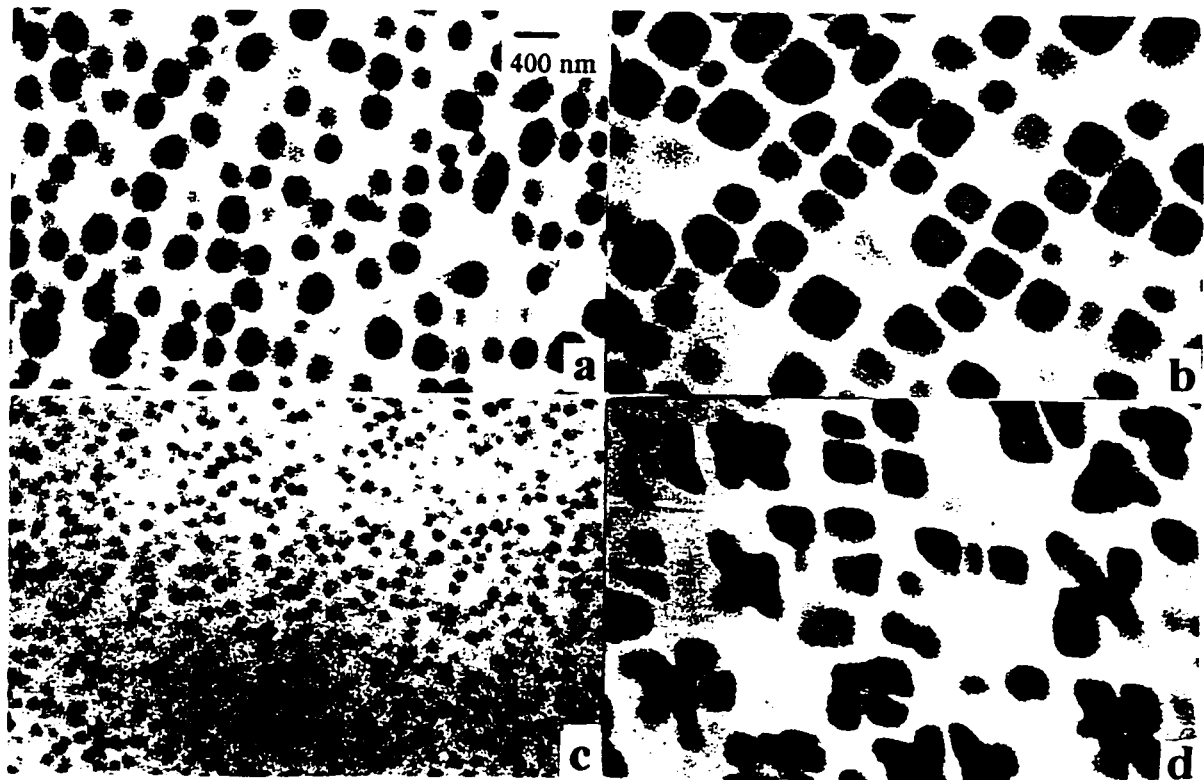
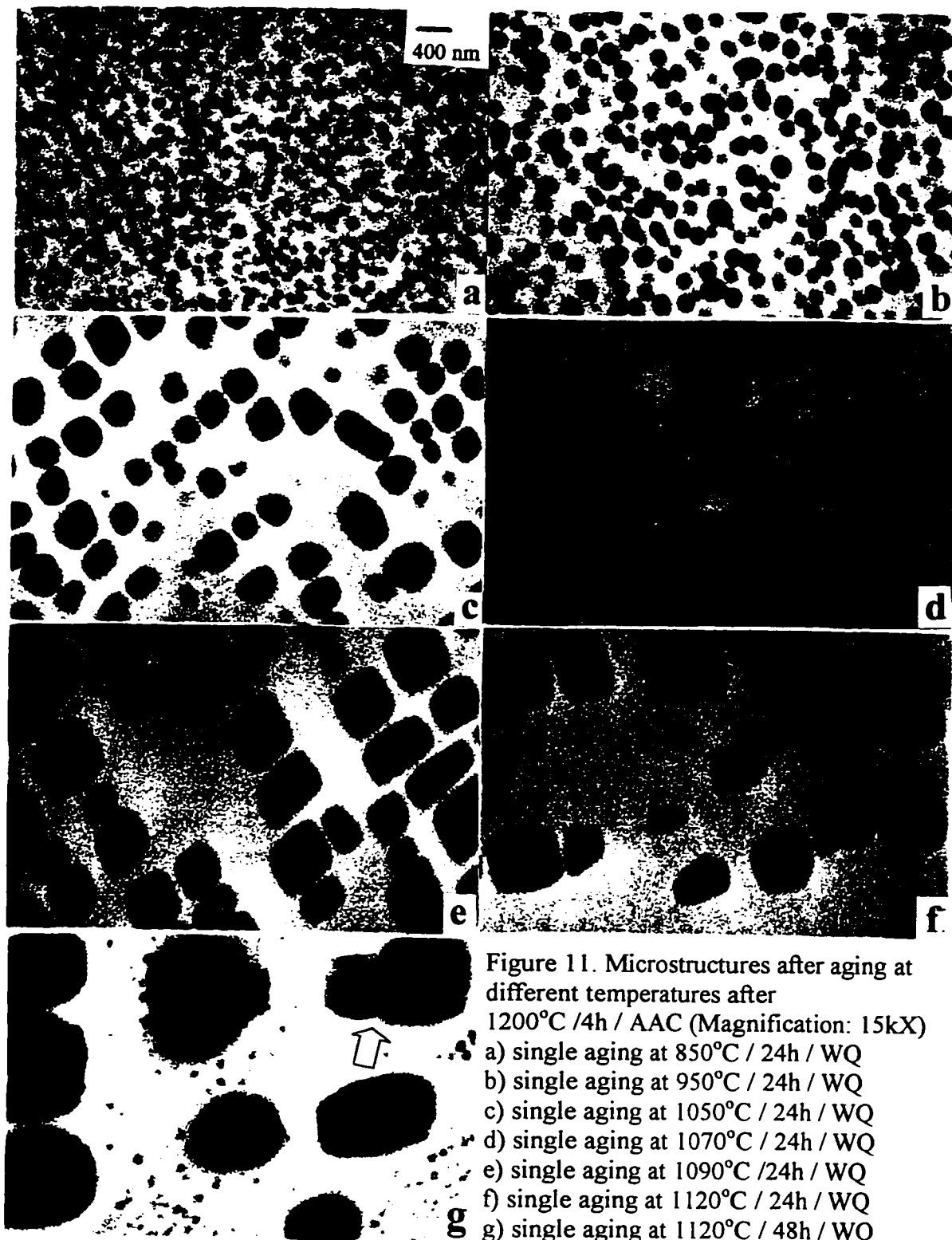
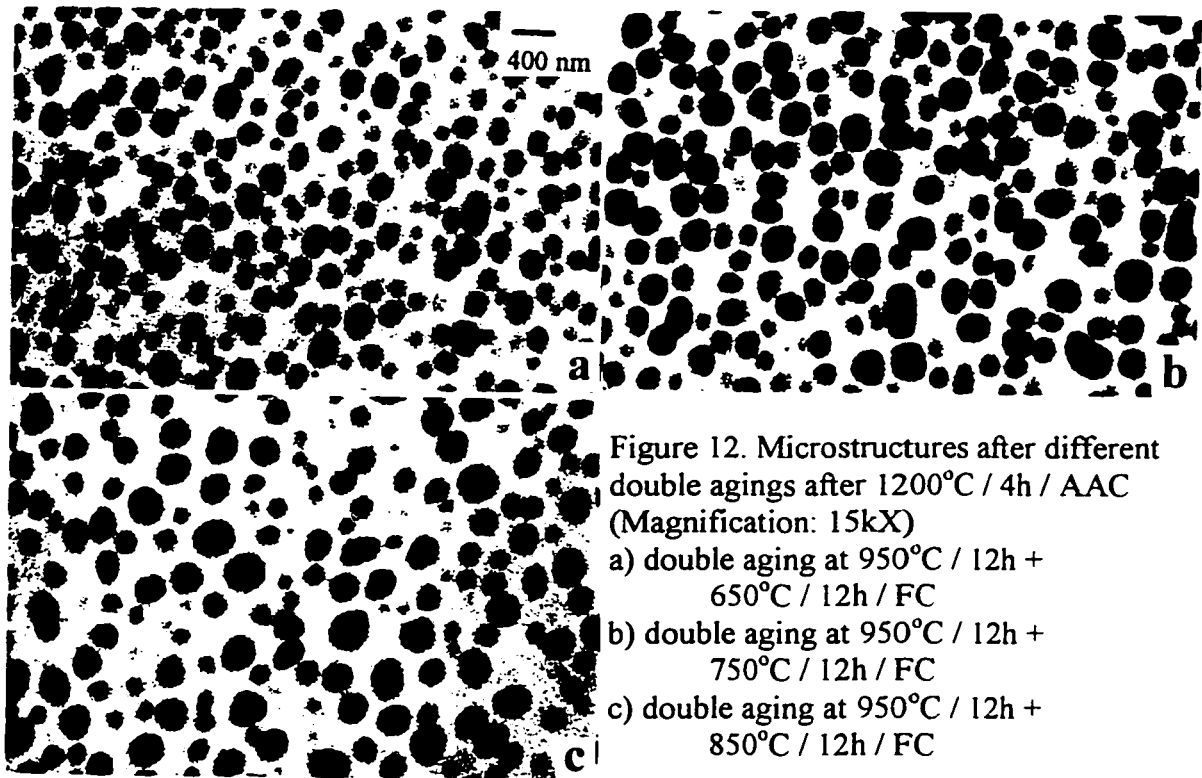


Figure 10. Microstructures after aging at different temperatures after 1250°C / 4h / AAC. (Magnification: 15kX)
a) single aging at 950°C / 24h / FC b) single aging at 1050°C / 24h / FC
c) single aging at 1200°C / 24 h / WQ d) single aging at 1200°C / 24 / FC





III.2. Microstructure Evolution in Polycrystalline Superalloy IN738LC in the Range 1120-1250°C

As explained in the previous section III.1, the precipitates coarsen to a maximum size of about 700 nm in cuboidal shape after 1120-1130°C/24h/FC aging treatments, Fig. 9f1, subsequent to the solution treatment of 1200°C/4h/AAC. Above this temperature, the duplex-size γ' precipitate morphology sets in at 1140-1150°C. The duplex-size microstructure consists of two extreme sizes of γ' precipitates, one very fine (~50-70 nm; size remaining nearly the same with changing time) and the other relatively coarse (size changing with time and temperature in the range). It was also already mentioned that

similar specimens aged for longer than 24h at 1120°C (e.g., 48 and 72h, Fig. 11g) after analogous solution treatment also showed the duplex-size γ' microstructure. In the range 1160-1225°C, a single-size fine γ' precipitate microstructure was observed, while at 1235 and 1250°C the single-phase solid solution matrix without any precipitate was obtained.

Two different solution treatments were applied to the specimens. As already stated, the one at 1200°C/4h/WQ yielded a fine size (~70 nm) precipitate microstructure as seen in Fig. 7, while the other at 1250°C/4h/WQ produced the single-phase solid solution matrix with no precipitates. Four experimental procedures were set up to study the mechanisms of the formation of the fine and duplex-size (coarse + fine) precipitate microstructures.

The first one, designated as Type-I heat treatment, consisted of holding (aging) the specimens at 1120, 1140, 1150, 1160, and 1180°C for different times after the solution treatment of 1200°C/4h/AAC (starting microstructure for aging treatments consisted of only fine precipitates, ~70 nm in size).

In the second procedure, after solutionizing at 1200°C/4h/AAC, the specimens were first aged at 1120°C/24h/FC to obtain the single-size unimodal-cuboidal precipitates with about 700 nm size, as seen in Fig. 9f1. Then, these specimens were aged at 1140, 1160, and 1200°C for different aging times to observe the dissolution of the big unimodal-cuboidal precipitates and the formation and growth of the finer ones. This procedure is designated as Type-II (starting microstructure for the second agings consisted only of maximum size cuboidal precipitates, ~700 nm in size).

In the third procedure, Type-III, the specimens were solution treated at 1250°C/4h to obtain the single-phase solid solution condition and then quickly transferred

to another furnace, already heated to 1140°C. The specimens were then aged at this temperature for different times. This procedure was set up to observe the evolution of the precipitates from the supersaturated solid solution without allowing any nucleation and growth that would happen at lower temperatures during reheating after quenching to room temperature from the solution treating temperature.

The fourth heat treatment procedure was named as Type-IV. In this, first the duplex-size precipitate microstructure, seen in Fig.13f, was developed in the specimens, then they were aged at 1160°C to observe the change in the duplex microstructure when aged at the fine precipitate formation temperature.

The results obtained after these four different types of heat treatments are described below.

III.2.1. Agings after the 1200°C/4h/AAC solution treatment, (Type-I):

These heat treatments were carried out to define the stability range for the duplex-size γ' microstructure in the range 1120-1200°C. After 1200°C/4h/AAC solution treatment, some of the specimens were aged at 1140°C for 1, 3, 5 and 30 min. and 2, 4, 12, 24, 48, and 96h. Initially, the precipitates coarsen and the duplex-size γ' microstructure could be observed after the aging treatments carried out for 30 min. or longer times. These microstructures are shown in Figure 13.

The duplex-size microstructure is found, likewise, at 1150°C after the Type-I treatment for 24h. This is evidenced by the microstructure in Fig. 14. The size and shape of the coarse precipitates in this sample are nearly similar to those formed after 24h at 1140°C (compare γ' sizes in Fig. 14 with those in Fig. 13h). However, it is noteworthy

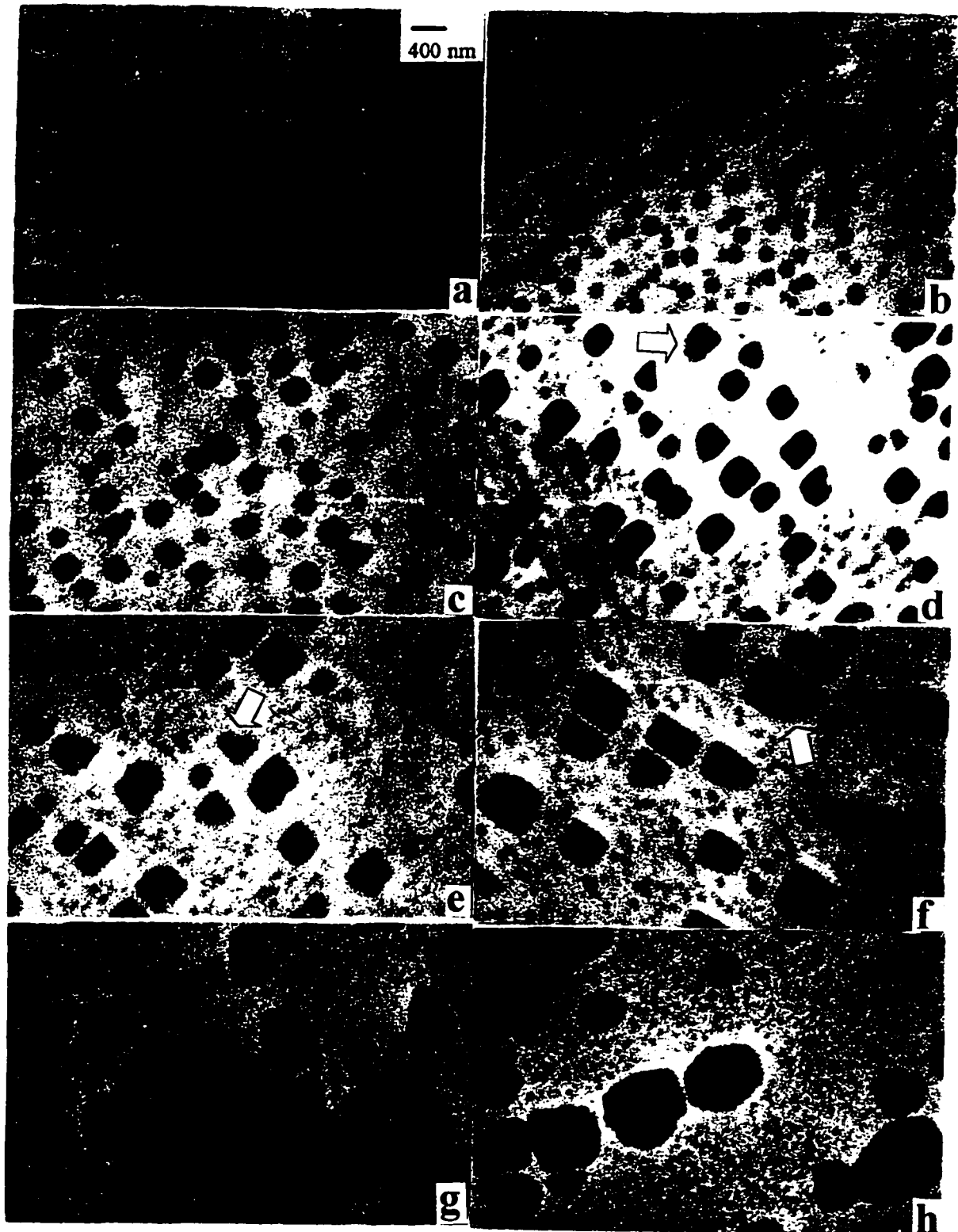


Figure 13. The duplex-size γ' precipitate microstructure obtained through Type-I heat treatment- $1200^{\circ}\text{C} / 4\text{h} / \text{AAC} + 1140^{\circ}\text{C} / t / \text{WQ}$ (Magnification: 15kX).

a) $t = 1\text{min.}$ b) $t = 3\text{ min.}$ c) $t = 5\text{ min.}$ d) $t = 30\text{ min.}$ e) $t = 2\text{h}$
 f) $t = 4\text{h}$ g) $t = 12\text{h}$ h) $t = 24\text{h}$ i) $t = 48\text{h}$ j) $t = 96\text{h}$

(Figure 13 continued)

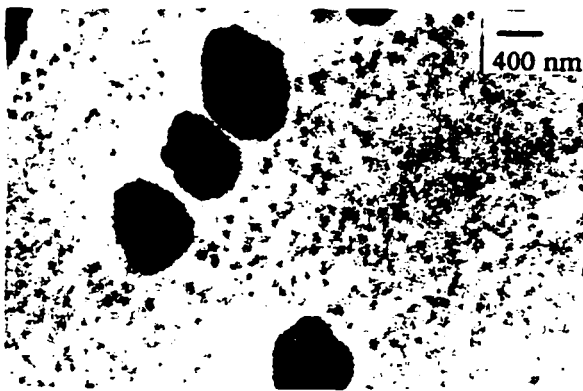
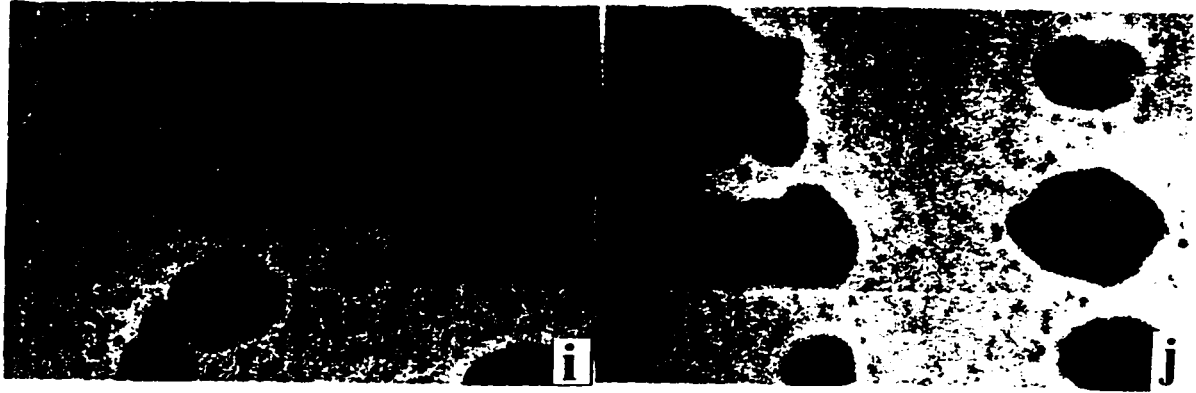


Figure 14. The duplex- size γ' precipitate microstructure obtained after Type-I aging at 1150°C / 24h / WQ subsequent to the solution treatment of 1200°C / 4h / AAC. (Magnification: 15kX)

that after aging at 1150°C, there is much less number of coarse precipitates, i.e., the volume fraction of the coarse precipitates is reduced at 1150°C. The duplex-size γ' microstructure was also obtained after aging at 1120°C for 48h and 72h via Type-I heat treatment, as already mentioned.

Agings by Type-I treatment at 1160, 1180, and 1200 °C yielded, however, the single-size fine precipitate microstructure with almost identical size (~70 nm) as already given for the solution treatment 1200 °C/4h/WQ.

The size of the fine precipitates in the duplex-size range showed no change with time, indicating that any large-scale growth of the fine precipitates does not occur during

aging. The coarse, growing-precipitates were cuboidal in shape up to 12h aging time and tended to become spheroidal or ellipsoidal at and above the 24h aging time. Note that the growing cuboidal precipitates show evidence of dissolution starting from 30 minutes, Fig. 13d. Dissolution of precipitates is clearer after longer time agings, Fig. 13e-j. It is clearly seen in the micrograph showing the microstructure obtained after aging for 24h, Fig. 13h, that the morphological change of cuboidal precipitates starts at the flat surfaces of the cubes. By addition of material onto flat surfaces (through coalescence with adjacent coarse precipitates), the precipitate shape changes from cuboidal to spheroidal. The bulged or irregular shaped coarse precipitates keep on growing through coalescence. This is clear in Fig. 13h, where one small precipitate is joining with a coarse one (bottom-right), and in Fig. 13i,j, where big agglomerated precipitates can be seen.

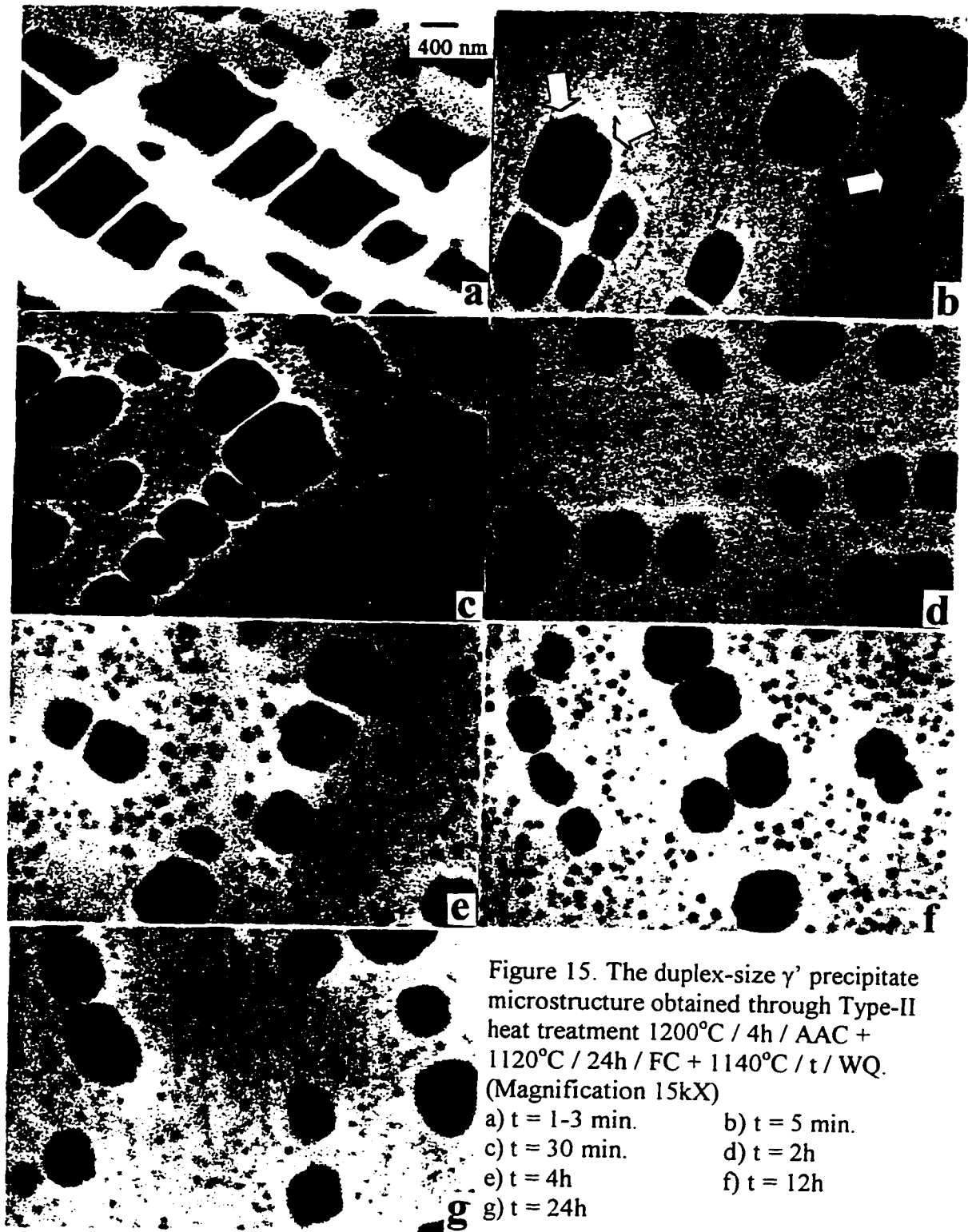
III.2.2. Agings after 1200°C/4h/AAC+1120°C/24h/FC heat treatments, (Type-II):

With an aim of elucidating the dissolution process of the coarse γ' precipitates and the nucleation and growth of the fine ones, first, the coarse cuboidal γ' microstructure, having no fine precipitates, was developed, Fig. 9f1, and later treated (aged for a second time) at 1140, 1160, and 1200°C for different times. The agings were carried out at 1140 and 1200°C for 1, 3, 5, and 30 minutes, and 2, 4, 12, and 24 hours, and at 1160°C for 15, 30, and 60 seconds and 5 and 30 minutes, and 2, 4, 12, and 24 hours. This was a more elegant way for studying the dissolution mechanism of the coarse and especially the formation and growth of the fine precipitates, since there was no fine precipitate in the starting microstructure, unlike in the case of Type-I heat treatment, wherein fine precipitates were already present after the first solution treatment step.

In this type of heat treatment, when the coarse-cuboidal precipitate microstructure was aged at 1140°C, the duplex-size precipitate microstructure was again obtained. The micrographs in Figure 15 show the microstructures obtained through Type-II heat treatment at 1140°C. It was observed that the fine precipitates formed in 5 minutes, and they were stable through all the aging treatments carried out up to 24h. Dissolution of the coarse cuboidal precipitates along cube corners can be observed after the 5 min. aging, indicated by arrows in Fig. 15b, leading to the spheroidal and ellipsoidal precipitate morphology with increasing aging time. In fact, after 5 min. at 1140°C, several coarse spheroidal particles had already been developed, see top right in Fig. 15b. During the dissolution process, the size of the coarse precipitates generally decreases with increasing time, as can be seen in Fig. 15a-g, and the coarse ones become spheroidal. Some coarse precipitates may also be splitting into two or three smaller ones in order to facilitate dissolution.

Fine-precipitate-free zones develop around the coarse ones and are indicative of fine precipitates merging with the adjacent coarse ones. These zones are clearly observable in Figs. 13 and 15.

Second agings at 1160°C yielded a partially fine precipitate microstructure after 15-60 second agings, Fig. 16. The complete transformation of coarse unimodal-cuboidal precipitates to fine ones was found to have taken place in as little as five minutes at 1160°C. Agings at 1200°C via Type-II treatments produced only the single-size fine precipitate microstructure in about one minute. Complete dissolution of the coarse precipitates with about 700 nm size seems to be possible in less than one minute at this temperature.



III.2.3. Agings after 1250°C/4h+1140°C/t/WQ heat treatments, (Type-III):

The aim of these treatments was to see if quenching first to room temperature after solutionizing had changed the nucleation and growth mechanisms and kinetics of the precipitates. Specimens were therefore quenched directly into the furnace kept at 1140°C from the solution treating temperature of 1250°C. Aging treatments were carried out thereafter at 1140°C for 1, 3, 5, and 30 minutes. The microstructures obtained through Type-III heat treatments were found to be quite similar to those obtained after Type-I heat treatments at 1140°C, shown in Fig. 13a-d. It is noteworthy that the duplex microstructure is also developed after 30 minutes in Type-III heat treatment as in Type-I treatment.

III.2.4. Agings after 1140°C/4h/WQ+1160°C/t/WQ heat treatments, (Type-IV):

After developing the duplex size microstructure by aging at 1140°C/4h/WQ, the second aging was carried out at 1160°C for 15, 30, and 60 seconds to observe any change in the duplex size microstructure at the fine precipitate formation temperature. Gradual reduction in the size of coarse precipitates was observed with increasing time as illustrated in Fig. 17.



Figure 16. The partially fine precipitate microstructure obtained through Type-II heat treatment- 1200°C / 4h / AAC + 1120°C / 24h / FC + 1160°C / t / WQ. t=15, 30, and 60 s. (Magnification: 15kX)

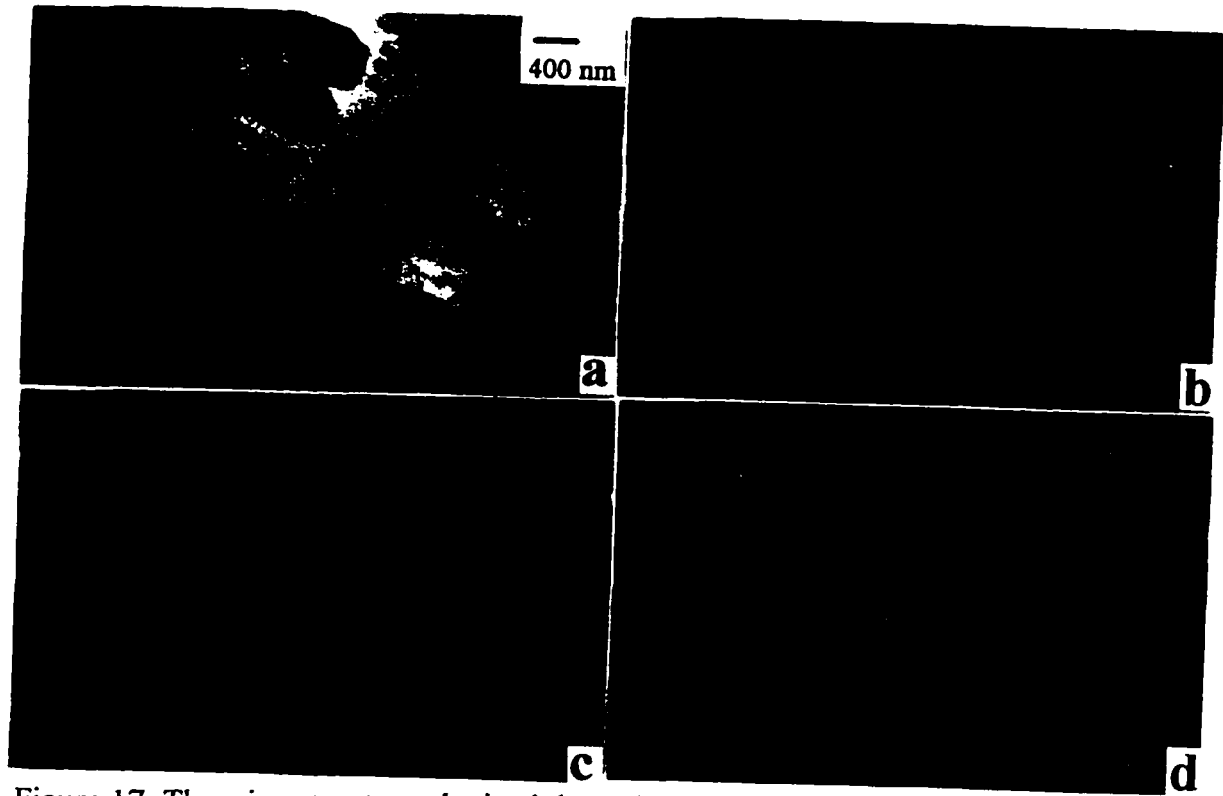


Figure 17. The microstructure obtained through Type-IV heat treatment-
1200°C / 4h / AAC + 1140°C / 4h / WQ + 1160°C / t / WQ
(Magnification: 15kX)

a) t= 15 s

b) t= 30 s

c1) t= 60 s

c2) same specimen as c1 showing different area.

**CHAPTER IV. RESULTS AND DISCUSSIONS:
PRECIPITATE GROWTH/DISSOLUTION
MECHANISM AND KINETICS IN IN738LC**

IV.1. In the Range 650-1120°C.

Two different precipitate growth mechanisms were observed. Precipitate growth was by merging of smaller precipitates into larger ones during the 1120°C/2h solution treatment followed by any type of aging treatment. This can be seen in Fig. 6c,d and Fig. 8b. Such a merging mechanism leads to conversion of cuboidal precipitates, possibly, to oval-shaped or spheroidal type. It is obvious that incomplete coalescence is due to the lack of adequate thermal energy and/or diffusion time at this temperature (1120°C or below) required for the process. Precipitate growth mechanism after the 1200°C/4h or 1250°C/4h (AAC or WQ) solution treatments followed by any aging treatment could be via solute ejection from the supersaturated solid solution and addition to the growing precipitate, since there is more volume fraction of the precipitate found at lower temperatures than at higher temperatures. At a given temperature, precipitate coarsening over a long time period should be occurring by the Ostwald ripening. Also, coalescence of adjacent particles seems to be another mechanism for the growth of the precipitates during the aging heat treatment at a high enough temperature, as can be seen in Fig. 11g, shown by an arrow. Particle coalescence also was observed by Malow et al. [11]. This topic is discussed in detail in section IV.3.

During aging, γ' precipitates grow to a certain size, and further coarsening of the γ' occurs during FC, aided primarily by solute ejection from the matrix solid solution (precipitate consolidation dominates in duplex precipitate-size microstructures, as already pointed out). This fact is brought about by comparing the precipitate sizes in Figure 9 for

the FC-condition with those in Figure 11 for the WQ-condition of an analogous sample. The higher volume fraction of the γ' precipitates obtained after FC indicates the fact that solute ejection from the matrix continues during FC, aiding the further precipitate growth. The larger precipitate size obtained after FC is due to the longer time available for the diffusion of the solute atoms than in the case of WQ. Further coarsening during furnace cooling can also be deduced from Figure 18. In this figure, the precipitate size in logarithmic scale is plotted against the inverse temperature. For all the aging temperatures shown in the plot, the precipitate size is larger for the FC condition. In addition, it is important to note that there is an abrupt increase in precipitate size noticed above 1050°C for both the FC and WQ conditions, which points probably to another accelerated mechanism for precipitate growth in this range. Also, similarity in the precipitate sizes in the solution-treated microstructure (in the AAC or WQ condition) and in the ones obtained after agings at any temperature at and below 750°C is due to the vastly decreased diffusivity at these low temperatures.

Figures 9f1 and 9f2 show two different precipitate growth morphologies. These two (cuboidal and triangular, the latter possibly formed by cubes/diamonds splitting over octahedral $\{111\}$ planes) precipitate shapes were observed in the same sample at different locations, and the morphology difference can be due to the difference in grain orientations. Cuboidal growth occurs on $\{100\}$, and octahedral growth is on $\{111\}$ planes of the FCC-superlattice [95,96]. Octahedral morphology is indicated by the presence of equilateral triangles in Figure 9f2. This is the first time the triangular or the possible octahedral growth has been identified in the superalloy IN738LC.

The largest unimodal-cuboidal precipitate size via water quenching after the aging treatments was obtained after aging at 1120°C/24h/WQ (Fig. 11f). Surprisingly, after agings for longer time periods (48 and 72 hours) at this temperature, a duplex-size precipitate microstructure formed, as seen in

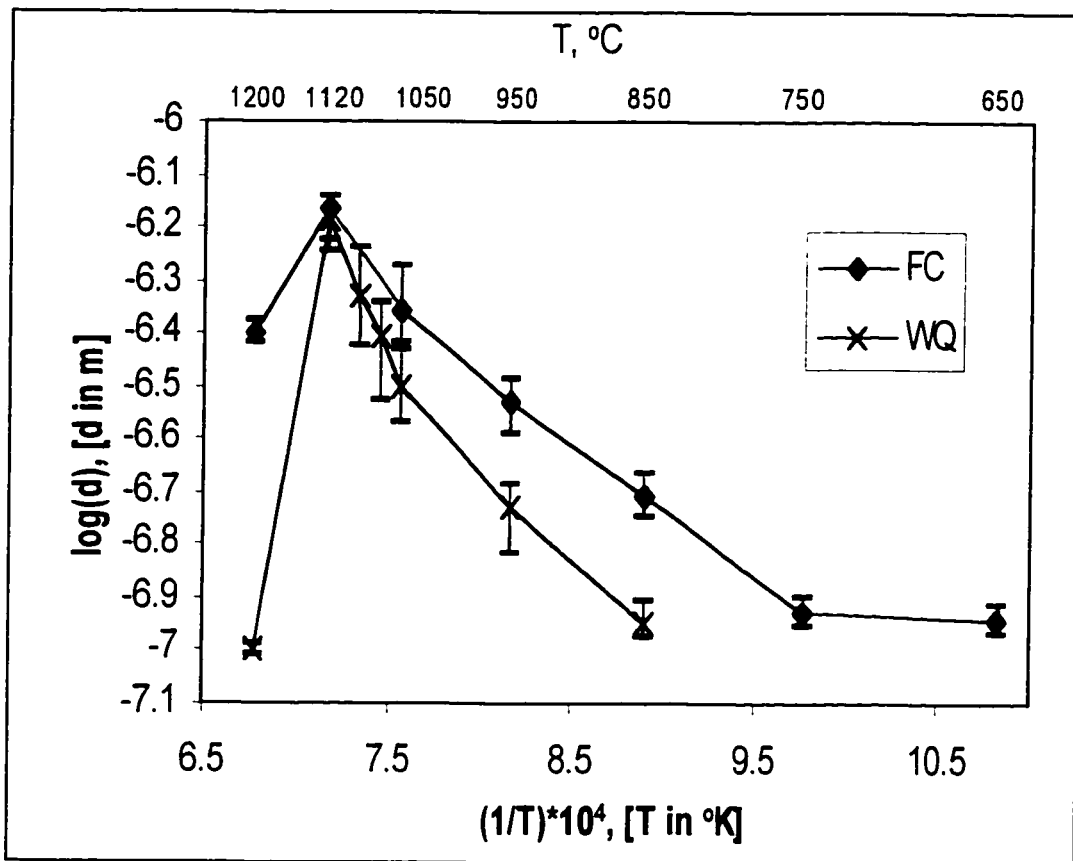


Figure 18. Plot of $\log(d)$ vs. $1/T$ of gamma prime precipitate size derived from Figs. 9&11 and data given in Table III. (d is average precipitate size after the heat treatment 1200°C/4h/AAC + T/24h/(WQ or FC), where T is the aging temperature)

Fig. 11g, and at still higher temperatures (1140-1150°C), this occurred in a much shorter time (30 min.); further, a precipitate refinement leading to the formation of single-size fine precipitates was observed in the range 1160-1225°C. Fine precipitates were obtained after the treatment 1250°C/4h/AAC (single phase solid solution) followed by the 1200°C/24h/WQ aging treatment, and the resultant microstructure, shown in Fig. 10c, is exactly similar to the one shown in Fig. 7 for those solution treated at 1200°C for various time periods. Figure 10d shows the agglomerated precipitates of medium size, obtained after 1250°C/4h/AAC followed by 1200°C/24h/FC. Growth and agglomeration of precipitates, obviously, should have taken place during furnace cooling. This can be readily understood by comparing Figures 10c and 10d, showing the aforementioned microstructures for the two conditions. In Figure 10d, the precipitates are not grown to a larger size because growth occurs during subsequent FC by consolidation of fine precipitates, which would be present at 1200°C. Results of further study and analysis pertaining to γ' dissolution and precipitate refinement is given in section IV.2 and coarsening features in IV.3.

Precipitate sizes (average diameter for spheroidal, cube edge for cuboidal, and average edge length for rectangular) were measured using the micrographs after various heat treatments, given in Figures 9 and 11, and the data is given in Table 3. Precipitate growth data was analyzed by using the following well-known growth equation, given in Ref. [97]:

$$d^n - d_0^n = Kt \quad (2)$$

$K = K_0 \exp(-Q/RT)$, where d_0 and d are the initial and final precipitate size, respectively, t is the time, n is the growth exponent, and K is a growth rate parameter

involving the interface energy between γ' and the matrix and the interface mobility. From the plots of precipitate growth data given in Figure 18, Q, the activation energy for the γ' precipitate growth, was calculated to be 150 kJ/mol in the range of 750-1050°C (FC1) and 298 kJ/mol in the range of 1050-1120°C (FC2) for the FC condition (precipitate sizes after FC plotted against the aging temperature), and 191 kJ/mol in the range of 850-1050°C (WQ1) and 350 kJ/mol in the range of 1050-1120°C (WQ2) for analogous WQ condition, by taking $d_0=0$ and $n=3$. The growth exponent n in Eq. (2) was calculated to be 3.1 from the precipitate size data obtained after different aging times at 1120°C, and it is rounded to 3 in the calculations, as is normally done. The initial precipitate size, d_0 , is also taken as zero because heat treatments after both the solution treatments at 1250°C, which produces a single phase supersaturated solid solution, and 1200°C, which produces a refined fine size (~70 nm) precipitate microstructure, yield similar size precipitates in the final microstructure. Therefore, using a zero initial precipitate size would not give rise to any vast error in the calculations. It can be noted that the precipitate size data from the FC condition gives about 50 kJ/mol less activation energy than that obtained from the analogous data in the WQ condition. Activation energy for precipitate growth of IN738LC is given to be 330 kJ/mol for the AC condition in Ref. [11]. In Ref. [51], corresponding Q for Nimonic-105 is given to be 266 kJ/mol.

IV.2. In the Range 1120-1250°C.

The precipitate sizes (average diameter for spheroidal and cube edge for cuboidal ones) were measured using the micrographs after various heat treatments, given in Figs. 13-15, and the size data derived from them is given in Table 4. The precipitate size vs. aging time is plotted in Fig. 19 for Type-I heat treatment along with the superimposed

Table 3. Size of the γ' precipitates in FC and WQ conditions after aging for 24h at the given temperature subsequent to 1200°C/4h solution treatment.

Aging temperature, °C		650	750	850	950	1050	1070	1090	1120	1200
Precipitate Size, nm	FC-condition	115 (1765) [±6]	118 (1582) [±6]	196 (640) [±9]	294 (250) [-13/+10]	436 (120) [-12/+21]			700 (50) [-18/+5]	400 (120) [±5]
	WQ-condition			112 (1080) [-6/+10]	187 (430) [-19/+10]	315 (135) [-14/+18]	395 (72) [-25/+15]	468 (58) [-20/+22]	655 (32) [-25/+10]	70 (1800) [±3]

First line in each data cell gives the average precipitate size, second line number of precipitate particles averaged, and third line % deviation in size of the precipitates. Number of precipitates is given in a 4x5 in.² area.

precipitate size data of Type-II heat treatment. In this figure, the data for Type-I heat treatment represent two types of precipitate growth, normal and abnormal; the latter falls in the linear portion of the plot after an initial non-linear part showing the normal growth. The plot of $\log(d)$ vs. $1/T$ for the Type-I heat treatments at different temperatures (1120, 1140, and 1150°C) for the same time period (24h) is shown in Fig. 20.

Table 4. Size data of the γ' precipitates after various heat treatments. (size is given in nm)

Solution treatment and first aging	Time: t, (h)	0.083	0.50	2.0	4.0	12	24	48	96	240	
	Final aging										
1200°C/4h WQ	1140°C/t/WQ	260 (170) [±5]	300 (125) [±5]	386 (80) [±5]	440 (59) [-6/+10]	538 (45) [-16/+9]	622 (28) [-22/+25]	760 (19) [-10/+15]	1035 (12) [-15/+26]		
	1150°C/t/WQ						607 (38) [±18]				
	1160°C/t/WQ						70 (1800) [±3]				
	1180°C/t/WQ						70				
	1200°C/t/WQ	70	70	70	70	70	70	70	70	70	
1200°C/4h WQ	1140°C/t/WQ	683 (25) [-20/+9]	665 (26) [-18/+9]	655 (26) [-21/+10]	650 (26) [-16/+8]	638 (28) [-15/+8]	620 (30) [-18/+10]				
	1160°C/t/WQ	70	70	70	70	70	70				
1120°C/24h FC	1200°C/t/WQ	70	70	70	70						

First line in each data cell gives the average precipitate size, second line number of precipitate particles averaged, and third line % deviation in size of the precipitates. Number of precipitates is given in a 4x5 in.² area.

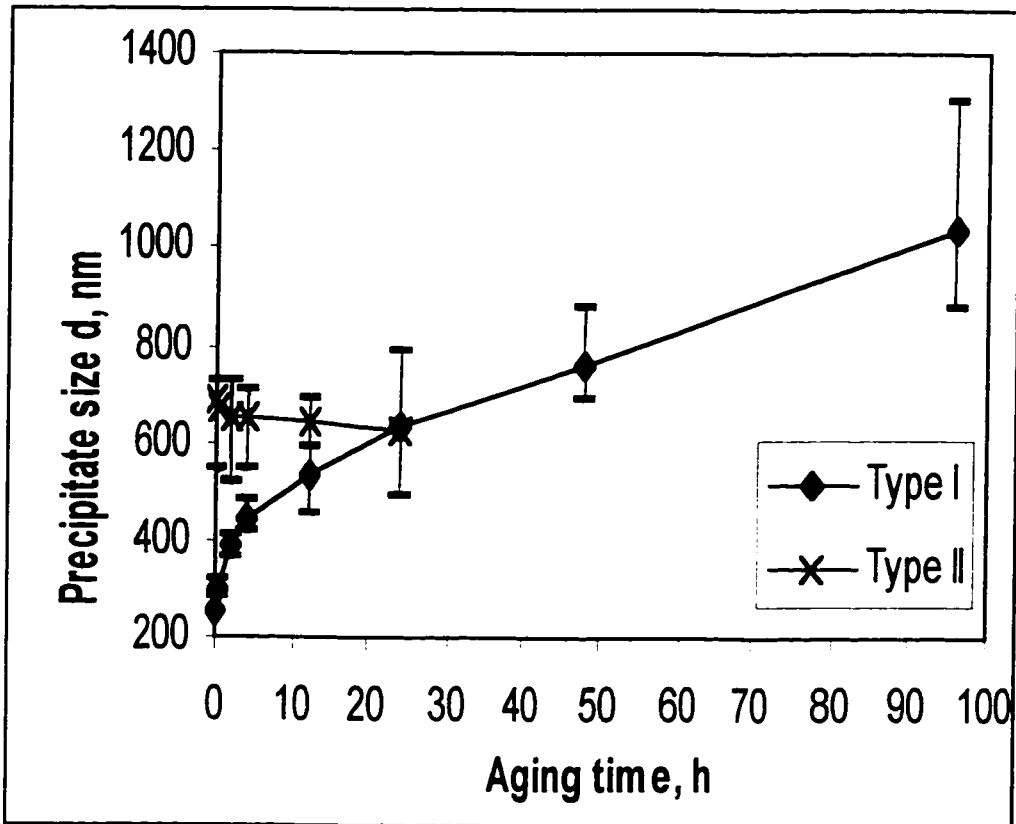


Figure 19. The plot of precipitate size vs. aging time for Type-I heat treatment at 1140°C, (1200°C/4h/WQ+1140°C/t/WQ), along with analogous plot of precipitate size data for Type-II heat treatment at 1140°C, (1200°C/4h/WQ+1120°C/24h/FC+1140°C/t/WQ).

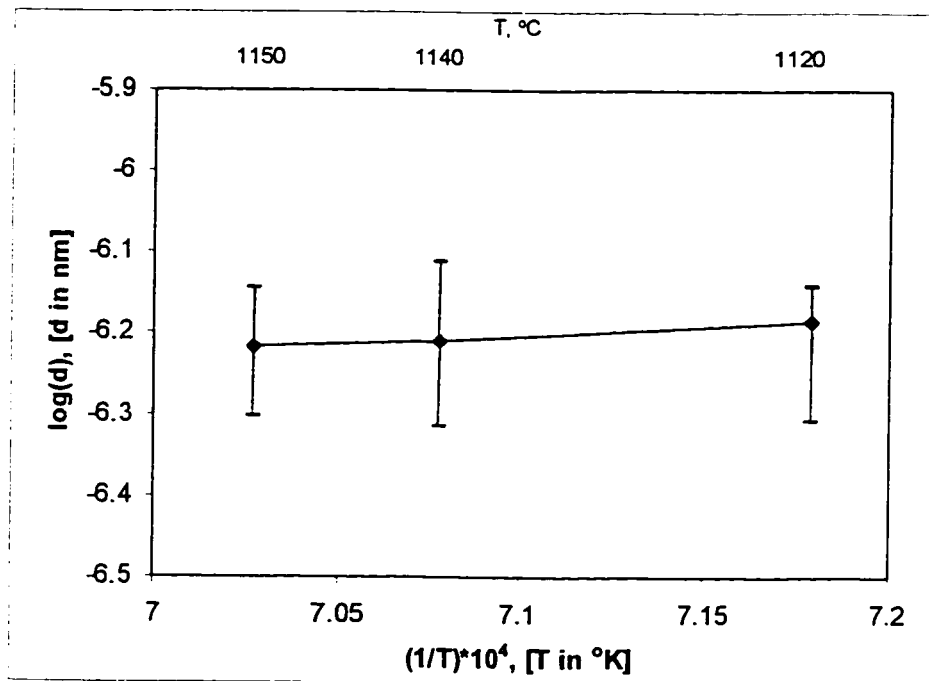


Figure 20. The plot of $\log(d)$ vs. $1/T$, derived using the precipitate size data after Type-I heat treatment at 1120, 1140, and 1150°C for 24h/WQ (data given in Tables III and IV for the corresponding microstructures)

Activation energy calculations were carried out using the precipitate sizes of only the coarse cuboidal ones. Three different activation energies were calculated, two values for dissolution using first the precipitate sizes obtained after agings at different temperatures for the same holding time (Fig. 20) and second using the precipitate sizes obtained through the Type-II heat treatment (Fig. 19), and one activation energy for precipitate growth at 1140°C using the sizes obtained after different holding times (non-linear portion of the curve corresponding to Type-I treatment in Figure 19).

It has been reported that the precipitate dissolution process could be treated as the reverse of the growth process [95]. In this case, using the same kinetic equation to calculate the activation energies for the growth and dissolution processes would not create any serious error. The well-known kinetic equation for precipitate growth that is already given in Equation (2) is employed in the activation energy calculations. K_0 in this equation is a constant parameter, which is taken to be negative for the dissolution process and positive for the growth.

The activation energies for the dissolution process using the precipitate sizes obtained through two different heat treatments, one after the Type-I agings at different temperatures (1120, 1140, and 1150°C) for 24h (Fig. 20) and the other after Type-II heat treatment at 1140°C for different times (Fig. 19), are calculated to be 110 kJ/mol and 85 ± 20 kJ/mol, respectively. A value of 685 ± 15 kJ/mol was obtained for the growth of coarse precipitates in the duplex-size microstructure at 1140°C. In the activation energy calculation for the dissolution process using the size data at different temperatures, the slope of the plot, given in Fig. 20, was employed. However, activation energy calculations for the dissolution or for the growth processes of the coarse precipitates at a

constant temperature (1140°C) require that the corresponding K_0 values be known in advance. The $\log(K_0)$ value for the latter calculation (for growth at 1140°C) was obtained as 6 from the precipitate size data of analogous aging treatments in the water quenched condition in the temperature range 1050-1120°C, see section IV.1; the value of 16 for $\log(K_0)$ obtained from Fig. 20 is used for the former (for dissolution at 1140°C). No activation energy calculation for the formation or for the growth of the fine precipitates of the duplex-size microstructure was possible, since no measurable precipitate growth was observed for these precipitates at the magnification used (15kX).

IN738LC shows the duplex-size γ' microstructure when quenched from the temperature range 1120-1150°C. Up to 1130°C, γ' phase has only the single-size coarse precipitate morphology after the 24h aging treatment, but acquires the duplex-size character after 48h or longer time agings. This implies possibly the prevalence of a maximum critical size beyond which dissolution of coarse precipitates and formation of the duplex-size precipitate morphology will be favored at temperatures slightly below the stable duplex-size range of 1140-1150°C. When quenched from the range 1160-1225°C, the alloy has only the refined precipitate microstructure. It is significant that these fine γ' precipitates do not grow to any bigger size even after 10 days of holding time at 1200°C. Likewise, they do not grow even in the duplex-size microstructure in the range 1120-1150°C.

In the early stages of the aging treatments, the very fine precipitates form after all of the three experimental procedures (Type-I, Type-II, and Type-III). This happens even in as little as 5 minutes from coarse precipitates at 1140°C and in 15 seconds at 1160°C

both via Type-II aging treatments. The fine precipitates of the duplex microstructure, however, form in 30 minutes at 1140°C via Type-I aging treatment. The source for the formation of the fine precipitates is possibly the dissolution of some of the smaller newly grown cuboidal precipitates in the case of Type-I heat treatments, and the “corner dissolution” of coarse cuboidal precipitates in the case of Type-II and Type-III heat treatments, as pointed out by an arrow in Fig. 13d,e,f. The size of the fine precipitates in the duplex microstructure is smaller than that of the precipitates in the 1200°C solution-treated microstructure, which is the starting microstructure for all of the aging treatments. This fact can be realized by comparing the size of fine γ' precipitates in Fig. 7 and Figs. 13, 15. The reason for this conflicting observation is that at the very early stages of the Type-I and Type-III heat treatments (i.e., within the first 30 min. of holding time at 1140°C), fine precipitates of the solution-treated microstructure would merge and form the growing-cuboidal precipitates (see Fig. 13), and at some stage of the agings, smaller sized ones among them would dissolve and reprecipitate in the matrix in the form of very fine secondary precipitates. It appears that in the stable duplex-size precipitate region critical coarse size is not needed and hence medium or small size coarse precipitates could dissolve to form the secondary fine precipitates. During this reprecipitation, the equilibrium size is smaller than the one obtained after the 1200°C solution treatment probably because there is not enough solute supply in the matrix for the fine precipitate growth. The same explanation applies also for the Type-II heat treatments because the “corner dissolution” is not enough to enable the growth of the very fine precipitates. However, it is clear that the size of the very fine precipitates should slowly rise to that of

1200°C solution-treated microstructure after all of the coarse precipitates dissolve with increasing temperature.

It is obvious that the formation of very fine precipitates is a rapid process. Likewise, the dissolution of most of the coarse precipitates at 1160°C is a fast process, which yields the partially fine precipitate microstructure in as little as 15 sec., Fig. 16. One important feature of Fig. 16 is that the size of the fine precipitates has already grown to the size of the fine precipitates obtained after the 1200 °C/4h/WQ solution treatment given in Fig. 7 in as little as 15 sec. Further, the very fine precipitates of the starting duplex microstructure seem to have grown to the normal fine precipitate size in such a short time in Type-IV treatment, Fig. 17. It should be noted that dissolution or splitting of the coarse precipitates might continue until their size drops down to the equilibrium size of about 70 nm for the fine precipitate microstructure. The solute atoms released from the coarse precipitates via either dissolution or splitting feed the very fine precipitates of duplex microstructure to grow them to the equilibrium size.

Dissolution of the coarse-cuboidal precipitates after Type-I and Type-II heat treatments has already been demonstrated. Through Type-II heat treatment, one sees the dissolution of the maximum-sized precipitates, whereas the results of Type-I heat treatments show the continuing growth of some of the precipitates through coalescence, leading to very large precipitate sizes of a few among them. In the duplex-size precipitate range, the dissolution of the big cuboidal precipitates in Type-II heat treatment continues with time. After the 24h aging time, the size of the coarse precipitates reaches that of the coarse precipitates in Type-I heat treatment for the same aging time, see Figs. 13h and 15g and also Fig. 19. This observation indicates that a size close to this is possibly the

equilibrium size for the coarse precipitates for the 24h aging time at 1140°C. Beyond 24h, the precipitate shape is nearly spheroidal, and the growth of a few precipitates is continued in Type-I heat treatment in this morphology, see Fig. 13.

The morphological transformation of the precipitates from cuboidals to spheroidals can be attributed to the need for reduction in surface area for the coarse cuboidal precipitates. Normally, a low interfacial energy term between the precipitate and the matrix compared to the other transformation energies allows for the precipitate growth through solute pick-up from the solid solution matrix (Ostwald ripening). In the present case, however, the morphological transformation (from cuboidal to spheroidal) indicates that the interfacial energy of the coarse precipitates is probably high, and coarsening is favored by the further reduction in surface area through spheroidization after coalescence of particles. Conversely, one can argue that cuboidal flattening of the surfaces of the very large size particles is not favored, since that could increase the surface area.

Because of the fact that the materials thermodynamically prefer the lowest possible total interfacial energy, it appears that the coarse γ' precipitates dissolve at higher than a critical temperature and/or size due to possibly a reduction in interfacial energy and reprecipitate as many very fine ones. This enables the accommodation of larger interfacial area. The overall interfacial energy is kept approximately unchanged. At 1120-1150°C, the γ' precipitates grow to a certain maximum size in cuboidal shape, and above this critical size, further growth is apparently favored only in the spheroidal morphology. The duplex-size microstructure obtained at 1120°C for 48 and 72 hours aging treatments is also an indication of the precipitate size and interfacial energy effect

for the formation of such a duplex microstructure. Since at this temperature a single-size coarse cuboidal γ' morphology was obtained up to 24h aging treatment, it is apparent that after reaching a certain size, the cuboidal precipitates start to dissolve and reprecipitate as fine ones, leading to the duplex-size precipitate microstructure. In addition, formation of the duplex-size microstructure in a shorter span of time via Type-II treatment (5 min.) than Type-I and Type-III treatments (30 min.) at 1140°C is an evidence for the size effect on the formation of duplex-size γ' microstructure. Moreover, dissolution or splitting of the maximum sized coarse precipitates and formation of the partially fine size precipitate microstructure at 1160°C occurs in as little as 15 seconds. Also, comparing Fig. 16 and Fig. 17, in which the specimens were final-aged at 1160°C, it is seen that the number of coarser precipitates is higher in Fig. 17. The size of coarse precipitate in Fig. 17 initially was much smaller than that of the coarse ones in Fig. 16, 450 nm vs. 700 nm, respectively. This initially smaller size of the coarse precipitates in Fig. 17 might have helped in the retention of more of them after very short aging at 1160°C. Furthermore, the coarser the precipitates, the faster they seem to dissolve. These experimental facts then strengthen the conclusion that the formation of fine size precipitate microstructure at highest possible temperature is determined perhaps by the sharp reduction in the interfacial energy.

Alternatively, one can argue that the fine precipitates formed after quenching from the range 1160-1225°C and the very fine precipitates of the duplex-size morphology are nucleated and grown at some lower temperature range during cooling by water quenching. The different times involved in forming the fine precipitates would then relate to the amount of the solute in the matrix introduced by the dissolution process. Higher

the temperature, faster will be the dissolution and enrichment of solute and quicker the precipitates will form. Lack of coarsening of the fine precipitates can then be understood, since in all cases the fine precipitates form during quenching through the same temperature range and hence the size and distribution will remain the same.

A careful analysis of the precipitate shapes in Fig. 9f1 shows that the radius around the corners of the cuboidal precipitates is the smallest and the corners are the sharpest for the precipitates with the maximum size obtained at 1120°C/24h/FC. According to Gibbs-Thompson relationship, Equation (3), solubility increases as the radius decreases [98].

$$X_{A,r}^{eq} = X_{A,\infty}^{eq} \exp(2\gamma V_m / rRT) \quad (3)$$

where $X_{A,r}^{eq}$ denotes the equilibrium solubility of precipitate A of radius r , $X_{A,\infty}^{eq}$, the equilibrium solubility of A of infinite large radius, γ , the interfacial energy between the precipitate and the matrix, V_m , the molar volume of the precipitates, R , the universal gas constant, and T , the absolute temperature. Hence, the decreased corner radius of the precipitates should facilitate their dissolution process at the corners.

The dissolution may progress either on $\{111\}$ or on $\{110\}$ planes. The reason for dissolution starting at the corners or on the edges of the cube is due to the fact that the surface energy, γ , of the FCC crystal structure, which is the crystal structure of the γ' precipitates, is the lowest on $\{111\}$ and $\{110\}$ planes, respectively (in proportion 0.577 to 0.589, as opposed to 0.667 for the $\{100\}$ planes), according to the Equation (4) [98,99].

$$\gamma_{(h,k,l)} = N_b(\Delta H_s / 12N_A)N_s \quad (4)$$

where N_b denotes the number of broken bonds per atom (4,5, and 3 for the $\{100\}$, $\{110\}$ and $\{111\}$ planes, respectively), ΔH_s the molar enthalpy of sublimation (breaking all of the bonds), N_A the Avagadro's number, and N_s the atomic density of the plane. Dissolution lowers the surface area, and the need for morphological change of the precipitates from cuboidals to the spheroidal ones is perhaps another reason for "corner dissolution" parallel to $\{111\}$. Through this dissolution process, the FCC crystal of γ' is trying to attain the equilibrium shape of a cubo-octahedron [95,96,98,100] which has the lowest surface area next to spheroidal shape. Also, dislocations present on $\{111\}$ planes facilitate the dissolution on these planes. Similar findings were reported by Batterman in Ref. [101]. He observed that dislocations on $\{111\}$ and $\{100\}$ planes of FCC germanium single crystals facilitated the dissolution on these planes, and these planes became the bounding surfaces, leading to a cubo-octahedron shape. Another fact in favor of the corner dissolution parallel to the $\{111\}$ planes is the observation of triangular-shaped precipitates as given in section III.1 and discussed in section IV.1. Presence of equilateral triangular precipitates indicates the growth parallel to the octahedral $\{111\}$ planes. Therefore, it could be argued that the precipitates would prefer dissolution parallel to the octahedral planes as well, since they prefer these planes during growth.

The abnormal growth of a few precipitates by merging can also be explained on the basis of the need for reduction in total surface area and to prevent an increase in the overall surface energy. Smaller particles migrate as a whole to the nearby coarse particles and coalesce in the duplex-size microstructure. Adjacent coarse particles could migrate and coalesce with each other as well at relatively high temperatures. This would indicate that the matrix is considerably softened to enable such migration. Close to the solidus

point of the alloy (1270-1280°C) [12], this can be expected. Also, an attractive force between such agglomerating particles can be postulated. This aspect of precipitate agglomeration is being discussed in the following section, IV.3.

Up to 1130°C, the microstructure indicates coarse γ' precipitates which keep on growing by coalescence. As stated earlier, the interfacial energy must be larger at and below 1130°C due to the lower precipitate-matrix overall interfacial area than that of the duplex microstructure obtained after quenching from the range 1140-1150°C. Single size fine precipitates, large in number and present after quenching from the temperature range 1160-1200°C, would have much larger overall interfacial area. In this higher temperature range the interfacial energy should be small enough to enable stability of fine precipitates, if they are formed and retained in the temperature range 1160-1225°C. However, if they are nucleated and grown in a lower temperature range during quenching, their formation can be accounted for easily as due to the overall reduction in free energy. Necessity of low enough interfacial energy to enable the matrix to keep large number of precipitates with fine size at high temperatures is also reported for superalloys in Ref. [98]. At still higher temperatures, 1235°C, the single-phase solid solution matrix, with no precipitate phase, has been obtained. That the material has possibly lower interfacial energy between the fine γ' particles and the matrix at temperatures close to the single-phase solid solution field (which itself should be very close to the solidus temperature in this alloy, ~1270-1280°C) than at lower temperatures is understandable as a temperature effect. If the fine precipitates are formed during quenching from a high temperature after the start of the precipitate dissolution process above about 1140°C, why such fine precipitates are not

formed during quenching from the temperature range 1235-1250°C cannot be explained from the available data.

Close to the boundary of single-size coarse γ' structure, i.e., at 1140°C, the coarse γ' precipitates in the duplex-size microstructure keep on growing, while at 1150°C, close to the single-size fine γ' structure, they show a greater tendency for dissolution, and reduction in size. The very fact that the material seemingly prefers the single fine-size precipitate microstructure at higher temperatures in the range 1160-1225°C or forms these fine precipitates during water quenching from this temperature range is an interesting finding. Absence of coarsening of fine precipitates in this temperature range would be easily explainable if the latter were true. If such were the case, the alloy should be single phase at temperatures above 1160°C, but forms the fine precipitates only while quenching from the range 1160-1225°C. Quenching from the single phase condition above 1225°C does not lead to the nucleation and growth of the fine precipitates due to some unknown reason.

Coarse precipitates are obtained from the fine ones of 1200°C solution treatment which have been retained at room temperature by water quenching. This indicates possibly that both the fine and coarse precipitates should be of similar composition and structure. Also, X-ray diffraction analysis has confirmed that the two different precipitates with coarse and fine sizes have the same structure (FCC) and lattice constant.

The equilibrium of two distinctly different sizes for the precipitate phase after quenching from the range 1120-1150°C is also a new finding. It appears that quenching from this range of temperature, the alloy prefers to have the two different sizes for γ' and

split the overall interfacial energy into two components, one coming from the coarse and the other from the fine precipitates.

Assuming that the overall volume fraction of γ' is nearly the same, the following expression should hold:

$$(A_c \gamma_c)_{1120^\circ\text{C}} \sim (A_{dc} \gamma_{dc} + A_{df} \gamma_{df})_{1140-1150^\circ\text{C}} \sim (A_f \gamma_f)_{1200^\circ\text{C}} \quad (5)$$

where A denotes the overall interfacial area and γ , the unit interfacial energy of the respective sizes. The subscripts c, dc, df, and f denote the coarse, coarse in the duplex-size (intermediate) range, fine in the duplex-size range, and the fine precipitate sizes, respectively. It is assumed that the precipitates of various sizes and distribution are stable at temperatures indicated. Then, it can be hypothesized that γ_c should be far greater than γ_f . Then only the intermediate stage of duplex-size γ' morphology would be feasible. As stated earlier, A_f should be far larger than A_c . Also, γ_f at 1200°C should be very small to prevent agglomeration of the fine precipitates at this temperature when the holding time is increased, if indeed the fine precipitates are present at 1200°C. Even so, coarsening of some precipitates due to random fluctuation of energy and motion of particles can be expected. Since all of the precipitates are of the same size, it indicates strongly the possibility that they are formed during quenching at a lower temperature.

In the final stage of dissolution, observed after 1160°C/(5min.-24h)/WQ aging treatment, the material shows the unimodal size, which is the same as that of the 1200°C solution-treated microstructure. Reduction in precipitate size creates more new surfaces, which should be brought forth by the vast reduction in surface energy at these very high temperatures, as pointed out above, if the fine particles are stable at 1160°C and above till

1225°C. Any coarse precipitate formed during heating is redissolved in the matrix leading to the formation of single-size fine γ' precipitates in the temperature range 1160-1225°C.

The activation energy calculations confirm that the precipitates are mainly in the dissolution mode in the range 1140-1150°C, not in the growth. The activation energy for the γ' growth in the range 1050-1120°C was reported earlier as 350 kJ/mol in section IV.1. The activation energies calculated in the range 1120-1150°C for the growth and the dissolution processes of the coarse precipitates of the duplex-size microstructure show very distinct values. The activation energy for the dissolution process of the γ' precipitates in Type-I treatment, calculated using the sizes obtained in the range 1120-1150°C (duplex-size microstructure range), is 110 kJ/mol, which is far below the one obtained for the growth in the range 1050-1120°C, given in the previous section. The other activation energy for the γ' dissolution was obtained from Type-II heat treatment. Type-II heat treatment is a double aging process (after solutionizing, aging first at 1120°C to produce the maximum size cuboidal precipitates and then at 1140°C to study their dissolution), as mentioned earlier. The activation energy calculated for dissolution in this heat treatment process is 85 ± 20 kJ/mol. The activation energy values calculated for the dissolution of coarse precipitates via the two different heat treatment processes are fairly close to each other. The activation energy for the normal growth of precipitates in Type I heat treatment at 1140°C is calculated to be 685 ± 15 kJ/mol, which is nearly twice the value for growth in the range 1050-1120°C and far above the one required for the dissolution process of the γ' .

The two very distinct activation energies calculated at the same temperature (1140°C), one for the growth and the other for the dissolution process, show that the precipitate dissolution should be more favorable, since the energy required to activate the dissolution process is far less than that required for the growth. Also, the very low dissolution activation energy calculated using the size data obtained after agings at different temperatures for the same time period verifies the ease with which the dissolution process would progress as compared to the growth in the range 1140-1150°C. The positive slope shown in Figure 20 is an evidence for the dissolution, as well. Though this is the general trend, more dissolution is favored closer to the fine precipitate boundary, i.e., close to 1160°C. However, closer to the single-size coarse precipitate boundary, i.e., at 1140°C, some precipitate growth still occurs in the duplex-size zone by coalescence, even though the activation energy for the process has been vastly increased. As pointed out earlier, dissolution of coarse precipitates is a very fast process at temperatures above 1160°C requiring a time of about one minute or even less.

IV.3. Precipitate Coarsening Mechanisms

Precipitates generally coarsen by picking up solute atoms from the matrix, driven by the atomic diffusion process. However, coarsening can also occur by precipitate agglomeration and this is found to be one of the modes for growth of precipitates in the duplex-size microstructure of the alloy IN738LC. Also, two different precipitate coarsening features by the 'precipitate agglomeration mechanism' (PAM) were observed. Precipitate coarsening was by merging of smaller precipitates into larger ones in some cases, observed during agings after the solution treatment of 1120°C/2h/WQ or AAC, Fig. 21a. This process drives the morphological change from cuboidal to spheroidal or

ellipsoidal at low temperatures below $\sim 950^{\circ}\text{C}$. In the second case, the precipitate coalescence after the 1200 or 1250 $^{\circ}\text{C}/4\text{h}/\text{AAC}$ or WQ solution treatments and any aging treatment thereafter was via joining of nearly equisized precipitate particles. In this case, individual, adjacent precipitates seem to move as a whole and join with each other, as seen in Figs. 21b,c and 13h. Furthermore, as the precipitate coarsening advances, the agglomerated ones take on the cuboidal form in the temperature range of about 1050-1120 $^{\circ}\text{C}$. During the later stages of coarsening, the coarser precipitates formed retain their cuboidal shape while some smaller ones still join with them. This fact is clearly demonstrated in Fig. 21c.

However, the coarse cuboidal particles do not hold the cuboidal shape when their size becomes large enough and increases beyond a certain critical value. Around this time precipitate dissolution seems to start and the microstructure seems to change to the one containing the duplex-size precipitates. These aspects were already discussed in the previous two sections, III.2 and IV.2.

The features shown in Figs. 13h and 21 are clearly indicative of the fact that the precipitate coarsening is not controlled by conventional atomic diffusion process, wherein the smaller precipitates dissolve into the matrix, the solute atoms diffuse toward the larger ones, and their absorption by the latter leads to the precipitate coarsening due to the familiar Gibbs-Thompson effect. This process, Ostwald ripening, has been studied widely [23-27]. Although this process may be occurring, the precipitate coarsening here is via the agglomeration (consolidation) of adjacent precipitates. This process can still be considered as activated by inter-diffusion of atoms at the interface leading to its migration in the direction of possible attractive force activating the migration of the precipitate as a

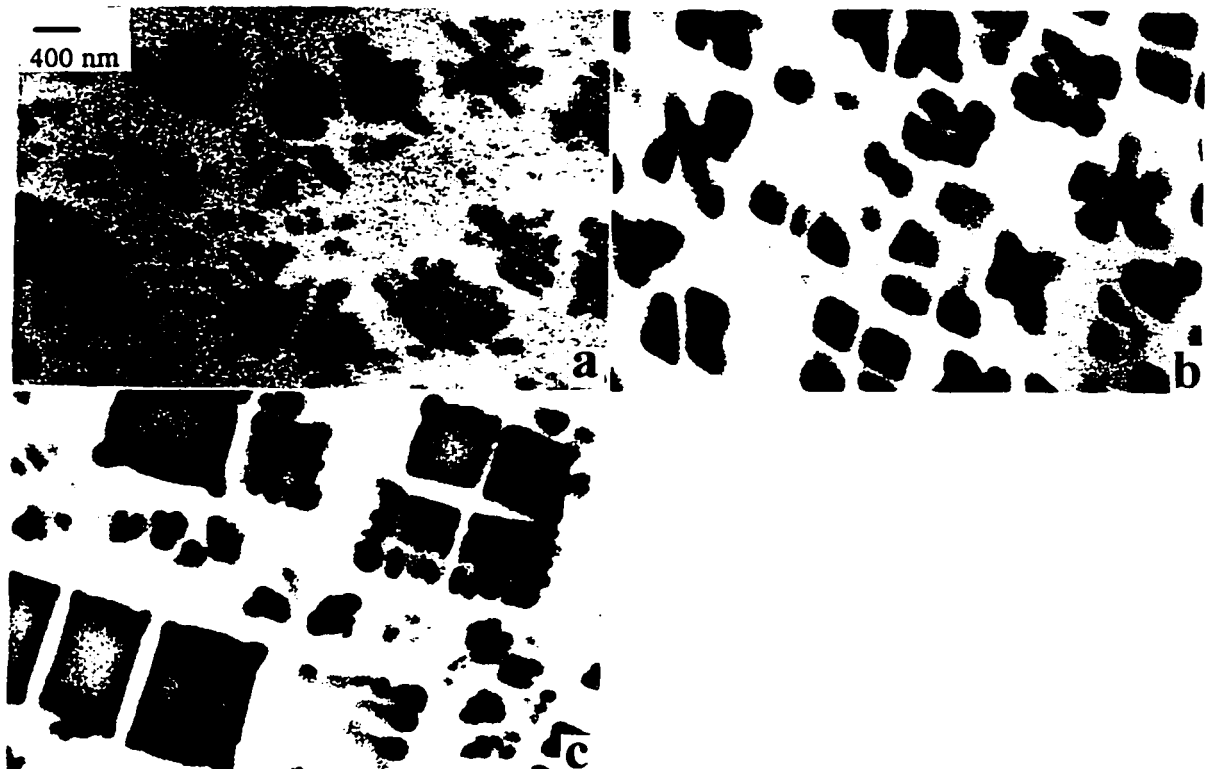


Figure 21. Micrographs showing the precipitate agglomeration modes.
(Magnification: 15kX)

a) in the duplex-size precipitate microstructure.

(1120°C / 2h / AAC + 750°C / 24h / FC)

b) agglomeration of adjacent precipitates in single-size precipitate microstructure.

(1250°C / 4h / AAC + 1200°C / 24h / FC)

c) micrograph showing the agglomeration of smaller precipitates (as in b) and later their coalescence into the bigger ones; also, possible coalescence of the adjacent four coarse precipitates (right top) and of three coarse ones (bottom left) along $\langle 100 \rangle$ direction is noticeable.

whole in the matrix medium. The precipitate coalescence takes place at a nearly constant volume fraction in the temperature range 650–1130°C in the superalloy IN738LC.

The first hypothesis on the precipitate movement in the matrix as a whole for agglomeration purposes was made by R. D. Doherty in 1982 [20]. Doherty indicated that the closely spaced precipitates could move toward each other and join by the removal of elastically strained matrix. Later, P. W. Voorhees and W. C. Johnson [21] did the first theoretical analysis (1988) of the particle migration in the matrix driven by the elastic stresses. They basically derived the formulae for growth rate and migration velocity of the mass center of precipitates, considering the elastic energies. Other authors also have considered the coalescence process by taking into account the lattice misfit, the applied stress, and the elastic properties of the constituent phases in the system [23,28-47]. General finding is that the sign of the misfit and the applied stress, the ratio of the elastic properties of the precipitate and the matrix phase, and the interfacial energy might significantly affect the precipitate evolution. Also, some of the results indicate an inverse coarsening [28-30], where smaller precipitates may grow at the expense of the larger ones due to the elastic interactions between the precipitates. This finding is just the opposite of the growth by Ostwald ripening.

The particle motion can be conceived to be due to the pull out of the face of the particles in the direction of postulated attractive force and corresponding caving-in at the opposite tail end of the particle. The advancing front can be projected to be pulled-out by activating the diffusion of the solute atoms from the precipitates into the adjoining matrix planes at the interface. The matrix layers in contact with the interface are then projected to slowly convert to precipitate layers. Simultaneously, diffusion of the solvent atoms

from the matrix layers into the precipitate layers at the interface occurring at the opposite tail end would convert the precipitate layers into the matrix. This mechanism could possibly be aided by the vacancy and/or dislocation concentration at the interface.

Another equally possible mechanism for particle motion is that a slight Poisson's contraction of the precipitates at the surfaces perpendicular to the moving front allows diffusion of the solvent atoms into these contracted surfaces. This would enable the removal of the squeezed-in matrix between the moving (joining) particles and its readjustment at the faces and the tail end of the moving precipitates. This scheme could also explain Doherty's original suggestion [20]. Concurrently, the deformed precipitates should readjust their shape to cuboidal form, requiring the solute redistribution in the distorted precipitates during and after the consolidation.

It can be deduced from Fig. 21c that the coarse cuboidal precipitates are generally aligned along two mutually perpendicular $\langle 100 \rangle$ directions and will coalesce subsequently along these directions, given more time. Figure 13h indicates the coalescence of two nearby precipitates of ellipsoidal shape along such a direction, whereas Fig. 21b illustrates the coalescence of generally four adjacent equisized particles. The directional alignment and coalescence of the precipitates along the elastically soft directions, $\langle 100 \rangle$, has already been reported [28-44]. This directional alignment is attributed to the tendency for the minimization of configurational strain energy (position dependent), which in turn reduces the total free energy of the system.

A step-by-step approach was followed to calculate the activation energy for the coalescence of the precipitates. In the first attempt, the diffusion-controlled growth mechanism was assumed and the conventional method for the calculation of the activation

energy (slope of $\log(d)$ vs. $1/T$ plot) was employed. The coarsening investigated here is not by the conventional atomic-diffusion-controlled mechanism. Nevertheless, Equation (2), governing the diffusion-controlled growth process was still used in the calculations as a first approximation. In later attempts, these calculations can be further improved. The ultimate aim is to better understand and define the nature of the energy required to coalesce the precipitates. The absence of any such study in the literature, to the author's knowledge, makes this analysis significant, although some attempts have been made earlier to formulate the force acting on or between the precipitates during directional alignment [34,40,41].

Figure 22 shows the plot of $\log(d)$ vs. $1/T$. This plot is a partial reproduction of Fig. 18. In this plot, the 24h precipitate size data in the WQ condition, given in Table 3 for the temperature range 850–1120°C is used with an analogous additional size obtained after aging at 1140°C for 24h in the duplex-size zone and water quenching, included in Table 4. The size of the coarse particles obtained after aging for 24 hours at 1140°C is lower than the corresponding one obtained after an analogous aging at 1120°C for 24 hours. Assuming linear variation of $\log(d)$ vs. $1/T$ in different temperature ranges, the activation energy for the γ' precipitate growth, Q , was calculated in first attempts to be 191 kJ/mol in the range of 850-1050°C and 350 kJ/mol in the range of 1050-1120°C for the WQ condition, taking $d_0=0$ and $n=3$, see section IV.1. In the calculation of these activation energy values, the slopes of the two nearly straight-line segments in the plot, one in the range 850-1050°C and the other in the 1050-1120°C range, were employed.

For a further, more precise analysis of the activation energy, the plot of $\log(d)$ vs. $1/T$, given in Fig. 22, was segmented into three parts (850-950°C, 950-1050°C, and 1050-

1120°C), and three different activation energies were obtained from the slopes of these segments. An additional activation energy value for the growth of analogous coarse precipitates in the duplex-size precipitate microstructure was calculated from the size data given in Table 4 for the aging treatment at 1140°C. In order to calculate this additional activation energy value at 1140°C, the K_0 value in the growth equation needs to be known in advance. After calculating the activation energy in the range 1050-1120°C and inserting this activation energy value back in Equation (2), the value for K_0 used was obtained. Use of the K_0 value calculated from the data in the range 1050-1120°C for the activation energy calculation at 1140°C is a reasonable approximation, since 1140°C is in the vicinity of this temperature range. It is obvious from the results that the activation energy increases with increasing temperature. This increase might be associated with the morphology change of precipitates from nearly spheroidal to cuboidal in the different temperature ranges from low to high. Plot of the four calculated activation energies mentioned above for precipitate growth vs. average temperature in the various temperature ranges is shown in Fig. 23.

A more careful observation indicates the possibility that the plot of the data of $\log(d)$ vs. $1/T$, given in Fig. 22, has a steadily varying curvilinear trend. Similar curvilinear trend is also observed in Fig.23 for Q varying with T . Hence, in further attempts to refine the activation energy calculations, a best curve fit was applied to the data points in these plots. These curve fits are shown in the corresponding figures, as well.

Using the data from the curve fit in Fig. 22, continuously varying Q values with T have been calculated for the range 850–1120°C. Together with the data for Q

corresponding to 1140°C, the above data can further be fitted with a curve (shown in Fig. 23) of a polynomial equation, written as follows:

$$Q(T) = (2.3356e-8)T^4 - (9.313e-5)T^3 + (0.1382)T^2 - (90.398)T + 22175 \quad (6)$$

Traditionally, the activation energy, Q , which is the energy needed to initiate a process, is given for a temperature range, and it comes in the Arrhenius equation as a constant. Here a polynomial dependency of Q on T is obtained, similar to the dependency of specific heat on temperature.

The continuously increasing activation energy for precipitate growth with increasing temperature is an interesting finding. It is also worth noting that the activation energy obtained for the growth of coarse precipitates at 1140°C (1413°K) in the duplex-size precipitate microstructure region also fits in very well with the curve fit for Q vs. T obtained, Fig. 23. Through extrapolation of the curve, a further increase in activation energy at still higher temperatures (1150-1225°C) is easily predictable. For instance, an activation energy value of 817 kJ/mol for the precipitate growth at 1160°C was calculated using Equation (6) given above. The same equation yields a value of 690 kJ/mol at 1140°C (experimentally determined value is 685 kJ/mol). Such a large increase in activation energy for growth at 1160°C and above might explain why the fine-size precipitates either remain stable and do not grow to any noticeably larger size even after several days of aging treatment or do not form at all activating dissolution tendencies of precipitates in the high temperature range 1160-1225°C, but form later during quenching, as stated earlier in section III.2.

The next attempt was to correlate the activation energy to the precipitate size and the inter-precipitate spacing. Figure 24 relates d_{cf} to T . (d_{cf} values were obtained from

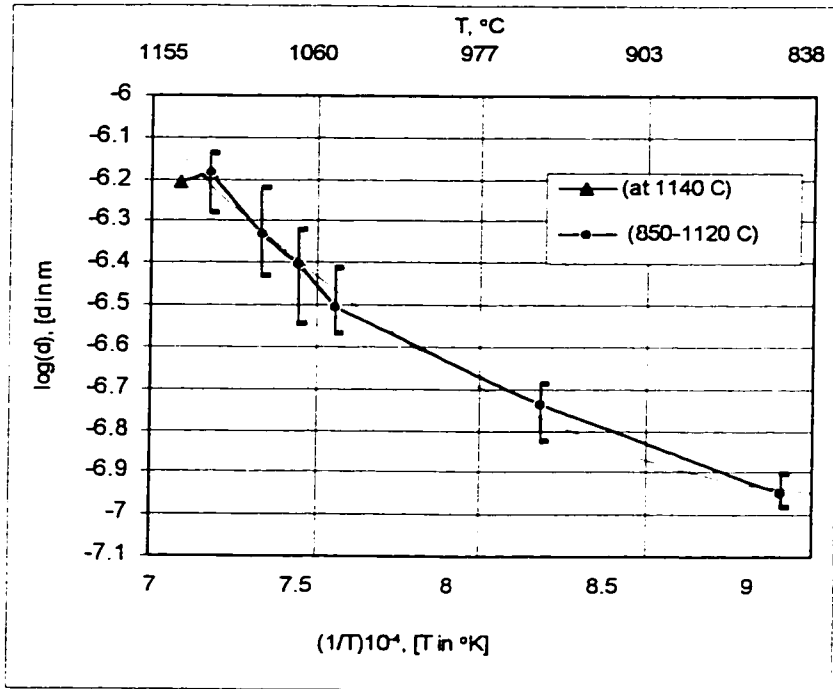


Figure 22. Plot of $\log(d)$ vs. $1/T$ of γ' size derived from data given in Table 3 and Table 4 for WQ condition (Partially reproduced from Fig. 18).

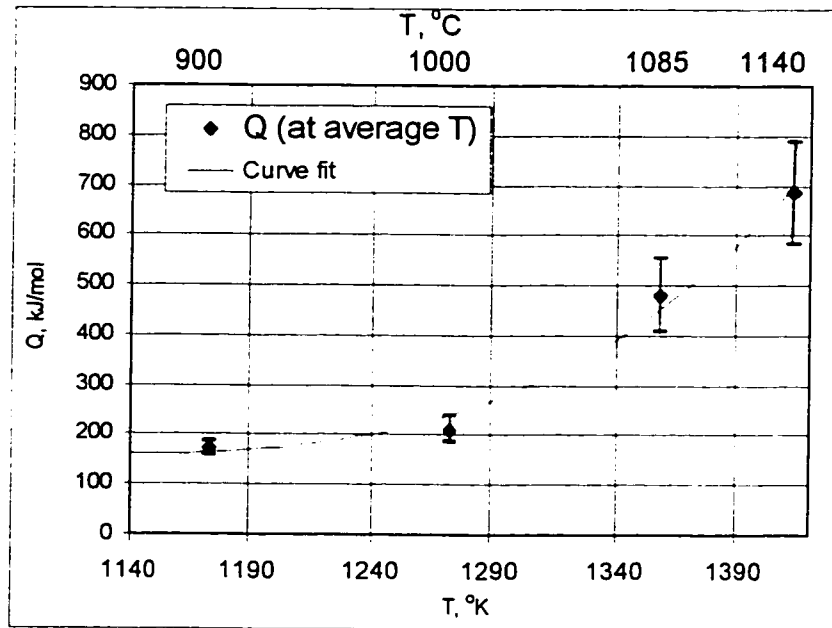


Figure 23. Plot of Q vs. T ; the curve fit is from the best fit curve of Fig. 22 including the data point corresponding to 1140°C

the curve fit given in Fig. 22). It is seen in Fig. 24 that the size of the precipitates varies as a polynomial function of T, as well. This function is determined in the form given as follows:

$$d_{cf}(T) = (3.30779e-5)T^3 - (0.116511)T^2 + (137.333)T - 54021.6 \quad (7)$$

To set out a relationship between the inter-precipitate spacing and temperature, the average spacing between the neighboring precipitates was measured from the micrographs in Fig. 11 obtained at 15000X magnification. Also, an attempt was made to calculate the spacing between the precipitates. For the calculation of this spacing, the sketch in Fig. 25 was used. In this figure the precipitates are assumed to be of similar size, unimodal-cuboidal in shape, and distributed evenly in the matrix. Also, the vertical and horizontal spacings between the precipitates are assumed to be equal. These conditions are not realized in the micrographs of the alloy; yet the microstructures can be crudely approximated to these conditions for analysis. The area shown within the dashed lines represents the unit cell out of which the area fraction and the spacing could be calculated. To calculate the inter-precipitate spacing, the following formula given in Ref. [102] (modified for the case under consideration) was employed:

$$s = \left(\sqrt{1 / A_f} - 1 \right) d \quad (8)$$

where s is the spacing between adjacent particles, A_f the area fraction, and d the precipitate size. The measured (s_m) and calculated (s_c) values of inter-precipitate spacing for the microstructures in Fig. 11 are plotted against temperature at which the given microstructure was obtained, Fig. 26. The inter-precipitate values (s_{cf}), calculated using

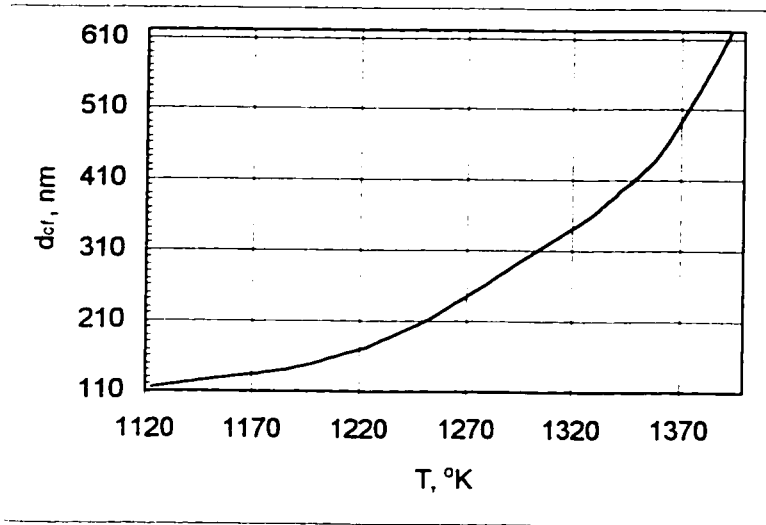


Figure 24. The plot of d_{cr} vs. T

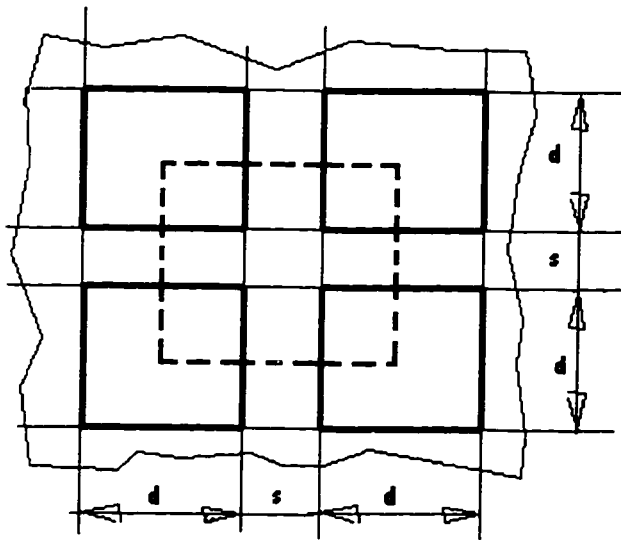


Figure 25. Evenly distributed cuboidal precipitates in the matrix. The area encapsulated with dashed lines shows the unit cell used to calculate the spacing (s) between the precipitates.

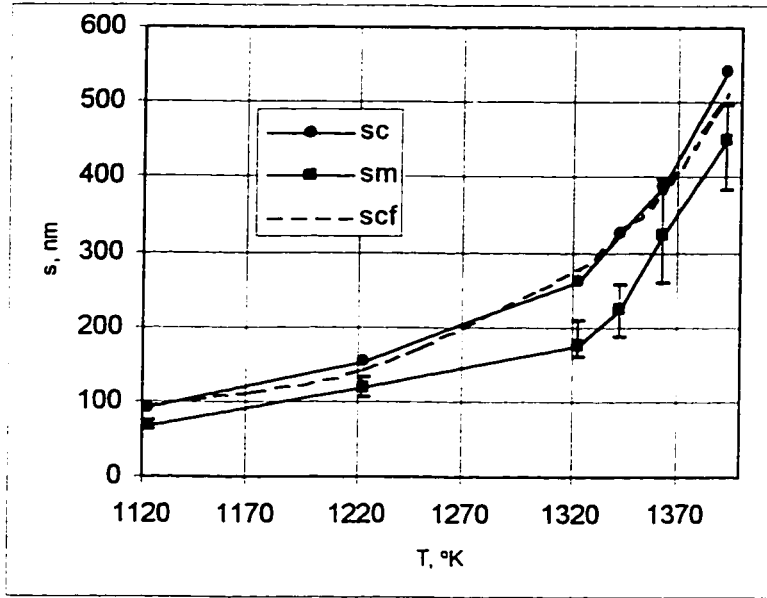


Figure 26. Plot of s vs. T

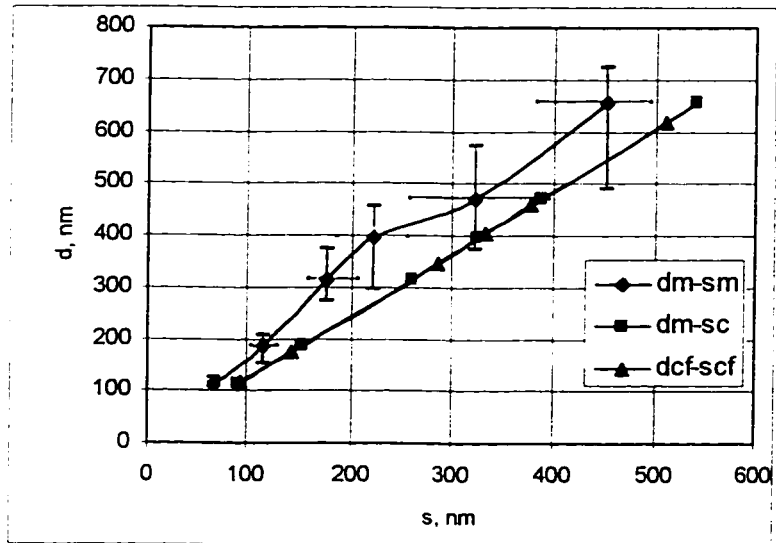


Figure 27. Plot of d vs. s

the d_{cr} in place of d in Eq. (7), are also shown in Fig. 26. Note that the calculated spacing values are about 20-40% larger than the average measured ones due to the non-uniformity in the spacings. Nevertheless, it can be concluded that as the precipitate size increases, the average distance between the precipitates also increases, if the volume fraction of the precipitates would approximately remain the same, as shown in Figure 27. In this figure, a general linear relationship is observed between the precipitate size and the spacing values, as dictated by Eq. (8), although a couple of data points in the d_m - s_m data plot show slight deviation from linearity. Nevertheless, proportional dependence of s with d can be approximated for experimental values, which indicate that the interparticle spacing increases with increasing size of the precipitates.

Observation of the micrographs shown in Fig. 11 and the features of Figs. 24 and 26 yield a hint for better understanding the unusual need for the increasing activation energy for the precipitate growth with increasing temperature. Analysis of Figs. 24 and 26 show that both the size and spacing between the precipitates increase with an increase in temperature, since the growth takes place at a nearly constant volume fraction of the precipitates, as mentioned earlier. Thus, the spacing between the precipitates is larger in the microstructure obtained after 1120°C/24h aging than in the ones obtained at lower temperatures for the same time period. This means that the increased size of the precipitates as well as the increased spacing between the adjacent ones necessitate more energy to coalesce them for growth. The increasing activation energy with increasing precipitate size and inter-particle spacing is illustrated in Fig. 28. The Q_{cr} values are the activation energy values calculated using Eq. (6) at different temperatures, which yielded the corresponding precipitate size and inter-particle spacing.

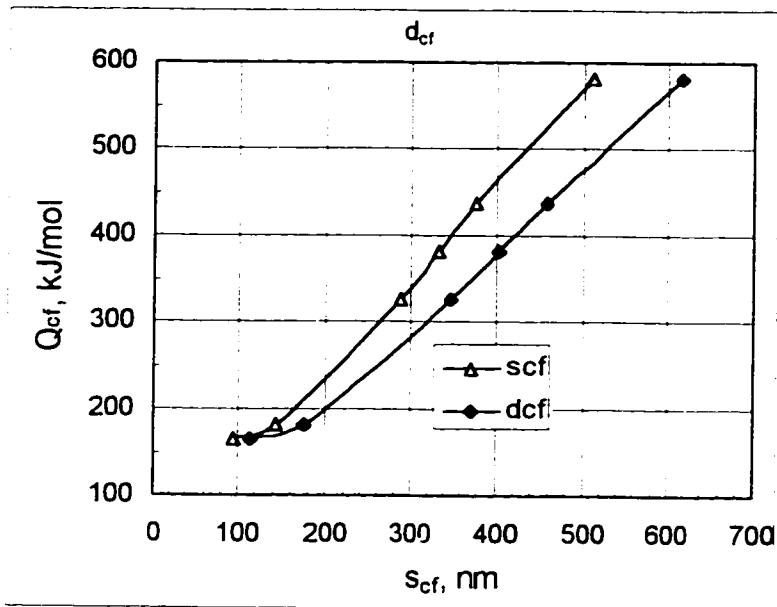


Figure 28. Plot of Q_{cf} vs. d_{cf} and s_{cf}

IV.3.1. The “Precipitate Agglomeration Model (PAM)”

The requirement for more energy for the coalescence process could be better understood when a clear distinction between the processes for the growth - one via disintegration or dissolution and atomic diffusion and the other by coalescence (i.e., by the movement of particles as a whole) - is made. In the latter, since the whole particle needs to move, it could be deduced that larger the size and more the distance to be moved, the more energy it would require. After coalescence, given time and sufficient energy, the consolidated precipitates could acquire uniform shape as appropriate, as seen in Fig. 11.

Based on the observations made above, a simple ‘Precipitate Agglomeration Model (PAM)’ can be proposed. It is postulated that the consolidation of adjacent particles by particle motion is due to an attractive force F_A exerted by the particles on one another. This attractive force is felt to be developed by the need to reduce the overall

surface interfacial energy of the particles as well as the elastic strain energy of the matrix at the given temperature, which would be determined by the total surface area of the particle. The surface area of the particle is a function of the size 'd' of the particle and should be proportional to d^2 . Hence, one can write:

$$F_A = f(d^2), \text{ where 'd' is a function of temperature} \quad (9).$$

If the particles are of similar size, then each particle would exert similar attractive force on each other and would tend to line up along a low energy direction, i.e., in a direction along which the consolidation energy would be the minimum. This would be the case especially if the consolidation energy were vastly anisotropic. Such seems to be the case in IN738LC, wherein the particles align along the $\langle 100 \rangle$ directions during annealing.

Dragged by the attractive force F_A , the particles are drawn to each other and coalesce. Hence, the agglomeration energy can be postulated to be a function of the product of the attractive force and the inter-particle distance 's'.

$$Q(d) \propto (F_A) \cdot s \propto f(d^2) \cdot f(d) \propto f(d^3) \quad (10)$$

since the inter-precipitate spacing is linearly proportional to the precipitate size, as indicated in Eq. (8). It is obvious that the proportionality in Eq. (10) may take the form:

$$Q(d) = C \cdot d^3 \quad (11)$$

where C is a constant, since the surface area is some linear function of d^2 and the inter-particle spacing also is a linear function of d. Thus, a linear function of Q with respect to d^3 can be proposed if no other factor is playing a role. However, if other factors, such as the influence of the matrix, etc., do play a role, then the variation of Q with respect to d need not be a linear function and can be written as:

$$Q(d) = f(C \cdot d^3) \quad (12)$$

Q_{cf} values obtained for the d_{cf} values of Fig. 22, plotted in Fig. 28, are again replotted against d_{cf}^3 . This plot is shown in Fig. 29. The function governing the curve shown in this plot is determined to be a polynomial given below:

$$Q = (4.96634e-23)(d^3)^3 - (2.57128e-14)(d^3)^2 + (5.11797e-6)(d^3) + 155 \quad (13)$$

This function represents an increasing dependency of Q to d^3 (i.e., to volume and hence to mass of each particle) and represents the variation of Q with the coarsening of the particles. Thus, it can be inferred that the agglomeration or consolidation energy is dependent on a function of the volume or the mass of the consolidating particles. Eq. (13) is a function coming out of the experimental data derived in this work. Further definition and refinement of the agglomeration energy is possible.

The nearly linear increase of precipitate size with time beyond 24h at 1140°C, shown in Fig. 19, can be utilized in a different type of analysis. In this time regime, precipitate coarsening seems to be controlled mainly by the precipitate agglomeration mechanism proposed and, as such, the data should be amenable to yield the consolidation energy. Further attempts can be oriented in this direction.

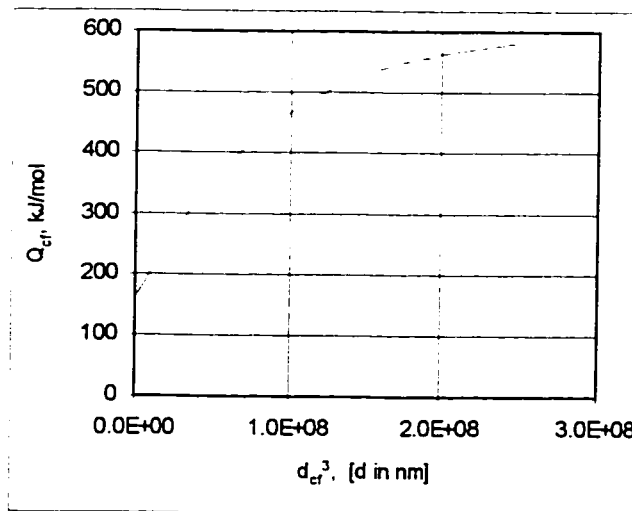


Figure 29. Plot of Q_{cf} vs d_{cf}^3

The increased activation energy at high temperatures around 1050-1160°C could probably signal to different precipitate evolution mechanisms, as well. It might be attributed to the formation of cuboidal precipitates and the need to grow them in cuboidal shape. It is reported that coarsening slows down at high magnitude of the misfit, since the elastic strains are proportional to the square of the misfit [37]. This means that precipitates with larger sizes, having higher misfit and elastic strains, would not favor the growth, and more energy supply would be required to advance any further coarsening. Moreover, the formation of the duplex-size precipitate microstructure at and above 1120°C and the single-size fine precipitate microstructure above 1160°C could necessitate a mechanism change to evolve and stabilize the fine precipitates at the highest possible temperatures in the precipitate forming temperature range. Alternatively, dissolution of precipitates and formation of single-phase solid solution should be favored. This could be a reason for the prohibitively high activation energy for growth at the highest possible temperature range 1160-1225°C. Whether the stability of the precipitates itself is possible under such a prevalence of high activation energy for growth is to be questioned. It is possible that the need of very high activation energy for growth triggers the breakdown of precipitates and favors the easy dissolution into the matrix at temperatures close to the single-phase solid solution formation temperature.

Utilization of atomic-diffusion-based equation, Eq. (2), to analyze particle coarsening appears to yield a continuously varying Q with temperature, unlike the constant Q assumed in the normal growth model. With the restriction that the activation energy Q for the precipitate coarsening process be a continuous variable of T , the diffusion-controlled model can still be used. PAM proposes that the consolidation energy

is also a function of d^3 . It may be possible in further attempts to define the attractive force F_A in terms of interfacial surface energy and elastic property differences between the matrix phase and the precipitates and to devise a better system of equations based on the premises of precipitate agglomeration model proposed here in this section. This and the directional nature of alignment of cuboidal particles and their subsequent consolidation along these directions of alignment, implying anisotropic nature of the consolidation energy, should verily be the topics for further study as PAM matures.

CHAPTER V. RESULTS AND DISCUSSIONS: PREFERRED ORIENTATIONS IN THE SUPERALLOY IN738LC

V.1. Results

Preferred orientations in the heat treated specimens could readily be detected when X-ray diffraction (XRD) was undertaken for structure analysis of the precipitates. The results of the XRD study pertaining to the preferred orientation and lattice parameter determination are given in Table 5. In this table, XRD data extracted from five different batches of specimens are presented. Taking of patterns was repeated at different times for specimens in three of the batches in order to verify the reproducibility. The lattice parameters of the FCC precipitate and matrix solid solution phases were calculated from the line positions in the patterns. These two phases were found to have nearly close lattice parameters, and very little difference was obtained. In several instances, where only one single diffraction line was obtained, lack of splitting or broadening of diffraction line indicated that the precipitate and the matrix phases possibly have nearly identical lattice parameters.

The first batch of specimens studied includes the single-phase supersaturated solid solution matrix (SSS), fine-size precipitate microstructure (F), Fig. 7, coarse-size precipitate microstructure (C), Fig. 9f1, and the duplex-size precipitate microstructure (D), Fig. 13f, containing very fine and medium size precipitates. All of these specimens had been cut parallel to the radial plane of the as-received cylindrical rod. The data obtained for specimens of this batch represents pretty much the basic results. A very strong $\{131\}$ preferred orientation was observed for the SSS. The fine precipitate microstructure showed a strong $\{220\}$ preferred orientation. Unimodal-cuboidal coarse precipitate microstructure was characterized by the $\{200\}$ preferred orientation. Two

preferred orientations were observed in the duplex-size microstructure, $\{200\}$ and $\{111\}$, the former for the precipitate and the latter for the matrix phase, respectively. An important deduction that could be made from the specimens of this batch is that the $L1_2$ ordering seems to be more noticeable in the coarse size precipitate microstructure, i.e., it gets pronounced with the coarsening of the precipitates. Repetition of XRD of these specimens yielded essentially similar results in all cases. However, an additional $\{111\}$ diffraction line was obtained along with the $\{131\}$ for the SSS, Fig. 31a, and likewise, the $\{131\}$ line was present along with $\{111\}$ in the pattern for the duplex microstructure, corresponding to those of the matrix phase. Fig. 30 (b, c, e, f) shows the diffraction patterns of the above described microstructures with the given POs.

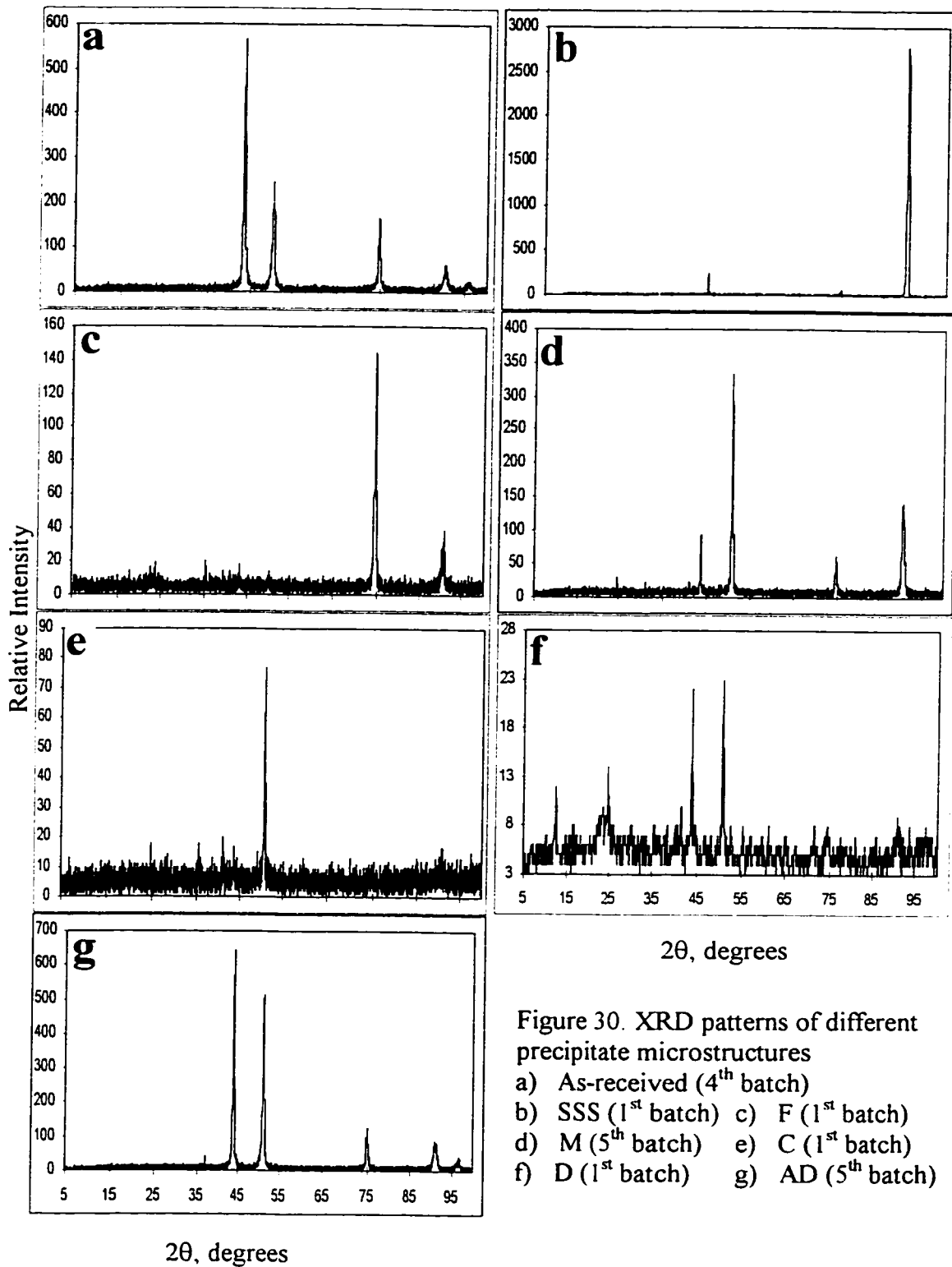
In the second batch of specimens, the as-received material without any further heat treatment was also included in addition to specimens similar to the ones in the first batch. The as-received material in this batch showed a very weak indication of $\{131\}$ preferred orientation, but basically it had random orientation in the radial section, Fig. 30a. Also, a $\{131\}$ orientation for the matrix and a $\{200\}$ orientation for the precipitate phase could be observed in the axial cut section of the as-received material. The solution-treated material as well as the microstructure with the coarse precipitates in the second batch had essentially similar textures as the analogous specimens in the first batch. The fine size precipitate microstructure had essentially the $\{220\}$ PO for the precipitate phase as in the first batch; however, it also showed the $\{111\}$ preferred orientation for the matrix. The duplex-size microstructure showed only the $\{111\}$ orientation in this case. Repetitions of XRD gave different results in all cases except in the case of C and the as-

Table 5. Preferred orientations and lattice parameters of FCC phases in the aged IN738LC alloy specimens

Micro-structure	Cut Section	1 st Batch	Repeat 1 st Batch	2 nd Batch	Repeat 2 nd Batch	3 rd Batch	4 th Batch	5 th Batch (Thermal Expn. Spns.)	Repeat 5 th Batch
AR	Radial			Random (3.604)	Same as 2 nd		Random (3.588)		
	Axial			{131} _M , {200} _P (3.5908) _{M/P}	Same as 2 nd		Random (3.587)		
SSS	Radial	{131}, (3.588) _M	{131}, {111} (3.59) _M	{131} (3.5855)	{111} (3.5915)	No good XRD Pattern	{220}, {200}+mdm (3.59)	ppied., {200} (3.582)	ppied., {200}, {111} (3.582)
	Axial						{131}, {111} _M , some ppt. possible (3.5906) _P , (3.578) _M	ppied., {200}, {111} (3.587)	ppied., {200} (3.587)
F	Radial	{220} _{PM} (3.598-3.595) _P , (3.585) _M	{220} (3.5876) _P	{220} _P , {111} _M (3.5956)	{131}, {111} (3.594)	{220} _P , {131} _M (3.592) _P , (3.584) _M	Si{131} _{M/P} , {220} _P (3.588) _P , (3.582) _M	{200} _P , wk{220} _M (3.5966) _P , (3.586) _M	
	Axial						{200} _P , {111} (3.5896) _P	Si{111} (3.5856)	
M	Radial						Si{200} _P , {131} (3.584) _P	{200} _P , [wk{131}, {111}] _M (3.592) _P , (3.580) _M	
	Axial						{200} _P , {111} (3.582) _P	Random (3.596) _P	
C	Radial	{200} _{PM} (3.593) _P , L1 ₂ order	{200} _P (3.595) _P	{200} (3.5935) weak L1 ₂ order	{200} (3.593)		{200}, {220} _P (3.5898) _P , (3.5838) _M	Si{200} (3.590) _P	
	Axial						{200} _P (3.5892) _P	Random (3.592) _P	
D	Radial	{200} _P , {111} _M (3.594) _P , (3.583) _M , L1 ₂ -D order	{200} _P , {131} _M → {111} _M (3.586) _M , (3.574) _M	{111} (3.584)	{131} _{PM} (3.584) _P , (3.577) _M		si{200} _P , {111} _M (3.586) _{PM}		
	Axial						{200}, {220} _P , {131}, {111} _M (3.591) _{PM}		
AD	Radial					{200} _P , {131} _M (3.5896) _P , (3.5838) _M		Random (3.565), (3.579)	Random (3.577)
	Axial							Si{111}, v. wk{131} (3.592) _P , (3.582) _M	v.wk{111} (3.582), (3.589)

L1₂-D (double L1₂) structure was observed in one specimen with duplex microstructure.

Also, L1₂ structure was observed almost in all the specimens studied, but this is not noted for all of the microstructures in the table.



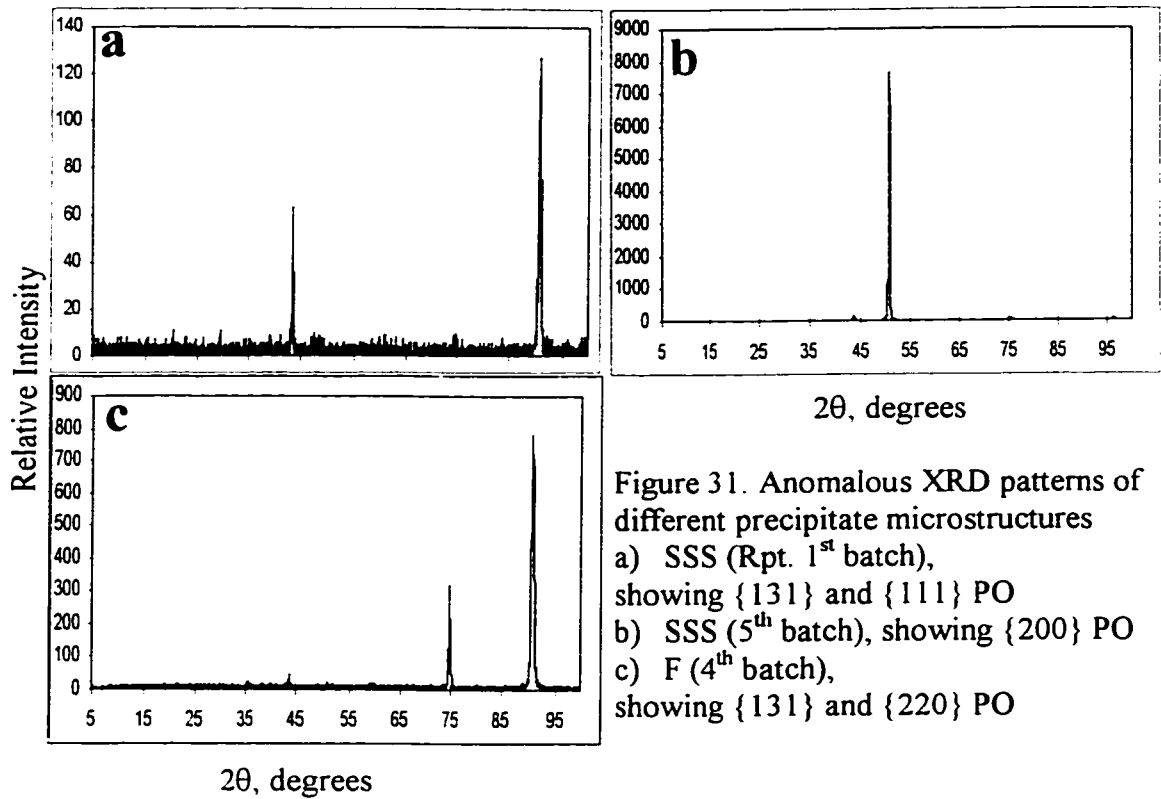


Figure 31. Anomalous XRD patterns of different precipitate microstructures
a) SSS (Rpt. 1st batch), showing $\{131\}$ and $\{111\}$ PO
b) SSS (5th batch), showing $\{200\}$ PO
c) F (4th batch), showing $\{131\}$ and $\{220\}$ PO

received material. A $\{111\}$ PO was observed in the repeat for SSS, which showed $\{131\}$ in the first try. Fine precipitate microstructure had $\{131\}$ orientation instead of $\{220\}$ obtained in the first XRD, along with the $\{111\}$ orientation. A $\{131\}$ orientation was observed with the duplex-size microstructure instead of the $\{111\}$.

The fine precipitate microstructure of the third batch showed the $\{220\}$ and $\{131\}$ preferred orientations for the precipitate and the matrix phases, respectively, Fig. 31c. The duplex-size precipitate microstructure obtained through aging at 1140°C was further aged at 950°C for 36 hours and analyzed along with the other specimens in the third batch. This annealed duplex (AD) microstructure showed a $\{200\}$ orientation for the precipitate and $\{131\}$ for the matrix phase in the third batch.

Specimens in the fourth batch were cut from the radial and axial planes for all of the microstructures from a new set of rods obtained for the second time. The as-received sample showed no preferred orientation in either section conforming to previous results. The results obtained from radial sections of other specimens were generally conforming to results obtained from the first three batches. However, the solution-treated microstructure had the expected $\{131\}$ PO in the axial section only along with $\{111\}$, but $\{220\}$ and $\{200\}$ preferred orientations were found in the samples cut parallel to the radial plane. The $\{131\}$ and $\{220\}$ orientations were seen for the fine microstructure in the radial section for the matrix and the precipitate phase, respectively, but in the axial section $\{200\}$ and $\{111\}$ preferred orientations were observed. The microstructure having medium size precipitates (M), Fig. 9e, analyzed for the first time, showed $\{200\}$ orientation in both sections for the precipitate phase, but had $\{111\}$ orientation in the radial section and $\{131\}$ orientation in the axial section for the matrix phase. The coarse size precipitate microstructure showed the expected $\{200\}$ preferred orientation in both sections. In addition, a $\{220\}$ orientation was observed in the radial section of this microstructure. The duplex microstructure showed the expected $\{200\}$ and $\{111\}$ orientations in both the cut sections for the precipitate and the matrix phase, respectively. It also showed $\{220\}$ orientation for the precipitate phase and the $\{131\}$ orientation for the matrix phase in the axial section.

X-ray study also was carried out on some of the specimens of IN738LC that had already been heat treated suitably and used in thermal expansion tests, discussed later in chapter VIII. The solution treated material (SSS) in this batch showed strong $\{200\}$ PO in both sections, Fig. 31b. The $\{111\}$ diffraction peak was still present. Fine precipitates

could be observed readily in the microstructure of these specimens after the thermal expansion test. Repeat of XRD yielded nearly similar result. Fine size microstructure showed {200} and {220} preferred orientations in the radial section, but had very strong {111} PO in the axial section. Microstructure M with medium size precipitates showed {200} PO for precipitate phase and {111} and {131} for the matrix phase in the radial section. This specimen exhibited random orientation in the axial section. Coarse precipitate microstructure showed the expected {200} PO in the radial, but had random orientation in the axial section. The annealed duplex microstructure (AD) as in the third batch showed random orientation in the radial section, but strong {111} and {131} orientations in the axial section. Repeat XRD yielded, likewise, random orientation in the radial section.

Results obtained with the $Ni_3Al(Ti, Nb)$ type intermetallic alloys are presented in Table 6. It is notable that alloys containing Ti showed generally very strong and single cube texture - the {200} preferred orientation.

Table 6. Preferred orientation (PO) data and lattice parameters of $L1_2$ phases in some Ni-aluminide-type alloys deduced from XRD patterns.

Alloy composition	Heat Treatment		Applied	
	1100°C/5	days/AC	750°C/14	days/AC
	PO	a, Å	PO	a, Å
1) Ni_3Al	{200} partial	3.569	{111} partial	3.565
2) $Ni_3Al_{0.5}Ti_{0.5}$	{200} 100%	3.5896	{200} 100%	3.592
3) $Ni_3Al_{0.5}Nb_{0.5}$ *	random	3.601	{111} slight	3.6055
4) $Ni_3Al_{0.5}Ti_{0.25}Nb_{0.25}$ **	{200} 100%	3.598	{200} 100%	3.598

* In addition to the $L1_2$ phase, another phase is present in very small amount.

**This alloy also has another phase along with the $L1_2$ phase. Lines of this phase are extremely weak and do not correspond to the second phase in alloy 3.

V.2. Discussion

Annealing textures are found to develop easily in hiped and aged IN738LC superalloy. Very strong single POs are generally found for most of the precipitated microstructures, except for the one containing duplex-size precipitates. The solid solution phase takes on the $\{131\}$ texture in the supersaturated solution-treated condition, but the texture seems to change to $\{111\}$ when this phase is annealed, see Fig. 31a. During the annealing process the matrix would relax any internal stress and precipitate the γ' phase, and the concentration of solute in the solid solution matrix would decrease. Either of these processes seems to trigger the changeover of texture from $\{131\}$ to $\{111\}$ and either one or both of these types of textures could be obtained in a given sample. However, the matrix phase is also found to take on a similar texture as the precipitate phase, abandoning the $\{131\}$ and/or the $\{111\}$ preferred orientations developed at the initial stages of annealing. This may have been facilitated by the weak nature of the matrix¹.

The precipitate phase seems to show a strong tendency to grow in cuboidal mode at temperatures above about 1000°C. Attendant to its nucleation and growth feature, the precipitate takes on the $\{220\}$ PO when it is fine and changes to the $\{200\}$ orientation with the coarsening of particles. This is evident not only in the coarse precipitate microstructure, but in the microstructure with the medium size precipitates as well. The interesting finding is that the matrix phase seems to enable the easy coarsening and cuboidal alignment of the particles by changing its own PO to that of the precipitate

¹ That the matrix is weak is proven in tensile tests carried out at 1200°C, see VI.2.

phase, as described earlier. Thus only one strong PO, either of the $\{220\}$ for the F or of the $\{200\}$ with the M and C microstructures, can be detected in these precipitated microstructures, indicating that both the precipitate and the matrix phases have similar orientations. It is also found that the precipitate phase and the matrix phase have nearly identical lattice parameters, since there is no detectable line broadening or shift found in the single diffraction peak obtained in either case, see Fig. 30 (c, e).

The duplex-size precipitate microstructure has the $\{200\}$ PO for the precipitates and the $\{111\}$ PO for the matrix. The orientation of the precipitates is thus found to be dictated by the coarsened medium size precipitates and not by the extremely fine ones. The matrix also does not conform to the orientation of the precipitates in the duplex microstructure and this may be either due to the formation of two differently sized precipitates or due to the start of the precipitate dissolution process and partial dissolution of precipitates that has been introduced.

The microstructure of the as-received sample can be considered to be a modification of the duplex-size precipitate microstructure (D) in which the fine precipitates have been coarsened by a low temperature second aging and/or furnace cooling. The as-received samples generally show random orientation, which indicates that with the coarsening of the precipitates in the duplex-size microstructure, a random orientation would result. Possibly, with the coarsening, large misfit strains get produced, which can be postulated to be accommodated or relaxed somewhat by the material abandoning the preferred orientations for both the precipitate and the matrix solid solution phase. That this occurs only in the case of duplex-size precipitated microstructure is an interesting finding. The coarsening in the duplex-size microstructure

occurs also by particle agglomeration, i.e., by the fine particles literally migrating and joining with the adjacent coarse particle, as already discussed in chapter IV.3. Possibly, when such coarsening is taking place by particle agglomeration, the PO characteristic is getting lost. The annealed condition of the duplex-size precipitate microstructure (AD) also indicates a tendency toward randomizing the orientations of both the precipitates and the matrix solid solution, see Table 5.

The thermal-expansion-tested SSS specimen indicates a {200} PO along with a slight prevalence of the {111} texture. The former is attributable to the precipitates that have been formed during the thermal expansion test, i.e., by the heating involved in the test. The matrix changes to the expected {111} PO, as already stated. The only anomaly is that the precipitate takes on the {200} texture that has been observed for the coarse precipitates in the other samples. The difference is attributable to the very slow controlled heating involved in the thermal expansion run. Obviously, such very slow controlled heating appears to be congenial for the formation of the true cube texture at low temperatures.

Data presented in Table 6 is indicative of the fact that Ni_3Al itself is amenable to texturing during annealing. This intermetallic phase seems to take on a weak {200} or {111} texture at high and low temperatures, respectively. It is noteworthy, however, that with the addition of Ti in solid solution, a complete and strong {200} texture is obtained, even in solid solutions that contain equal amounts of Nb as Ti. On the contrary, addition of Nb alone in solid solution does not seem to promote any specific PO, but rather random orientation of grains results.

The lattice parameter data, given in Table 5 in parenthesis, for the phases can be used to calculate the relative misfit between the matrix FCC phase and the FCC precipitate phase. The misfit calculated as $(\Delta a)/a$ is rather small and is in the range 0.17 to 0.36%. However, as stated earlier, when only one diffraction peak with no broadening is obtained, only one lattice parameter could be calculated and it has to be assumed that both the phases in question have nearly identical lattice parameters, which would mean that the misfit is nearly zero. This is not unusual and such results have been reported in the literature for the superalloys, as already mentioned in the earlier sections and given in Ref. [98].

**CHAPTER VI. RESULTS AND DISCUSSIONS:
HIGH TEMPERATURE TENSILE PROPERTIES OF
POLYCRYSTALLINE SUPERALLOY IN738LC**

VI.1. In the Range RT-850°C with Various Precipitate Microstructures

Different precipitate microstructures were developed first using the heat treatment schedules already introduced in the earlier chapters. Among the precipitate microstructures, four of them were tested for their tensile properties. These microstructures consisted of i) fine-size (F; ~70 nm size), ii) medium-size unimodal-cuboidal (M; ~ 450 nm size), iii) coarse-size unimodal-cuboidal (C; ~700 nm size), and iv) duplex-size (D; ~50 and ~450 nm sizes) precipitates. These precipitated microstructures are shown in Fig. 32. Single phase supersaturated matrix in the solution

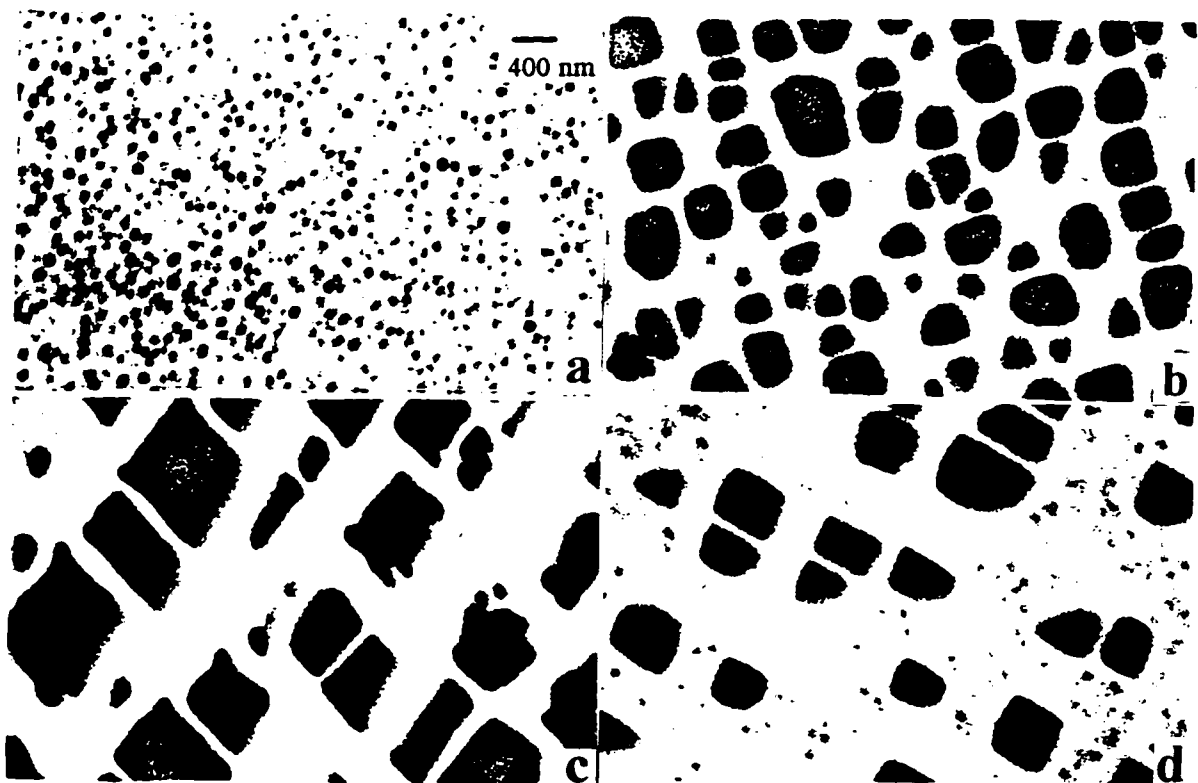


Figure 32. Various precipitate microstructures of IN738LC chosen for tensile testing and thermal expansion studies (Magnification: 15kX).
a) fine-size ppts. (F; ~70 nm) b) medium-size ppts. (M; ~450 nm)
c) coarse-size ppts. (C; ~700 nm) d) duplex-size ppts. (D; ~50 and 450 nm)

treated condition (SSS) was also included in the tests at room temperature to obtain data for the matrix.

VI.1.1. Results

The tensile test results obtained for different microstructures are compiled in Table 7 and shown in Figures 33-38. Tests were conducted on two analogous specimens for each case and the data given are the averaged results from the two tests. They are further described below. When calculating the strain hardening coefficient and strain rate sensitivity, the formulae given in Ref. [103] are employed.

(i) Single-phase Solid Solution matrix (SSS): This is the solution-treated and quenched material containing only the supersaturated solid solution with no precipitates. Tensile tests were conducted on this material at room temperature only, since during high temperature tests the material would form the precipitated microstructure and its properties would continuously change. The yield and tensile strengths as well as the elasticity modulus for this microstructure are higher with the higher applied strain rate (10^{-3} s^{-1}). The corresponding properties are shown among room temperature data in Figures 33-35. This microstructure also strain hardens more with the higher strain rate, Fig. 36. Also, a lower % elongation value was obtained with the lower strain rate ($5 \times 10^{-5} \text{ s}^{-1}$), Fig. 37. The material also showed the highest positive strain rate sensitivity, Fig. 38.

(ii) Fine-size precipitate microstructure (F): This microstructure consisted of unimodal, fine precipitates of size of about 70 nm, as can be seen in Fig. 32a. Specimens with such fine precipitates showed the highest yield strength among the tested microstructures from room temperature up to 750°C at both the strain rates applied. The 0.2% offset yield strength values for this microstructure are given in Figures 33 (a, b). At

the higher strain rate of 10^{-3} s^{-1} , the yield strength steadily decreased with increasing temperature up to 750°C , but at 850°C a sharp decrease in the yield strength was observed. At the lower strain rate of $5 \times 10^{-5} \text{ s}^{-1}$, the yield strength dropped from the room temperature value to a lower one at 650°C , and later showed an anomalous increase at 750°C . Beyond this temperature, however, the yield strength dropped drastically. The observed yield strength was slightly higher at the lower strain rate in the range room temperature to 750°C ; consequently, a slightly negative strain rate sensitivity was calculated in this range, Fig. 38. However, it became positive in the range $750\text{-}850^{\circ}\text{C}$ as for the other microstructures. Elasticity modulus of this microstructure followed a trend very similar to the yield strength at both strain rates (compare Figures 33 and 35). The tensile strength of this microstructure decreased only by a relatively small amount from room temperature to 650°C at the higher strain rate, but a sharp decrease was observed at and above 750°C , as seen in Fig. 34. Strain hardening was generally small, but got slightly increased at 750°C ; the values were nearly similar at room temperature and 650°C , and the lowest value (zero) was at 850°C after the tests with both the strain rates, Fig. 36. The elongation seems to drop continuously from 11% at room temperature to 4.7% at 850°C at the lower strain rate, whereas it increases from about 7% at RT to its maximum value of 16% at 650°C and drops back to about 5% thereafter at the higher strain rate.

(iii) Medium-size precipitate microstructure (M): This microstructure, shown in Fig. 32b, has unimodal cuboidal precipitates with the size of about 450 nm. Its yield strength decreased continuously up to 750°C . Also, a relatively sharp drop was observed in the range $750\text{-}850^{\circ}\text{C}$ with the lower strain rate. The tests with the higher strain rate

Table 7. Tensile Properties of IN738LC with various precipitate microstructures.

Micro-Structure	T, °C	σ_y , MPa [$\pm 3\%$]		E, GPa [$\pm 8\%$]		σ_u , MPa [$\pm 5\%$]		Strain hardening coefficient, n		% Elongation, δ [$\pm 12\%$]		Strain rate sensitivity, m	Energy-to-break, J	
		$\dot{\epsilon}=10^{-3}$ s ⁻¹	$\dot{\epsilon}=5 \times 10^{-5}$ s ⁻¹	$\dot{\epsilon}=10^{-3}$ s ⁻¹	$\dot{\epsilon}=5 \times 10^{-5}$ s ⁻¹	$\dot{\epsilon}=10^{-3}$ s ⁻¹	$\dot{\epsilon}=5 \times 10^{-5}$ s ⁻¹	$\dot{\epsilon}=10^{-3}$ s ⁻¹	$\dot{\epsilon}=5 \times 10^{-5}$ s ⁻¹	$\dot{\epsilon}=10^{-3}$ s ⁻¹	$\dot{\epsilon}=5 \times 10^{-5}$ s ⁻¹		$\dot{\epsilon}=10^{-3}$ s ⁻¹	$\dot{\epsilon}=5 \times 10^{-5}$ s ⁻¹
SSS	20	853.0	668.0	170.0	143.7	889.5	721.3	0.068	0.014	7.8	4.9	0.082	25	11
	20	851.8	859.0	176.6	164.0	915.9	964.9	0.092	0.102	7.0	11.2	-0.003	20	41
F (70 nm)	650	789.4	789.2	151.6	142.9	907.8	843.5	0.109	0.098	16.0	8.0	0.000	58	20
	750	779.3	802.6	141.0	143.8	797.7	820.6	0.137	0.110	5.7	6.7	-0.009	12	14
	850	684.4	551.6	124.1	131.0	684.4	552.5	0.000	0.000	4.7	4.7	0.072	9	6
M (450 nm)	1200	10	4	13	8	11	4.5			35	35	0.31		
	20	709.6	680.5	170.3	156.0	849.5	839.4	0.127	0.143	11.5	11.8	0.014	38	41
	650	589.3	608.2	147.6	131.8	846.2	883.4	0.224	0.221	16.5	19.6	-0.010	55	70
C (700 nm)	750	582.1	604.4	122.7	134.6	787.1	758.5	0.197	0.169	11.5	10.5	-0.013	33	28
	850	595.5	511.4	125.7	113.8	739.8	603.9	0.128	0.109	13.0	8.7	0.050	55	27
	20	712.0	700.7	163.4	157.6	862.8	920.5	0.142	0.174	15.5	20.4	0.005	59	82
D (50 and 450 nm)	650	599.7	583.0	142.7	123.5	899.3	920.8	0.261	0.268	24.5	26.4	0.009	90	99
	750	587.6	607.1	117.6	125.6	852.8	825.1	0.248	0.217	21.0*	11.8	-0.010	79	39
	850	604.6	479.2	126.4	94.6	698.4	590.4	0.028	0.077	18.5	15.1	0.077	68	48
D (50 and 450 nm)	20	858.6	834.4	167.6	161.4	1031	912.7	0.118	0.090	16.0	8.5	0.009	70	30
	650	768.4	739.7	139.2	134.6	875.0	818.1	0.101	0.112	12.9	12.1	0.012	48	38
	750	761.6	764.6	126.5	146.5	817.9	797.4	0.094	0.101	6.5	6.8	-0.001	20	15
850	786.9	633.5	132.2	124.4	786.9	654.2	0.000	0.000	5.3	5.1	0.072	12	9	

* The coarse-size precipitate microstructure tested at 750°C with the higher strain rate showed a $\pm 30\%$ deviation in percent elongation.

produced nearly similar results, but with a slight anomalous increase in the yield strength in the range 750-850°C. The tensile strength seemed to increase slightly up to 650°C at the lower strain rate, beyond which a continuous drop was observed with both strain rates. The elasticity modulus followed the same trend as the yield strength at both the strain rates, compare Fig. 33 with Fig. 35. Strain hardening increased by about 50% at 650°C from its room temperature value, above which it decreased again at both the strain rates. Strain rate sensitivity of 0.2% yield strength was more pronounced at 850°C, as for the other microstructures. Highest elongation (17-20%) was found at 650°C for both the strain rates, Fig. 37, with subsequent reduction in elongation with further increase in temperature, but there was an increase in elongation in the range 750-850°C with the higher strain rate.

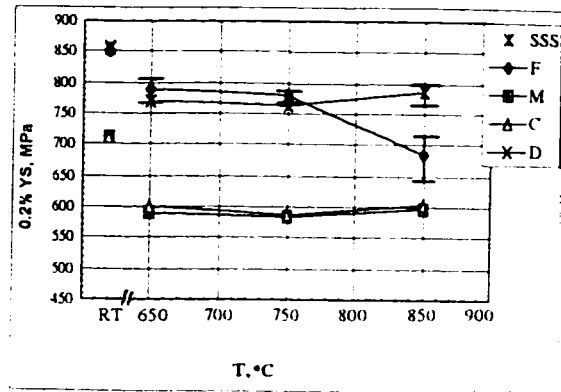
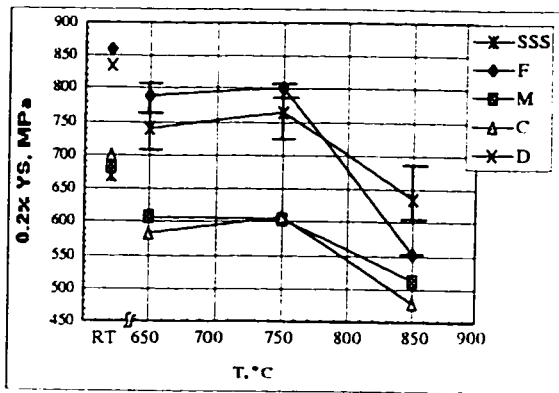
(iv) Coarse-size precipitate microstructure (C): This microstructure has unimodal cuboidal precipitates of size about 700 nm, Fig. 32c. This was the coarsest precipitate size that was experimented in this study. The yield strength of this microstructure exhibited similar behavior as the medium-size precipitate microstructure at both the strain rates applied. The anomalous strengthening peak was seen at 750°C with the lower strain rate, and it shifted to 850°C with the higher strain rate. The tensile strength increased very slightly at 650°C, and it decreased beyond this temperature with both the strain rates. The elasticity modulus behaved nearly in a similar way as the yield strength under both the strain rates. Maximum strain hardening and elongation (24-27%) were seen at 650°C with both the strain rates, Figs. 36 and 37. Whereas the former dropped considerably in the range 750-850°C, the elongation increased in the range 750-850°C after dropping considerably in the range 650-750°C with the lower strain rate. At the higher strain rate,

however, the drop in elongation was continuous, but only half as much, in the range 650-850°C. The magnitude of the strain rate sensitivity was the highest at 850°C as for all of the microstructures.

(v) Duplex-size precipitate microstructure (D): Two distinctly different precipitate sizes constituted this microstructure, one fine (~50 nm) and the other medium size (~450 nm). This microstructure is illustrated in Fig. 32d. The yield strength behavior of this microstructure was very similar to those of the microstructures M and C, though the value was higher. This microstructure had the highest tensile strength among all at RT after the higher strain rate and at 850°C for both the strain rates. The tensile strength decreased steadily with increasing temperature at both the strain rates. The elasticity modulus showed an anomalous increase and peaked at 750°C with the lower strain rate, but the peak was found to be shifted to 850°C with the higher strain rate. Strain hardening coefficient was generally small as for F; it seemed to rise slightly initially up to 650°C, but later dropped to zero at 850°C with the lower strain rate, Fig. 36a. A continuously decreasing value of strain hardening coefficient was seen with the higher strain rate from room temperature to 750°C, and there was a drastic drop in strain hardening to nearly zero value in the range 750-850°C, Fig. 36b. The strain rate sensitivity was the highest at 850°C as for the other microstructures. The % elongation seemed to have a similar trend as the strain hardening coefficient for this microstructure.

VI.1.2. Discussion

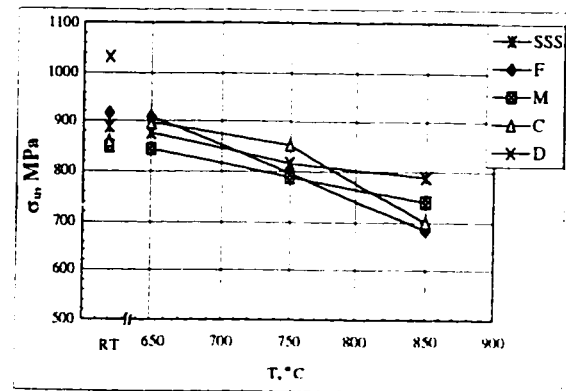
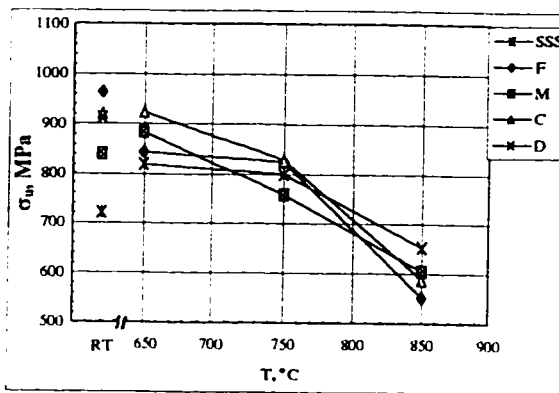
The variations of tensile mechanical properties with the microstructure, strain rate and test temperature are discussed below.



(a)

(b)

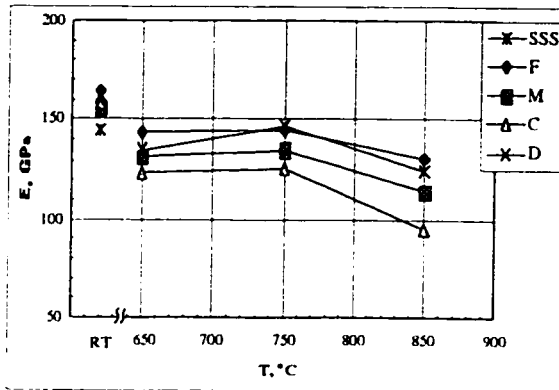
Figure 33. 0.2% offset Yield strength with
 a) low strain rate ($5 \times 10^{-5} \text{ s}^{-1}$) b) high strain rate (10^{-3} s^{-1}).



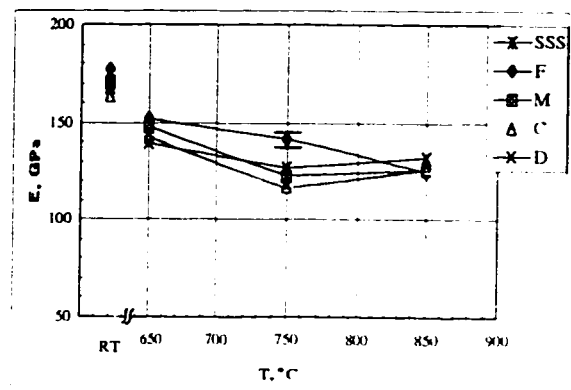
(a)

(b)

Figure 34. Tensile strength with
 a) low strain rate ($5 \times 10^{-5} \text{ s}^{-1}$) b) high strain rate (10^{-3} s^{-1}).



(a)

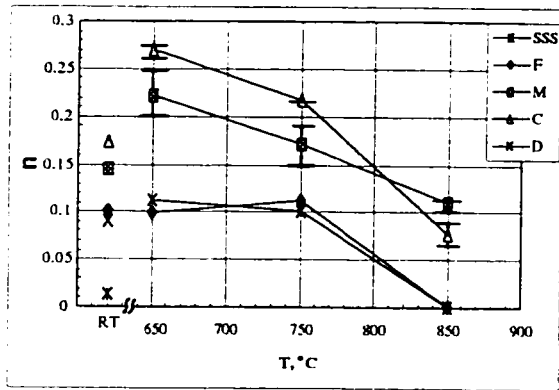


(b)

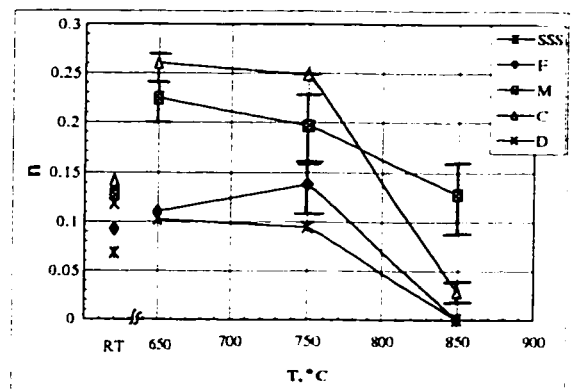
Figure 35. Elasticity Modulus with

a) low strain rate ($5 \times 10^{-5} \text{ s}^{-1}$)

b) high strain rate (10^{-3} s^{-1}).



(a)

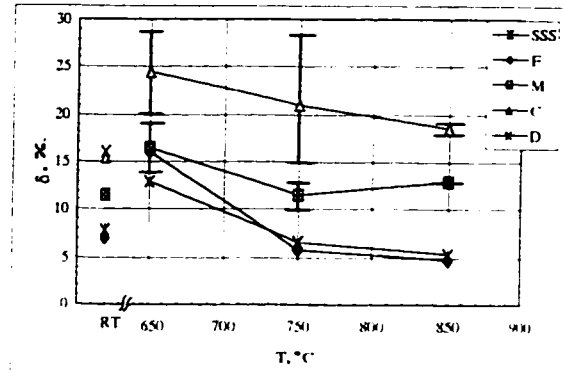
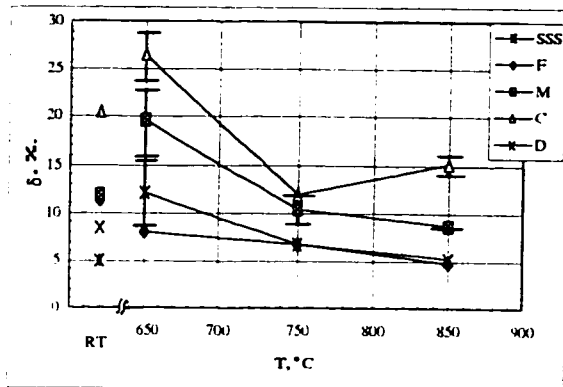


(b)

Figure 36. Strain Hardening Coefficient with

a) low strain rate ($5 \times 10^{-5} \text{ s}^{-1}$)

b) high strain rate (10^{-3} s^{-1}).



(a)

(b)

Figure 37. % Elongation, δ with
a) low strain rate ($5 \times 10^{-5} \text{ s}^{-1}$)

b) high strain rate (10^{-3} s^{-1}).

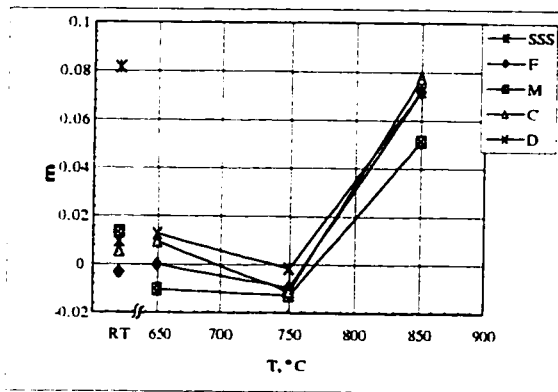


Figure 38. Strain rate sensitivity of yield strength for the various microstructures.

Yield Behavior: The yield behavior of the microstructures tested could be studied in two groups, the behavior of F and D in one and of M and C in the other. The microstructures F and D have higher yield strength in the entire test temperature range, see Fig. 33. Since they both have fine size precipitates and F shows slightly higher yield strength than D, this could be related to the precipitate size effect. Duplex-size (D) microstructure, having similar medium size cuboidal precipitates as M and fine size precipitates as F, might be expected to have somewhat an intermediate behavior. However, the existence of fine precipitates as in F seems to force D to behave more like F and the strength is lowered only slightly by the presence of the medium size precipitates. This clearly illustrates the effectiveness of the fine precipitates in the microstructure for increasing the flow stress. Also, this behavior is exhibited at both strain rates. Since the strengthening in precipitated microstructures is generally attributed to the blocking of moving dislocations by the precipitate particles and finer the precipitates and smaller their interparticle spacing, higher is the strengthening, the result obtained in this study is expected. The dominance of the fine precipitates in the duplex-size microstructure is also noteworthy. Also, the yield strength data reported in this paper is in good agreement with the mechanics model enunciated in Ref. [104] by Voyiadjis and Huang which stipulates that the yield strength is inversely proportional to the interparticle spacing.

An anomalous increase in yield strength is observed at high temperatures with both the strain rates and this is a commonly observed behavior in the γ' -strengthened superalloys [6,8,70-73]. This anomalous increase in yield strength has been well studied in several intermetallic alloys such as Ni_3Al and Ni_3Ga [63-68] as well. The strengthening of the intermetallic Ni_3Al at high temperatures is attributed to the cross slipping of

dislocations from the octahedral $\{111\}$ planes of the FCC superlattice to the $\{100\}$ cubic planes and their subsequent locking [69]. Since Ni_3Al is the strengthening precipitate phase in the superalloy IN738LC, the anomalous increase in yield strength in this superalloy might be attributed to a similar strengthening mechanism by Ni_3Al , as well. Anomalous strengthening also may depend on whether the dislocations moving in the solid solution matrix cut through or loop around the strengthening precipitate particles, and the dislocation interaction at the γ' - matrix interface needs to be defined also for a more precise explanation.

Observation of Figures 33a and 33b shows that with the higher strain rate anomalous strengthening occurs at the higher temperature of 850°C than for the lower strain rate for all the microstructures except for F. A similar result was reported in Refs. [6,8,71]. It is also seen that the magnitude of the peak strength at 850°C is higher (about 30%) with the higher strain rate than the analogous strengths of these microstructures at 850°C for the lower strain rate. Further work needs to concentrate on enumerating the reasons for the increased hardening at an increased temperature of 850°C . It is also not clear why the microstructure F with the fine precipitates does not show this hardening at 850°C .

Elasticity modulus: The elasticity (Young's) modulus of the microstructures shows a trend somewhat similar to the yield strength at both the strain rates. The modulus shows an anomalous increase in the range $650\text{-}750^\circ\text{C}$ for the lower strain rate, whereas it exhibits a more than normal decrease in this range for the higher strain rate with an attendant increase in the range $750\text{-}850^\circ\text{C}$. This behavior is clearly observable for all of the microstructures other than F. Whereas the yield strength is controlled by the first

movement of dislocations, the elasticity modulus should be independent of dislocation motion. The observed unexpected increase in elasticity modulus in the range 650-750°C and 750-850°C at the low and high strain rates, respectively, as for yield strength, would imply that a common process or phenomenon could be responsible for both parameters, which should be explored further. The observed elasticity modulus difference between the microstructures with the fine and the coarse precipitates can be due to the orientation differences in the specimens. The coarse precipitate microstructure which has the {200} preferred orientation is stretched along the soft <100> with attendant higher elastic strains and lower elasticity modulus at all temperatures. Likewise, the fine precipitate microstructure with the {220} preferred orientation being stretched along the <110> direction shows lower elastic strain and hence higher elasticity modulus.

Tensile Strength and Strain Hardening: The tensile strength behavior of the microstructures, shown in Fig. 34, again follows two distinct patterns—one for F and D, and the other for M and C. The former have slightly higher tensile strengths at room temperature than the latter in both the strain rate tests, and the latter two seem to pick up strength in the range RT to 650°C and become slightly stronger than the former two. Thereafter a reduction in strength is seen. On the contrary, the microstructures F and D show a continuous decrease in strength in the entire range. Although the increase or drop in the range RT to 750°C is not much, less than 10%, the drop is considerable from 750 to 850°C. This drop also is considerably larger in the case of lower strain rate, about 30% for all microstructures, than at the higher strain rate, about 10-15% only. These need to be studied further based on dislocation interactions. Strengthening seen for the microstructures M and C in the range RT to 650°C is perhaps due to enhanced strain

hardening found for these microstructures in this range, see Fig. 36. In fact, C, being the most strain-hardened microstructure, shows the highest tensile strength at 650°C.

Microstructure F behaves differently compared to the other microstructures. It not only strain hardens the least, but it also shows an anomalous increase in strain hardening in the range 650-750°C. The reason for this behavior is also not obvious.

% Elongation (δ , %): The microstructures C and M with the coarse and medium size precipitates exhibit maximum elongation and peaking at 650°C. In contrast F and D microstructures have lower elongation at high temperatures. Microstructure D shows not only twice as much elongation at room temperature under higher strain rate as compared to lower strain rate, the value drops off from RT to 650°C with the higher strain rate, whereas it increases under the lower strain rate to about a similar value at 650°C in this temperature range. In addition, anomalous increase in elongation is seen in the 750-850°C range, for C at lower strain rate and for M at the higher strain rate. These could again relate to dislocation - precipitate interactions.

Strain rate sensitivity: The change in the magnitude of the strain rate sensitivity of yield stress with changing temperature up to 750°C is almost negligible. Slightly negative strain rate sensitivity observed for most cases is due to the anomalous strengthening at 750°C with the lower strain rate. A further increase to positive values is due to strengthening with the higher strain rate in the temperature range 750-850°C.

The literature data pertaining to the tensile properties of a microstructure corresponding to the as-received microstructure of the present study is given in Table 8. The properties given in the literature are correlated to the ones obtained in the current study for the duplex-size microstructure, since the as-received microstructure evaluated

earlier in the literature is only a coarsened modification of the duplex-size microstructure studied here.

The tensile test results given in Ref. [105] were obtained after testing at a strain rate of 6.67×10^{-5} , which is very close to the lower strain rate of 5×10^{-5} used in the current work. Hence, the data of these two different studies for nearly analogous duplex-size microstructure should be comparable. The yield and tensile strength data obtained by Mirshams et al. [105] were slightly higher at 650°C and 750°C, but less at 850°C, than the values obtained in the present work at the respective temperatures. Their elongation values are also much higher at all temperatures. Likewise, because the strain rate (10^{-3}) used in Ref. [6] is the same as the higher strain rate used in the current work, results of these two studies on the nearly analogous duplex-size microstructure should be comparable.

Table 8. Tensile Properties of IN738LC extracted from plots given in the literature.

Reference*	T, °C	σ_y , MPa	σ_u , MPa	% Elongation	σ_y^{**} , MPa	σ_u^{**} , MPa	% Elongation**
Mirshams et al. [105] $\dot{\epsilon}=6.67 \times 10^{-5} \text{ s}^{-1}$	649	758	1069	19	739.7	818.1	12.1
	760	800	862	16	764.6	797.4	6.8
	871	517	620	18	633.5	654.2	5.1
Bieber et al. [15] $\dot{\epsilon}$, not reported	649	896	1069	3			
	760	790	965	5			
	871	551	758	8			
Bettge et al [6] $\dot{\epsilon}=10^{-3} \text{ s}^{-1}$	20	850	-	2	858.6	1031.3	16.0
	650	740	-	6	768.4	875.0	12.9
	750	780	-	8	761.6	817.9	6.5
	850	700	-	5	786.9	786.9	5.3

* The precipitate microstructures used in all of these references have been produced through the heat treatment of 1120°C/2h (accelerated air cooling) + 850°C/24h (furnace cooling), yielding a duplex-size (fine-spherical and coarse-cuboidal) precipitate microstructure with ~80 nm diameter and ~450 nm edge length, respectively [1].
 ** The values obtained in this dissertation work and already given in Table 7. The data given corresponds to the respective strain rates given in the table

The yield strength data obtained in the current study is higher than the ones given in Ref. [6] in the entire test temperature range of RT to 850°C, except at 750°C. Data of Bettge et al. [6] also shows the peaking of yield strength due to secondary hardening at 750°C instead of at 850°C as found in this current work. Their result is contradictory to the general peaking trend at higher strain rates occurring at around 850°C, as already stated. This could be due to finer size of the fine precipitates in the duplex-size microstructure of the current study. The % elongation data of the current study matches closely with the data given in Ref. [6] for the higher strain rate test at temperatures 750°C and 850°C, though the rest of the data does not show any match at all with the ones given. Also, no comparison with the results obtained by Bieber et al. [15] can be made because the strain rate used is not specified in the latter study. The differences could have been caused by differences in the microstructures tested. Although, the ones tested have duplex-size precipitate microstructure, they differ considerably in the size of the precipitates and in preferred orientation. The ones in the literature correspond to the as-received duplex-size microstructure that is coarsened (Fig. 3c) in contrast to the duplex-size precipitate microstructure studied in this work (Fig. 13f).

VI.2. Tensile Properties of Polycrystalline Superalloy IN738LC with the Fine-Size Precipitate Microstructure at 1200°C.

It was already discussed in the earlier sections on microstructure development that the fine-size precipitate microstructure (F) is obtained after holding at 1200°C and subsequent quenching in water. No growth of the precipitates or dissolution of them into the matrix was observed even after holding the specimens at 1200°C for ten days. This prompted the deduction that these fine precipitates could have been formed from a single-

phase solid solution matrix at some low temperatures during quenching. The tensile tests were conducted at 1200°C because of the deduction that this observed unusual microstructural property could result in some very peculiar mechanical properties of either the fine precipitate-containing microstructure (if the fine precipitates are stable at high temperatures) or of the single-phase solid solution matrix.

Four specimens supposedly containing the fine-size precipitate microstructure were tensile tested at 1200°C with the same two strain rates that were used for the lower temperature tensile tests (10^{-3} s^{-1} and $5 \times 10^{-5} \text{ s}^{-1}$). The results obtained were significantly different from the ones obtained at lower temperature testings. The 0.2% offset yield strength was only 10 MPa with the higher strain rate and 4 MPa with the lower strain rate, both of which are extremely low compared to the yield strength values obtained at and below 850°C, see Table 7. The yield strength values obtained at 1200°C were about 1.2% and 0.5% of the corresponding room temperature values with the higher and lower strain rates, respectively. Similarly, the tensile strength was also remarkably low at 1200°C, 11 MPa and 4.5 MPa with the higher and lower strain rates, respectively. Elasticity modulus of the fine-size precipitate microstructure at 1200°C was 13 GPa and 8 GPa with the higher and lower strain rates, respectively. No strain hardening was observed. Rather, after yielding, the material showed almost a constant strength for a while and then the stress dropped down sluggishly, leading to about 35% elongation with both the strain rates. This behavior clearly points to strain softening effects and to the fact that the fine precipitates are not any more effective in blocking the dislocation movement, and the matrix is also extremely soft. The calculated strain rate sensitivity was 0.31,

which indicates a superplastic behavior. Compared to this, the strain rate sensitivity was only 0.072 at 850°C and much lower at lower temperatures.

Studies on the mechanical behavior of the fine-size precipitate microstructure are not complete yet and more data needs to be collected still at temperatures close to 1250°C; however, the data obtained so far indicates that some improvement could be proposed in the future for the superplastic processing of this alloy. Preliminary results are included here to establish the two important facts in this work- first that the material is extremely soft at high temperatures around 1200°C and second that the material undergoes possibly superplastic deformation at and above the temperature range 1160-1225°C, which produces the single fine-size precipitates.

CHAPTER VII. RESULTS AND DISCUSSIONS: FRACTURE BEHAVIOR OF POLYCRYSTALLINE SUPERALLOY IN738LC

VII.1. Results

Results of fractographic study of specimens after the tensile test are given in Figs. 39-43. EDS analysis at selected locations on the fracture surface showed more number of carbides in the microstructures M and C regardless of the test variables (e.g., strain rate and temperature). The carbides were qualitatively determined to be (Ta, Ti)C, and were found to be situated at the grain boundaries as well as in the matrix. Size of the carbides varied between 5 and 10 μm . This size is much coarser relative to the γ' precipitate size, maximum size of which was found to be only $\sim 0.7 \mu\text{m}$. The fine precipitate microstructure F and the duplex precipitate microstructure D did not exhibit, on the contrary, any detectable amount of carbide inclusion on their fracture surfaces.

The fractographs showed, in general, dimple-ductile, quasi-cleavage, and faceted-cleavage type fracture modes in the tensile-fractured specimens. Regardless of the tensile test variables (microstructure, temperature, strain rate), most of the fractured specimens showed intergranular-type secondary cracks, Fig. 39. Particularly, microstructures with the medium and coarse size precipitates, M and C, showed long intergranular cracks, indicated by arrows, apparently following the columnar matrix grain boundaries, Fig. 40.

At room temperature, the microstructures SSS, F, and D showed a faceted-cleavage type fracture surface, Fig. 41a, b, c. Additionally, some of these specimens showed dimples, especially at the periphery. However, one of the specimens of D tested with the higher strain rate showed almost a complete dimple fracture, Fig. 41d. On the contrary, both M and C showed a dimple-ductile fracture at room temperature, Fig. 41e,f.

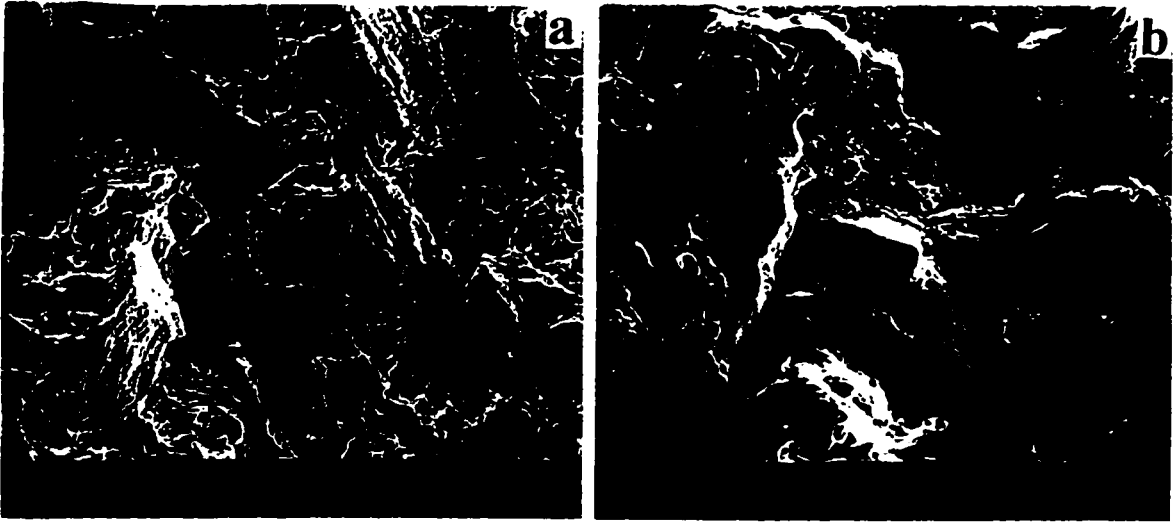


Figure 39. Fractographs showing the intergranular fracture with the microstructure

a) F b) C

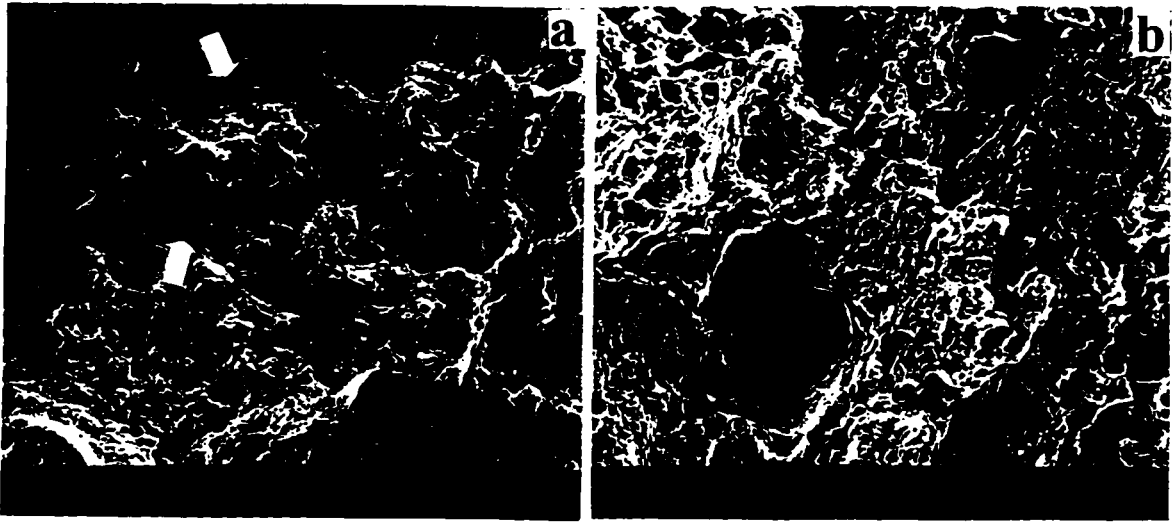


Figure 40. Fractographs showing the intergranular fracture with cracks possibly following the columnar matrix grain boundary

a) C b) M

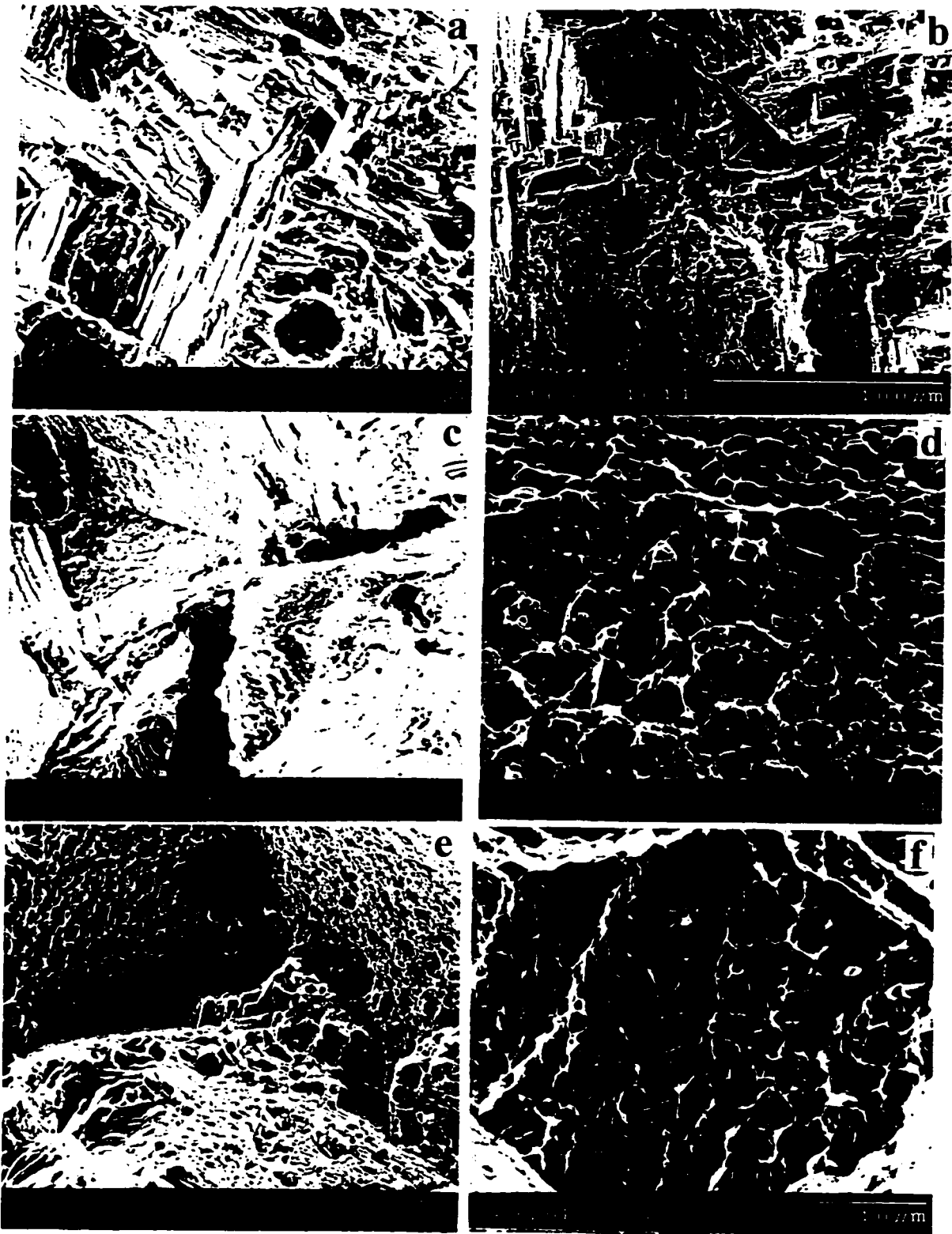


Figure 41. Fractographs showing the faceted-cleavage and dimple-ductile fracture observed at room temperature with

- | | | | |
|--------|------|------|------|
| a) SSS | b) F | c) D | d) D |
| e) M | f) C | | |

After testing at 650°C, F and D showed a quasi-cleavage type fracture and considerable amount of dimples associated with fracture, Fig. 42a,b. Faceted-cleavage is also visible. These two microstructures showed, however, dimple-ductile fracture at the periphery, Fig. 42c,d. The entire fracture surface of the microstructures M and C showed complete dimple fracture at 650°C, Fig. 42e,f.

At 750°C, the fracture behavior of the microstructure F was almost completely cleavage type again with indications of a fracture mode different from the faceted-cleavage parallel to $\{100\}$ corresponding to room temperature test specimens. Instead, the fracture at this temperature appeared to be initiated at a point and was spread around creating a flowery feature, Fig. 43a. Duplex-size microstructure again showed cleavage type fracture, and faceted features were still visible. Also, some dimples were observed on the fracture surface, Fig. 43b. The microstructures M and C showed also quasi-cleavage fracture surfaces. Figure 43c basically represents the fracture surface of both of these microstructures. However, specimen C showed a unique faceted total cleavage fracture with steps in some regions of only one specimen, Fig. 43d. The flat faces as well as the steps are wider than the ones observed on specimens with the other microstructures tested, compare Fig. 43d (C) with Figs. 41a (SSS), 41b (F), and 43b (D). A common feature of all of the microstructures tested at 750°C was that a slightly more cleavage-like feature could be inferred for the slower strain rate.

Static fracture toughness (energy-to-break the specimen, which is the area under the load vs. displacement curve, in the tensile test) data is given in Table 7 and is also plotted in Fig. 44. The toughness data shows meaningful variations as a function of microstructure, strain rate, and temperature. The M and C microstructures show

generally higher fracture toughness values than the F and D microstructures at analogous temperatures. In the lower strain rate tests, the toughness decreases from about 40 J to 5 J as the temperature is raised from RT to 850°C for the F microstructure. In the case of the other three microstructures, there is an increase in the toughness value in the range RT to 650°C, after which there is a large drop. For example, in the case of D, there seems to be about a 75% drop in the toughness when the temperature is raised from 650°C to 850°C, whereas it is about 50% in the case of M and C. Also, there seems to be a 25% increase in the range 750-850°C for C.

In the higher strain rate tests, F shows a nearly 200% increase in fracture toughness in the range RT to 650°C, above which it decreases drastically by about 75% in the range 650-750°C, and there is very little change in the range 750-850°C. On the contrary, D shows a continuous decrease in the range RT-850°C. Like F, M and C show an increase in the range RT-650°C, above which there is a continuous drop, but only about 25% in the case of C. The microstructure with the medium size precipitates, M, shows a reduction in the range 650-750°C of about 45%, but it shows an increase in the range 750-850°C of about 60%, back to its value at 650°C.

The reasons for the increase in fracture energy found in the range 750-850°C for the coarse (in lower strain rate tests) and for the medium (in the higher strain rate tests) precipitates cannot be enumerated at this stage. Further study on fracture processes in this temperature range is warranted.

VII.2. Discussion

More carbide particles of larger size than the γ' precipitates are found in the microstructures M and C than in the F and D. Since the alloy should possess similar

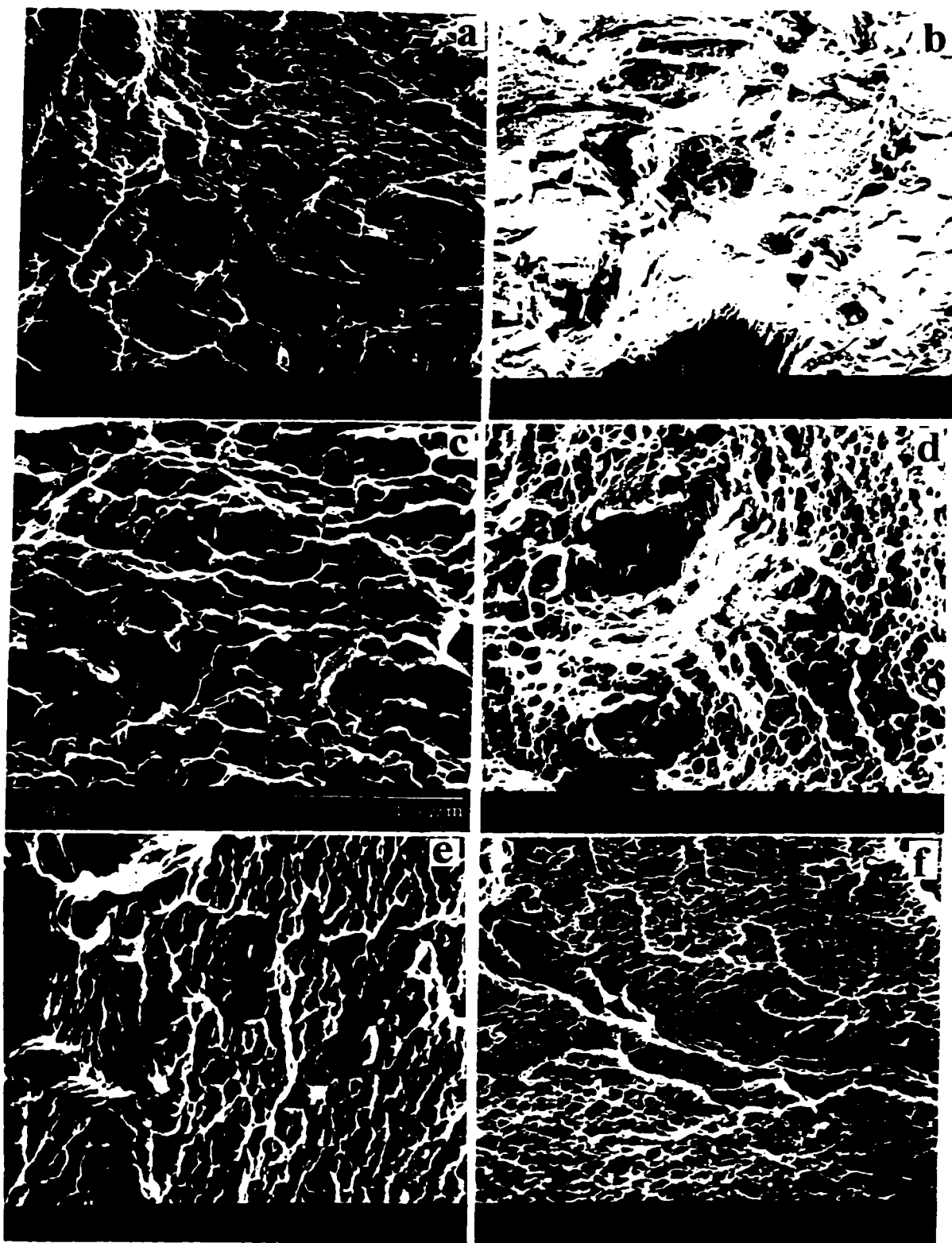


Figure 42. Fractographs showing the quasi-cleavage and dimple-ductile fracture observed at 650°C with

- | | | | |
|------|------|---------------------|---------------------|
| a) F | b) D | c) F (at periphery) | d) D (at periphery) |
| e) M | f) C | | |

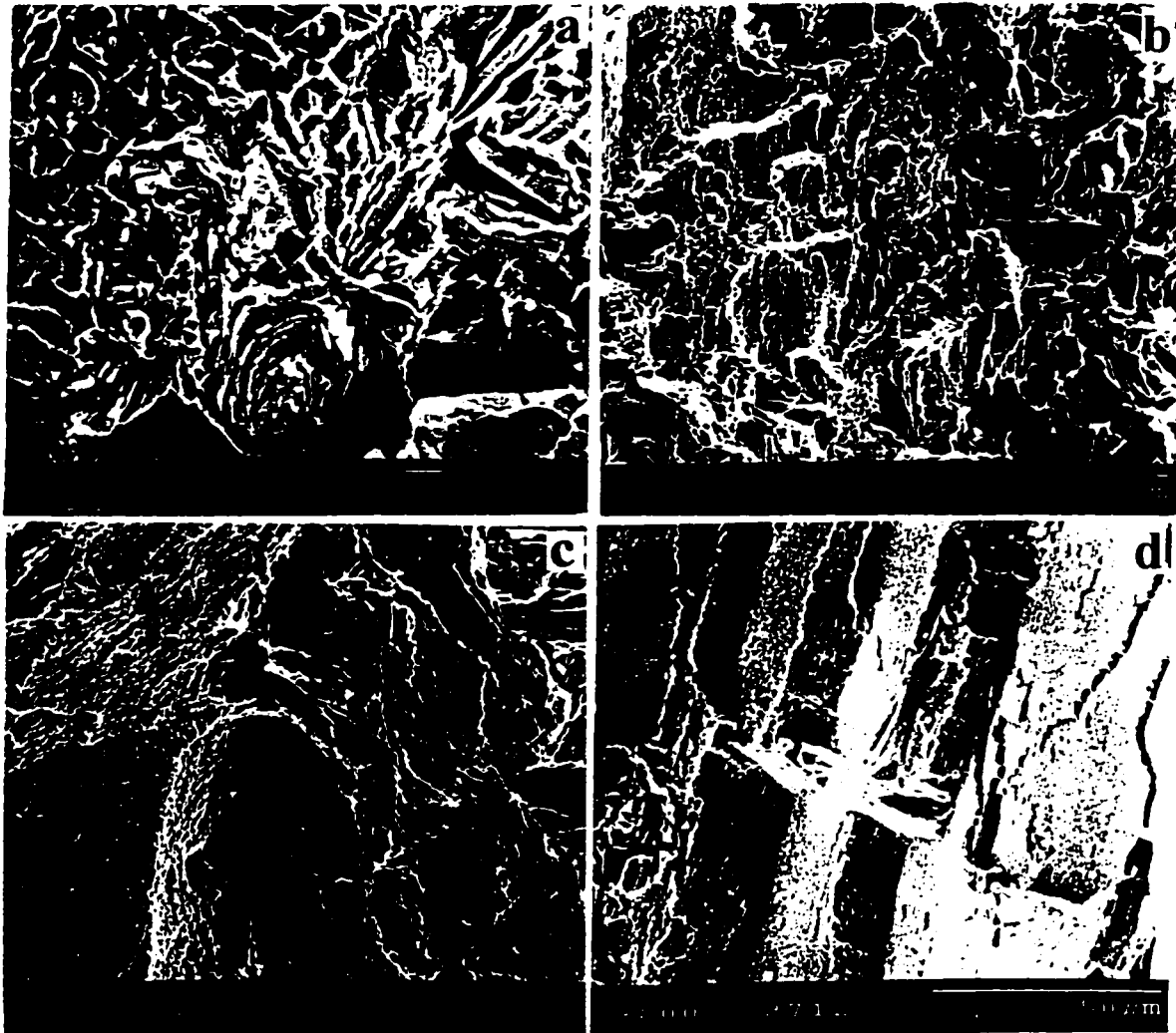


Figure 43. Fractographs showing the flowery, quasi-cleavage, and cleavage fracture observed at 750°C with

a) F

b) D

c) M and C

d) C

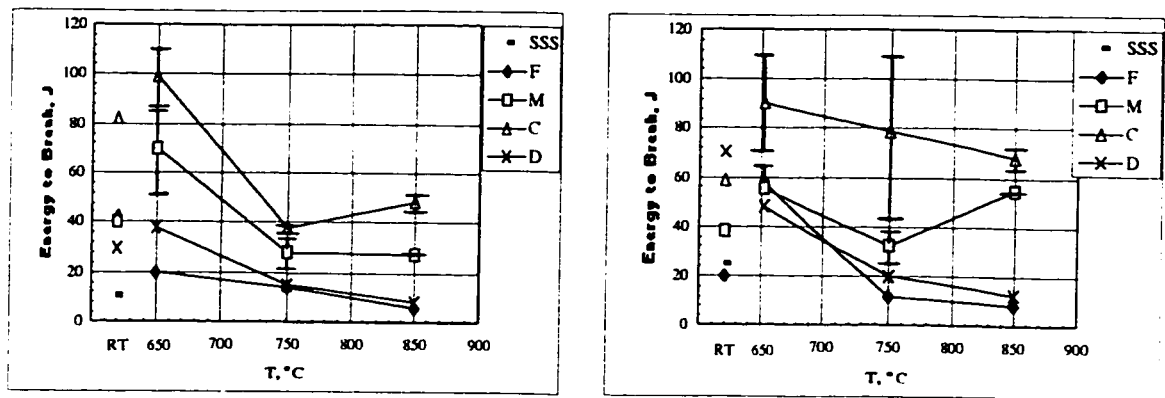


Figure 44. Plot of energy-to-break in the tensile tests with a) low strain rate ($5 \times 10^{-5} \text{ s}^{-1}$) b) high strain rate (10^{-3} s^{-1})

amount of carbide in all microstructures, it can be assumed that the carbides are present as very fine particles in F and D, and are not well resolved. This finer size of carbides observed in F and D could be due to the aging treatment carried out at somewhat higher temperatures leading to the breaking of the coarse particles and formation of fine ones. Concurrently, the carbide particles could have refined.

Grain boundary cracks, observed at all test temperatures in all of the fractographs of microstructures, indicate extreme brittleness of the grain boundaries. Particularly, the prevalence of dominant intergranular cracks in the microstructures M and C could be related to the more number of carbides found in these microstructures at the grain boundaries. The grain boundary carbides function possibly as crack initiation sites, and once initiated, the cracks propagate easily along the brittle grain boundary. Less number of grain boundary carbides observed in the microstructures F and D may be the reason why these microstructures show a less clear intergranular, but a more cleavage type fracture. Carbide and precipitates particles dispersed in the matrix could initiate

microvoids at their interface with the matrix, which would lead to dimples in the ductile fracture process of the matrix.

At room temperature, cleavage fracture of the F and D microstructures starts probably on the weak $\{100\}$ cleavage planes of the FCC matrix (Fig. 41b,c) as reported in Refs. [4,75, 77-79]. Their propagation leads to the faceted-cleavage fracture commonly observed in F and D. The fractograph in Fig. 41a, showing the faceted-cleavage fracture feature of the supersaturated solid solution SSS, also illustrates that the crack follows the $\{100\}$ cubic planes of the FCC structure in the supersaturated solid solution. This behavior also applies to the M and C in cases where they show somewhat flat (cleavage) fracture facets. When the advancing crack meets the precipitates, it still can propagate along the $\{100\}$ planes of the precipitate, since these are also the cleavage planes of the γ' precipitates and there is usually similar preferred orientation in both the matrix and precipitate.

In general, at all the test temperatures, the microstructures F and D showed more brittle behavior, while M and C show ductile type fracture. Some ductile features, such as tear-off dimples, were also observed in F and D at the periphery of the specimens. These tear-off dimples were not elongated, as usually expected, because the fracture mode was brittle and probably not enough deformation took place by the shear mode to create elongated dimples. However, one specimen with the duplex-size precipitate microstructure tested at the higher strain rate at room temperature showed a dimple ductile type fracture (Fig. 41d), which is not in line with the general behavior of the duplex-size microstructure as described above.

Cleavage fracture is also dominant at 750°C for all of the microstructures tested with slow strain rates. This might be due to the anomalous strengthening behavior of the alloy occurring at this temperature. Specimens tested with the higher strain rate at 750°C show quasi-cleavage, and this could be because the anomalous strengthening does not peak at 750°C with the higher strain rate, but rather it occurs at 850°C. It can be noted also that the cleavage feature observed at 750°C is quite different from the faceted {100} cleavage generally found at room temperature, compare Fig. 43a with Fig. 41b. A different cleavage mechanism or set of cleavage planes may be associated with this fracture morphology.

As expected and already discussed in section VI.1, the microstructures having fine-size precipitates (F and D) show higher yield strength, see Table 7. These microstructures also show lower energy values to break (static fracture toughness) under tensile loading conditions. This low toughness of the microstructures having fine precipitates might be associated with the cleavage type fracture. On the contrary, the microstructures having medium and coarse-size precipitates show higher toughness values, due possibly to their higher ductility leading to ductile mode of crack growth and a dimple fracture surface morphology. Further, the correlation of the fractographic features to fracture toughness in analogous testing conditions is very consistent at all of the test temperatures for all of the microstructures tested. For example, ductile fracture is seen at 650°C where the maximum toughness value is obtained, while brittle fracture is dominant at RT and 750°C where the lowest toughness values are registered.

**CHAPTER VIII. RESULTS AND DISCUSSIONS:
MICROSTRUCTURE EFFECT ON THE
THERMAL EXPANSION COEFFICIENT OF
POLYCRYSTALLINE IN738LC**

VIII.1. Results:

Thermal expansion was studied on similar microstructures, Fig.32, as for the tensile test. The test results obtained are shown in Fig. 45 wherein the thermal expansion coefficient α is plotted against the dwell temperature T at which the expansion data were collected. It can be observed in this figure that Ni₃Al has a uniformly increasing thermal expansion in the range 550-850°C, i.e., $d\alpha/dT$ is a constant in this range of temperature. The various microstructures of IN738LC also show a linear increase in the range 550-850°C, but the expansivity increases more (slope increases) in the range of 750 to 850°C (see Table 9). Fine (F), Fig. 32a, and duplex-size (D), Fig. 32d, precipitate microstructures as well as the solid solution phase (SSS) show a distinctly increased expansivity above 750°C. Also, a very slight increase in thermal expansion is detectable for the coarse, Fig. 32c, and annealed-duplex (AD) precipitate microstructures above 750°C. The microstructure with the medium-size precipitates (M), Fig. 32b, seems to show no increase in slope in the higher temperature range, as is the case with Ni₃Al. The expansivity plots of the solution-treated and the duplex-size precipitate microstructures fall noticeably below those of the others that grouped closely, with the solution-treated microstructure's thermal expansion being the lowest. Among the grouped ones, it is noticeable that the expansivity increases with increasing precipitate size. Fine-size precipitate microstructure shows a lower thermal expansion than the others in the group

at 550°C; however, as the temperature increases toward 850°C, its expansion also increases and becomes higher than that of the single phase Ni₃Al, unlike at 550°C.

The coarse precipitate microstructure persists with the highest expansion at all test temperatures. The thermal expansion of single phase Ni₃Al is similar to that of the coarse precipitate microstructure (highest) at lower temperatures, but above 780°C, its thermal expansion is the lowest, even lower than that of the fine precipitate microstructure.

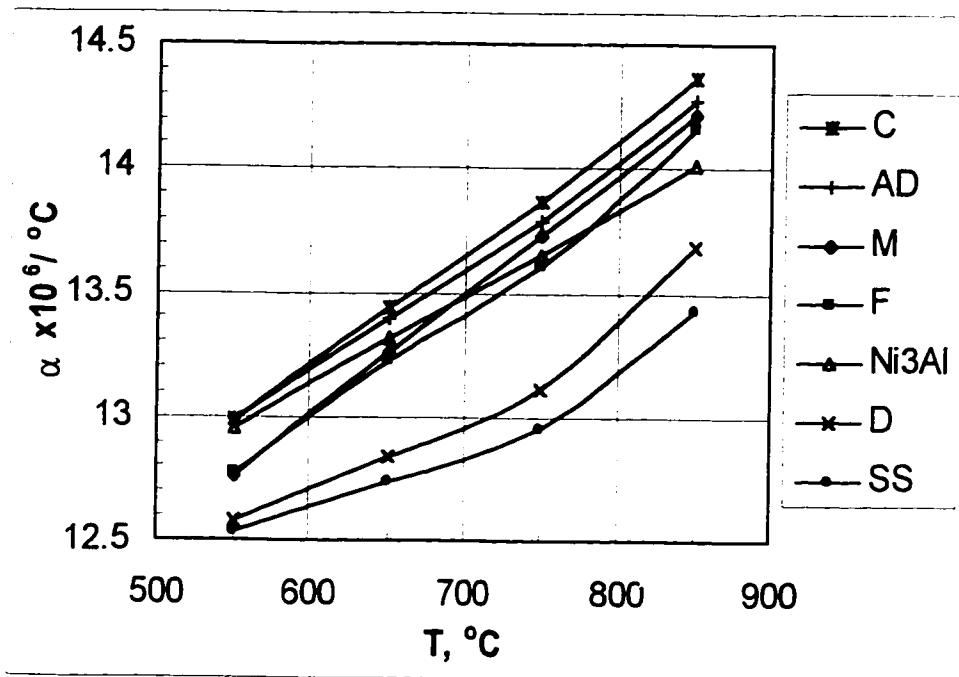


Figure 45. Coefficient of Linear Thermal Expansion of IN738LC with various precipitate microstructures.

The duplex-size precipitate microstructure (D) was aged at 950°C for 36 h after the first thermal expansion experiment. This treatment is designated as annealed duplex (AD). This was to see whether the fine precipitates in this microstructure coarsen and to

ascertain the effect on thermal expansion of any change in the duplex-size microstructure. There was a significant increase in the thermal expansion coefficient of this (AD) microstructure after the second aging treatment given above, even though there was no noticeable change in the sizes either of the coarse or of the fine precipitates in the duplex microstructure.

Measured matrix grain sizes along with the precipitate sizes for different microstructures and corresponding preferred orientation and the elasticity moduli data are given in Table 9. Also, included in Table 9 are the thermal expansion values of the microstructures at 750°C and the values of the $d\alpha/dT$ in the ranges 550-750°C and 750-850°C.

VIII.2. Discussion

The linear coefficient of thermal expansion of single-phase materials could be affected by the type of interatomic interactions, electronic configuration of bonded atoms, type of coordination and number of nearest neighbors, planar atomic density, grain boundary type and inclusions, and dislocation interactions, etc. However, when a material reinforced with a second phase constituent is investigated, there are some additional factors that need to be considered, such as volume fractions of the two phases, their elastic properties, continuity of the second phase in the matrix, and size and morphology of the second phase. Also, the interface characteristics between the matrix and the second phase should be taken into account.

Directional variation in the elastic properties (Young's modulus), preferred orientation of the precipitates and the matrix, and precipitate sizes are correlated to

thermal expansion in the following paragraphs to explain the observed differences in thermal expansion coefficient of the different precipitate microstructures.

Since thermal expansion is an elastic dilatation caused by the thermal forces, it can be considered to be related to the elasticity (Young's) modulus of materials. After all, the magnitude of the elasticity modulus is also determined by the same factors like interatomic distance, bond length and type, electronic configuration, and nearest neighbor interactions, etc.

Table 9- Grain and precipitate sizes, preferred orientation, experimental elasticity modulus, α , and $d\alpha/dT$ of the microstructures tested.

Micro-structure	Matrix		Average ppt. size, nm	Preferred Orientation *	E, GPa (measured at 20°C) [$\pm 8\%$]	α , $10^{-6}/^{\circ}\text{C}$ (at 750°C) [$\pm 3\%$]	$d\alpha/dT$, $10^{-6}/(^{\circ}\text{C})^2$	
	Grain size						550-750°C	750-850°C
	Radial	Axial						
C	Columnar	semi-	700	200	156	13.86	0.0043	0.0050
DA	Grains	Equiaxed	50 and 450	200		13.78	0.0039	0.0049
M	$\sim 2.4 \times 0.6$	~ 0.8 mm	450	200	156	13.74	0.0048	0.0048
F	mm size	Radius	70	220	164	13.61	0.0042	0.0054
D	Few columnar grains in axial and few equiaxed ones in		50 and 450	111, 200	162	13.11	0.0026	0.0057
SSS	Radial planes are also present			131	145	12.95	0.0020	0.0047
Ni ₃ Al						13.66	0.0035	0.0035

*in cases where two preferred orientations are given, the first one is the most dominant.

Precipitate sizes: **C**: coarse, **AD**: annealed-duplex, **M**: medium, **F**: fine, **D**: duplex, **SSS**: single phase supersaturated solid-solution.

Applying the generalized Hooke's law, it can be shown that the elasticity modulus of cubic crystals in different crystal directions can be given as follows [77,103]:

$$1/E_{hkl} = s_{11} - 2[(s_{11} - s_{12}) - \frac{1}{2}(s_{44})](l_h^2 l_k^2 + l_k^2 l_l^2 + l_h^2 l_l^2) \quad (14)$$

where E_{hkl} is the directional elasticity modulus, s_{ij} the elements of the compliance matrix, and l_i the direction cosines. As Eq. (14) indicates, the maximum value of E will be

obtained along $\langle 111 \rangle$, then along $\langle 110 \rangle$, and the lowest value will be along the $\langle 100 \rangle$ directions of the face centered cubic (FCC) crystals. It should be noted that the highest E value corresponds to the direction normal to the highest densely packed plane $\{111\}$, and, likewise, the lowest value corresponds to the direction normal to the lowest densely packed plane $\{100\}$. Highest modulus along a direction implies lower elastic expansion along that direction, and vice-versa.

To make an approximate estimation of the directional elastic properties of the superalloy IN738LC, the directional elasticity moduli for pure single crystal Ni, using Eq. (14), were calculated and found to be $E_{111} = 303$ GPa, $E_{110} = 232$ GPa, $E_{100} = 136$ GPa, and $E_{100} = 136$ GPa. The crude approximation that the directional variation of E in IN738LC is similar in magnitude as in pure nickel is justifiable because the superalloy has around 60 wt.% Ni and the same FCC structure like pure Ni. In these calculations, following values as given in Ref. [103] for s_{ij} of Ni were used: $s_{11} = 0.73 \cdot 10^{-11}/\text{Pa}$, $s_{12} = -0.27 \cdot 10^{-11}/\text{Pa}$, and $s_{44} = 0.80 \cdot 10^{-11}/\text{Pa}$. Similar values for the elasticity modulus were also reported: $E_{111} = 262$ GPa, $E_{110} = 215$ GPa, and $E_{100} = 138$ GPa, Ref. [106].

X ray diffraction results from several sets of specimens of heat treated IN738LC showed that the precipitate microstructures, which have gone through different heat treatment schedules to produce the different sizes of the precipitates, possess also different preferred orientations. These data are given in Table 5. Details of the X-ray study were already given in chapter V. Preferred orientation data along with the directional elasticity modulus of FCC crystals discussed above could be used to understand the observed differences in the thermal expansion coefficients of different precipitate microstructures having different preferred orientations. In this respect, if the

related preferred orientation data compiled from Table 5 and given in Table 9 is compared with the elasticity modulus data discussed above, it is easy to understand that the microstructure having the preferred orientation in the direction of highest value of elasticity modulus expands less, and vice-versa. For instance, the microstructure with the coarse cuboidal precipitates shows a $\langle 100 \rangle$ preferred orientation along the direction of expansion and expands the most. This result agrees with the data that FCC crystals have the lowest elasticity modulus and hence the largest elastic expansion along the $\langle 100 \rangle$ direction. Likewise, the fine size precipitate microstructure shows lower thermal expansion due to the $\langle 110 \rangle$ preferred orientation along which direction the elasticity modulus is medium. Furthermore, the duplex-size precipitate microstructure, having preferred orientation generally along $\langle 111 \rangle$ for the matrix with corresponding highest modulus and hence lowest expansion and $\langle 200 \rangle$ for the medium and fine-size precipitates, expands the least due probably to the elastic constraints from the matrix solid solution phase. The related experimentally obtained elasticity modulus data that was already presented in Table 8 is again given in Table 9. This data also confirms the above arguments. However, the experimental elasticity modulus value, being the lowest for the single phase supersaturated solid-solution matrix, does not match with the lower thermal expansion coefficient obtained for this microstructure. The lower expansion could be due to $\langle 111 \rangle$ preferred orientation which develops for the matrix during precipitation, sometimes being present along with the $\langle 131 \rangle$ orientation for the solid solution matrix. An alternate explanation could be that the supersaturation of solute in the matrix and resultant microstresses might be exerting the experienced constraints for the thermal expansion.

A very important observation is that when the duplex-size precipitate microstructure was aged for a second time at 950°C for 36h, a noticeable increase was seen in the thermal expansion. Concurrently, an increase in the slope $d\alpha/dT$ in the range 550-750°C and a decrease in the range 750-850°C, relative to the initial condition prior to second aging, were also observed. XRD data analysis (see chapter V) showed that the preferred orientation of the material changed to $\langle 200 \rangle$ after the second aging. As discussed above, $\langle 200 \rangle$ is the soft direction having the lowest elasticity modulus. Therefore, the change of the preferred orientation to the softest direction led to an increase in the thermal expansion and in $d\alpha/dT$.

Size effect of the strengthening particles on thermal expansion coefficient in composite materials has already been reported [107,108]. The authors observed that the smaller the size of the strengthening particle, the less the material expanded. This behavior was attributed to the interface interactions between the strengthening particles and the matrix phase. Existence of the particles gives rise to a distorted area at the interface, which constrains the matrix. Distorted interface could be due to different lattice sizes or different elastic properties that the phases may possess. The volume of the distorted area is inversely proportional to the particle size, so the microstructures having smaller particles would possess more distorted interfaces, which in turn would restrict matrix expansions more effectively due to the constraint strains.

Similar arguments could apply for precipitate microstructures studied here. Since the precipitate phase is the same in all of the microstructures, it cannot be argued that there might be an effect on the magnitude of the constricting strains at the interface due to a difference in the magnitude of elastic properties of the precipitate and the matrix

phases. Also, the volume fraction of the precipitate phase in all the microstructures is nearly the same, so no contribution should be expected due to any change in the volume fraction of the precipitate phase, either. However, if the same amount of the precipitate phase were dispersed in the matrix with a finer size, there would be a larger amount of interfacial area compared to the case having coarser precipitates. Therefore, the finer the precipitates, the more the interfacial area would be, which would give rise to more constraints in the matrix. Conversely, this discussion would be in line with the fact that the coarse precipitate microstructure expands more than the one having finer precipitates due to less interfacial constraints.

The rate of increase in α , i.e. $d\alpha/dT$, in the different microstructures is different in the different temperature ranges. Particularly, the ones that expand the least (the SSS and D) show lower $d\alpha/dT$ in the range 550-750°C, but the rate increases at 750°C to the level of the other microstructures. Also, the microstructure with the medium size precipitates shows the highest rate of increase in the entire temperature range (see Table 9). The reasons for these differences should be explored more carefully further.

CHAPTER IX. CONCLUSIONS

The following constitutes the salient conclusions from this study.

IX.1. Microstructure Development

1. The precipitates in IN738LC are $\text{Ni}_3(\text{Al}, \text{Ti})$, based on EPMA analysis. Also, volume fraction of γ' precipitates is 40-43% in the FC condition and 23-30% in the WQ condition after agings at various temperatures, at and below 1120°C . The volume fraction of the γ' precipitate phase can be considered to be nearly the same (approximately 26% for the WQ condition) in the temperature range $650\text{-}1225^\circ\text{C}$.

2. Various solution treatments carried out to determine the proper temperature and time for a complete γ' precipitate dissolution show that the $1120^\circ\text{C}/2\text{h}$ solution treatment is not adequate for a complete dissolution of the γ' precipitates. Also, different cooling rates including FC have no significant effect on the resulting microstructure after this solution treatment. A duplex-size precipitate microstructure is retained for γ' .

3. The $1200^\circ\text{C}/4\text{h}$ solution treatment gives the two-phase precipitated microstructure, but yields fine-size γ' precipitates. This temperature also is not high enough for a complete γ' dissolution. Increasing the holding time (e.g., to 24h, 72h, and 240h) and cooling by AAC, WQ, or iced-salt-water-quenching does not change the resulting solution-treated microstructure.

4. It is determined that $1235^\circ\text{C}/4\text{h}$ is the proper and minimum solutionizing treatment, which produces a single phase supersaturated solid solution in the water quenched condition (WQ).

5. The aging treatments conducted after the 1120°C/2h solutionizing do not disturb the microstructure significantly; resulting microstructures still retain the duplex-size distribution for γ' .
6. Agings after the 1200°C/4h and 1250°C/4h solution treatments give nearly similar microstructures. Following these solution treatments, single and double aging at a temperature between 650°C and 950°C give nearly spheroidal precipitates, and unimodal-cuboidal precipitates occur at around 1050°C up to 1130°C.
7. Triangular precipitates with possible octahedral surface morphology are found to be possible for the first time for γ' precipitates grown at 1120°C.
8. The 950°C/24h/FC aging treatment shows the transition from an incomplete cuboidal to a nearly complete cuboidal precipitate shape. Vastly increased holding times at this temperature might enable a completely cuboidal morphology.
9. For agings after 1200°C/4h and 1250°C/4h (AAC or WQ) solution treatments at high temperatures, precipitate growth mechanism during long time aging is mainly the particle coalescence, and solute absorption from the matrix during slow cooling (FC) leads to further coarsening.
10. The microstructure consists of single-size coarse precipitates up to 1130°C for 24h aging time. The duplex-size precipitate microstructure having two very distinct precipitate sizes (coarse + fine) prevails after longer aging times (≥ 48 h) at temperatures 1120-1130°C. However, the duplex-size microstructure appears within the first 5 minutes of aging in the range 1140-1150°C wherein the duplex-size precipitate morphology is found to be stable.

11. In Type-I heat treatment (starting from single-size fine precipitate microstructure), precipitates grow by coalescence as well as by the Ostwald ripening mechanism. The coarse precipitates grow in the cuboidal shape first, then the growth continues in spheroidal mode beyond 24h aging time at 1140°C aided by particle coalescence.

12. In Type-II heat treatment (starting from coarse precipitates), continuous dissolution of the coarse precipitates and the morphological change from cuboidal to spheroidal were observed in the range 1140-1150°C. Coarse particles also split into two or three smaller ones in the duplex-size zone.

13. The fine precipitates in the duplex-size precipitate microstructure appear to be very stable (no growth) even after aging for 96h at 1140°C. It is possible they are formed during quenching after aging.

14. “Corner dissolution” of coarse precipitates is one of the modes for the precipitate dissolution and formation of the fine precipitates of the duplex-size microstructure, and the other one is the dissolution of the newly grown smaller precipitates. Also, precipitate splitting aids in the dissolution and the eventual formation of fine-size precipitate microstructure.

15. Decreased corner radius and the lower interfacial energy of the {111} and {110} planes enable the “corner dissolution”. Attack on the former planes is more likely for cuboidals to convert to spheroidals in the dissolution mode.

16. The fine-size precipitate microstructure is formed within the first fifteen seconds during the agings in the range 1160-1225°C. The very coarse precipitates almost completely dissolve and the fine ones get formed in such a rapid-pace.

17. The fine-size precipitate microstructure was very stable (no growth) even after 240 hours of holding time at 1200°C. This may suggest the possibility that they are nucleated and grown during quenching from the high temperature after the dissolution of precipitates into the matrix has taken place.

18. Sharply decreased interfacial energy is perhaps the reason for the accommodation of large interfacial areas leading to the refined precipitate microstructure and preventing its growth at 1160-1225°C. This would be the case if the fine precipitates were stable at the given highest temperature range.

19. Solution treatments at 1235°C and 1250°C produce a single-phase supersaturated solid solution matrix after water quenching to room temperature.

20. The activation energy for the precipitate growth process is 150 kJ/mol (in the range 750-1050°C) and 298 kJ/mol (in the range 1050-1120°C) from precipitate size data for the FC condition, and 191 kJ/mol (in the range 850-1050°C) and 350 kJ/mol (in the range 1050-1120°C) from analogous data for the WQ condition.

21. Activation energy (at 1140°C) is calculated to be 685 ± 15 kJ/mol for the precipitate growth and 110 kJ/mol and 85 ± 20 kJ/mol for the precipitate dissolution process, the latter two values based on precipitate size data from Type-I and Type-II heat treatments, respectively.

22. The lower dissolution activation energy and the higher activation energy required for the precipitate growth in the duplex-size zone indicate that at and above 1140°C the dissolution process is more favorable, and its rate is higher when the temperature is close to 1160°C, the start of the fine precipitate region.

23. A more precise study of the precipitate coarsening features shows that the activation energy for the precipitate growth process is a polynomial function of temperature.

24. A 'Precipitate Agglomeration Model (PAM)' is proposed based on the result of continuously increasing Q for the growth of precipitates with temperature and size of the particles.

25. The reason for increased activation energy at higher temperatures (1050-1150°C) could be attributed to both the increased particle size and the spacing between the precipitates based on the assumption that the coarsening is via precipitate coalescence. An attractive force proportional to the surface area of the particle is proposed, drawn by which the particles move through a distance equal to the inter-particle spacing for merging together.

26. The energy for the precipitate coalescence is proposed to be a function of the product of the attractive force and the inter-particle distance. This results in Q being determined by a function of d^3 , i.e., by the volume or mass of the moving particles.

27. Extrapolation of Q to higher temperatures above 1150°C yields very high values indicative of severe restriction for the growth process.

28. The directional nature of alignment and consolidation of the cuboidal particles along $\langle 100 \rangle$ directions during aging at high temperatures and the possible anisotropy of the consolidation energy require further careful study.

IX.2. Preferred Orientation

1. The single-phase solid solution has a strong $\{131\}$ PO, which changes to $\{111\}$ as the solid solution is annealed.

2. Precipitates tend to favor the cube texture. $\{220\}$ orientation of fine-size precipitates changes to $\{200\}$, and medium-size and coarse-size precipitates possess $\{200\}$ preferred orientation.

3. In the duplex-size microstructure, matrix and precipitates have their individual PO, $\{111\}$ and $\{200\}$, respectively. In the other microstructures, matrix also acquires the same PO as that of the precipitate phase.

4. When the duplex-size precipitate microstructure is annealed for a long time at a lower temperature, the material loses its PO and becomes randomly oriented.

5. The misfit between the matrix and γ' precipitate phases is very small (0.17-0.36%), and in some cases it is almost zero.

IX.3. Tensile Properties

1. The tensile mechanical properties of IN738LC with different precipitate microstructures arrange themselves in two general groups – one for the microstructures with the coarse (C) and medium (M) size precipitates, and the other for the microstructures with the fine (F) and duplex-size (D) precipitates. The behavior of microstructures in a group is nearly similar.

2. Variations of yield strength and elasticity modulus of the microstructures with temperature show nearly similar trend. Likewise, the variations of tensile strength, strain hardening, and % elongation with temperature seem to have close similarities.

3. The yield strength shows an anomalous increase in the range 650-750°C with the lower strain rate, but with the higher strain rate this occurs in the range 750-850°C. The elasticity modulus seems to exhibit similar features.

4. The tensile strength of C and M microstructures seems to increase slightly in the range RT to 650°C, which seems to be related to an increase in strain hardening in this temperature range for these microstructures. The concurrent increase in % elongation seen for these microstructures in this temperature range appears to be anomalous and cannot be correlated to the strain hardening or strengthening.

5. There is an anomalous reduction in % elongation in the range 650-850°C for most of the microstructures. However, microstructure C shows an increase in the range 750-850°C with the lower strain rate and the microstructure M shows a similar increase in the same range of temperature, but with the higher strain rate.

6. The reasons for the varied behavior of the different microstructures should be correlated to the dislocation - precipitate interactions at the different temperatures. The anomalous hardening known to occur in Ni₃Al-type intermetallic compounds could be partially responsible for the anomalous strengthening in IN738LC at 750°C or 850°C.

IX.4. Fracture Behavior

1. Tensile fracture in IN738LC shows the features of faceted-cleavage in specimens with fine (F), duplex (D), and supersaturated solid solution matrix phase only (SSS), whereas dimple ductile fracture occurs in specimens with coarse (C) and medium (M) size precipitates after the tests at RT.

2. M and C generally show more dimple ductile fracture than F and D at all temperatures.

3. Dimple fracture or quasi-cleavage fracture is dominant at 650°C. The cleavage or quasi-cleavage mode prevails at 750°C for all of the microstructures. This is attributed

to the anomalous strengthening occurring at this temperature under slow strain rate testing.

4. The fracture feature correlates to ductility as well as to static energy fracture toughness exhibited by the specimens. M and C with the higher toughness and % elongation show ductile dimple mode of fracture, while F and D with lower fracture toughness give rise to cleavage fracture.

5. Cleavage fracture found at 750°C is different from the faceted {100} planar cleavage found at RT. This should be attributed possibly to a different strengthening mechanism prevailing at this temperature.

6. The dimples are attributed to harder γ' particles and to the presence of carbides in the microstructure contributing to microvoid formation and their coalescence. Intergranular mode of fracture observed is attributed mainly to the existence of the grain boundary carbides.

IX.5. Thermal Expansion

1. Microstructural changes are determining factors in the thermal expansion of materials.

2. The larger the precipitate size, the higher is the magnitude of thermal expansion.

3. The microstructures oriented along the $\langle 100 \rangle$ soft directions, such as M and C, show higher thermal expansion.

4. Higher thermal expansion is also observed with the precipitate microstructures having lower elasticity modulus.

5. The quenched-in supersaturated solid solution material (SSS) shows the lower thermal expansion coefficient which is attributed to the $\langle 111 \rangle$ preferred orientation along the direction of expansion and possibly also to constraints from microstresses due to solute supersaturation in the matrix.

CHAPTER X. SUGGESTIONS FOR FUTURE WORK IN THIS RESEARCH AREA

Based on the results obtained in this project, considering also the industrial needs, the following can be suggested for further in-depth study:

1. Difference in the activation energy of IN738LC in furnace-cooled and water-quenched conditions: In this study, a theoretical model can be proposed to account for the differences in the activation energies observed in the two cooling conditions.
2. Superplastic behavior that is briefly outlined in this dissertation certainly requires more work.
3. Also, fine-size precipitate microstructure, which does not grow after 10 days of aging treatment at 1200°C, needs more precise analysis, such as a TEM study. If these fine precipitates are formed during quenching, suitable experiments should be devised to verify this. In-situ TEM observation at 1200°C could verify this indirectly.
4. Deformation Mechanisms of IN738LC at High Temperatures: Slip mechanism(s) and dislocation precipitate interactions can be studied under tensile loading conditions.

These are some of the possible areas for future investigations and certainly it might take a long time to cover all aspects of the problems in their entire depth. This brief list only illustrates the richness of the project undertaken and further studies needed thereon to understand the behavior of IN738LC thoroughly.

REFERENCES

1. C. G. Bieber, Suffern, and J. J. Galka: United States Patent Office, No: 3459545, August 1969
2. D. Mukherji, F. Jiao, W. Chen, and R.P. Wahi: *Acta Metall. Mater.*, 1991, vol. 39(7), pp. 1515-1524.
3. J. Li, R. P. Wahi, H. Chen, W. Chen, and H. Wever: *Z. Metallkunde*, 1993, vol. 84(4), pp. 268-272.
4. J. Li and R. P. Wahi: *Acta Metall. Mater.*, 1995, vol. 43(2), pp. 507-517.
5. Y. Wang, D. Mukherji, W. Chen, T. Kutter, R. P. Wahi, and H. Wever: *Z. Metallkunde*, 1995, vol. 86(5), pp. 365-370.
6. D. Bettge, W. Osterle, and J. Ziebs: *Z. Metallkunde*, 1995, vol. 86(3), pp. 190-197.
7. F. Jiao, J. Zhu, R. P. Wahi, H. Chen, W. Chen, and H. Wever: *Proc. Conf. "LCF and Elasto-Plastic Behavior of Materials"*, Ed. by K. T. Rie, Elsevier Applied Science, London, 1992, pp. 298-303.
8. J. Ziebs, K. Naseband, and H. J. Kuhn: *ibid.*, pp. 369-374.
9. J. Ziebs, J. Meersman, H. J. Kuhn, and S. Ledworuski: *ibid.*, pp. 248-255.
10. H. Chen, W. Chen, D. Mukherji, R. P. Wahi, and H. Wever: *Z. Metallkunde*, 1995, vol. 86(6), pp. 423-427.
11. T. Malow, J. Zhu, and R. P. Wahi: *Z. Metallkunde*, 1994, vol. 85(1), pp. 9-19.
12. J. K. Tien and T. Caulfield: *Superalloys, Supercomposites, and Superceramics*, Academic Press, Inc., NY, 1989, p132
13. L. Liu, F. Sommer, and H. Z. Fu: *Scripta Metall. and Mater.*, 1994, vol. 30, pp. 587-591
14. L. Liu, B. L. Zhen, A. Banerji, W. Reif, and F. Sommer: *Scripta Metall. and Mater.*, 1994, vol. 30, pp. 593-598
15. C. G. Bieber and J. R. Mihalisin: *Proc. Second International Conference on the Strength of Metals and Alloys*, Pacific Groove, CA, 1970, American Society for Metals, Metals Park, OH, vol. III, 1970, pp. 1031-1036.

16. W. P. Foo and R. Castillo: *J. of Eng. for Gas turbines and Power*, 1992, vol. 114, pp. 275-283.
17. M. A. Burke, C. G. Beck, Jr., and E. A. Crombie: *Superalloys 1984*, Proc. of the Fifth International Symposium on Superalloys, The Metallurgical Society of AIME, Champion, PA, October 1984, AIME, Warrendale, PA, 1984, pp. 63-71.
18. M. Marchionni, D. Ranucci, and E. Picco in *Proc. High Temperature Alloys for Gas turbines 1982*, Liege, Belgium, 1982, Kluwer, Boston, 1982, pp. 791-804.
19. K. Kusabiraki, X. Zhang, and T. Ooka: *ISIJ International*, 1995, vol. 35(9), pp.1115-1120.
20. R. D. Doherty: *Metal Science*, 1982, vol. 16, pp 1-13.
21. P.W. Voorhees and W.C. Johnson: *Phys. Rev. Let.*, 1988, vol. 61(19), pp. 2225-2228.
22. C.K.L. Davies, P. Nash, and R.N. Stevens: *Acta Metall.*, 1980, vol. 28, pp. 179-189.
23. K. Tsumuraya and Y. Miyata: *Acta Metall.* 1983, vol. 31(3), pp. 437-452.
24. W.C. Johnson, P.W. Voorhees, and D.E. Zupon: *Metal. Trans.*, 1989, vol. 20A, pp. 1175-1189.
25. H.A. Calderon, P.W. Voorhees, J.L. Murray, and G. Kostorz: *Acta Metall. Mater.*, 1994, vol. 42(3), pp. 991-1000.
26. T.L. Wolfsdorf, Bender, W.H., and P.W. Voorhees: *Acta Mater.*, 1997, vol. 45(6), pp. 2279-2295.
27. R.A. Ricks, A.J. Porter, and R.C. Ecob: *Acta Metall.*, 1983, vol. 31, pp. 43-53.
28. C.H. Su and P.W. Voorhees: *Acta Mater.*, 1996, vol. 44(5), pp. 1987-1999.
29. W.C. Johnson and P.W. Voorhees: *J. Appl. Phys.*, 1987, vol. 61(4), pp. 1610-1619.
30. W.C. Johnson, T.A. Abinandanan, and P.W. Voorhees : *Acta Metall. Mater.*, 1990, vol. 38(7), pp. 1349-1367.
31. M. McCormack, A.G. Khachaturyan, and J.W. Morris: *Acta Metall. Mater.*, 1992, vol. 40(2), pp. 325-336.
32. T.A. Abinandanan and W.C. Johnson: *Acta Metall. Mater.*, 1993, vol. 41(1), pp. 17-25.

33. Y. Wang., L.Q. Chen, and A.G. Khachaturyan: *Acta Metall. Mater.*, 1993, vol. 41(1), pp. 279-296.
34. S. Socrate and D.M. Parks: *Acta Metall. Mater.*, 1993, vol. 41(7), pp. 2185-2209.
35. T.A. Abinandanan and W.C. Johnson: *Acta Metall. Mater.*, 1993, vol. 41(1), pp. 27-39.
36. W. Hort and W.C. Johnson: *Metall. and Mater. Trans.*, 1994, vol. 25A, pp. 2695-2703.
37. M. Fahrman, P. Fratzl, O. Paris, E. Fahrman, and W.C. Johnson: *Acta Metall. Mater.*, 1995, vol. 43(3), pp. 1007-1022.
38. Y. Wang and A.G. Khachaturyan: *Acta Metall. Mater.*, 1995, vol. 43(5), pp. 1837-1857.
39. J. Y. Huh and W.C. Johnson: *Acta Metall. Mater.*, 1995, vol. 43(4), pp. 1631-1642.
40. C.H. Su and P.W. Voorhees: *Acta Mater.*, 1996, vol. 44(5), pp. 2001-2016.
41. F.R.N. Nabarro, C.M. Cress, and P. Kotschy: *Acta Mater.*, 1996, vol. 44(8), pp. 3189-3198.
42. M.E. Gurtin and P.W. Voorhees: *Acta Mater.*, 1996, vol. 44(1), pp. 235-247.
43. J. Svoboda and P. Lukas: *Acta Mater.*, 1996, vol. 44(6), pp. 2557-2565.
44. W.C. Johnson : *Metall. and Mater. Trans.*, 1997, vol. 28A, pp. 27-38.
45. Y. Mou and J.M. Howe: *Metall. and Mater. Trans.*, 1997, vol. 28A, pp. 39-50.
46. Y. Mou and J.M. Howe: *Acta Mater.*, 1997, vol. 45(2), pp. 823-835.
47. D.Y. Li and L.Q. Chen: *Acta Mater.*, 1997, vol. 45(6), pp. 2435-2442.
48. G. Solorzano: *J. de Physique IV*, 1993, vol. 3(C7), pp. 2021-2026.
49. M. Tanaka: *J. Mater. Sci.*: 1994, vol. 29, pp. 4093-4098.
50. B. Radhakrishnan and R.G. Thompson: *Metall. Trans.*, 1993, vol. 24A, pp. 2773-2785.
51. J. Friedel: *Dislocations*, Pergamon Press, New York, 1964, pp. 211-216.

52. J.C. Ion, K.E. Easterling, and M.F. Ashby: *Acta Metall. Mater.*, 1984, vol. 32, pp. 1949-1962.
53. H.B. Aaron and G.R. Kotler: *Metall. Trans.*, 1971, vol.2, pp. 393-408.
54. F.J. Vermolen and S. Zwaag: *Mater. Sci. and Engn.*, 1996, vol. A220, pp. 140-146.
55. J.J. Becker: *Transactions AIME, Journal of Metals*, 1951, vol. 191, p.115.
56. P.A. Beck: *Acta Metall.*, 1953, vol. 1, pp. 230-234.
57. V. Novikov: *Grain growth and Control of Microstructure and Texture in Polycrystalline Materials*, CRC Press, NY, 1997, pp. 136-139.
58. T.J. Koppenaal, M.N. Parthasarathi, P.A. Beck: *Transactions of the Metallurgical Society of AIME*, 1960, vol. 218, pp. 98-102.
59. I.L. Dillamore, W.T. Roberts: *Acta Metall.*, 1964, vol. 12, pp. 281-293.
60. P.J. Evens, J.W. Martin, E.A. Little, : *Materials Science and Technology*, 1992, vol. 8, pp. 531-536.
61. C.A. Gandin, M. Rappaz, D. West, B.L. Adams: *Metall. and Mater. Trans.*, 1995, vol. 26A, pp. 1543-1551.
62. C.A. Gater, J.W. Martin: *Materials Science and Technology*, 1996, vol. 12, pp. 613-614.
63. D. Calliard, A. Couret, and G. Molenat: *Mater. Sci. and Engg.*, 1993, vol. A164, pp. 69-81.
64. G. Saada and P. Veyssiere: *Philos. Mag. Lett.*, 1991, vol. 64, pp. 365-374.
65. B. A. Grinberg, M. A. Ivanov, Y. N. Gornostyrev, and L. I. Yakonevko: *Phys. Met. Metall.*, 1979, vol. 46(4), pp. 117-139.
66. S. Takeuchi and E. Kuramoto: *Acta Metall.*, 1973, vol. 21, pp. 415-425.
67. V. Paidar, D. P. Pope, and V. Vitek: *Acta Metall.*, 1984, vol. 32(3), pp. 435-448.
68. P. B. Hirsch: *Strength of Metals and Alloys*, 1991, vol. 1, p. 3.
69. T. L. Lin and M. Wen: *Materials Sci. and Eng.*, 1990, vol. A128, pp. 23-31.

70. R. R. Jensen and J.K. Tien: *Metal. Trans.*, 1985, vol. 16A, pp. 1049-1068.
71. G. R. Leverant, M. Gell, and S. W. Hopkins: *Proc. Second International Conference on the Strength of Metals and Alloys*, Pacific Grove, CA, 1970, American Society for Metals, Metals park, OH, vol. III, 1971, pp. 1141-1144.
72. M. F. Kniepmeier, T. Link, I. Poschmann, G. S. Frerker, and C. Schulze: *Acta Mater.* 1996, vol. 44(6), pp. 2397-2407.
73. D.P. Pope and S.S. Ezz: *Intl. Met. Rev.*, 1984, vol. 29(3), pp. 136-167.
74. A. Berkovits, S. Nadiv, and G. Shalev: *Acta Metall. Mater.*, 1995, vol. 43(7), pp. 2605-2613.
75. G. Jianting, D. Ranucci, E. Picco, and P.M. Strocchi: *Metall. Trans.*, 1983, vol. 14A, pp. 2329-2335.
76. K.M. Chang, M.F. Henry, and M.G. Benz: *Journal of Metals*, 1990, vol. 42(12), pp. 29-35.
77. D.L. Anton: *Acta Metall.*, 1984, vol. 32(10), pp. 1669-1679.
78. A. Sengupta and S.K. Putatunda: *Scripta Metall. Mater.*, 1994, vol. 31(9), pp. 1163-1168.
79. M.B. Henderson and J.W. Martin: *Acta Metall. Mater.*, 1995, vol. 43(11), pp. 4035-4043.
80. S.H. Ai, V. Lupinc, and G. Onofrio: *Scripta Metall. Mater.*, 1993, vol. 29, pp. 1385-1390.
81. R.S. Krishnan, R. Srinivasan, and, S. Devanarayan: *Thermal Expansion of Crystals*, Pergamon Press, 1979, pp. 1-5.
82. R.A. MacDonald: *Thermal Expansion-8*, edited by T. A. Hahn, Plenum Press, NY, 1984, pp. 11-19.
83. K.V.K. Rao: *Thermal Expansion-1973*, edited by R.E. Taylor and G.L. Denman, AIP Conference Proceedings, vol. 17, AIP, NY, 1974, pp. 219-230.
84. H.D. Megaw: *Mat. Res. Bull.*, 1971, vol. 6, pp. 1007-1018.
85. Y. Benveniste: *Int. J. Solids Structures*, 1997, vol. 34(7), pp. 789-798.
86. R K. Williams, R S. Graves, F J. Weaver, and D L. McElroy: *Proc. Mat. Res. Soc. Symp.*, Materials Research Society, PA, 1985, vol. 39, pp. 505-511.

87. S V. Rabinovich, M.D. Kharchuk, and V.I. Chermenski: *Steels in Translation*, 1994, vol. 24(10), pp. 41-44.
88. G.W. Hollenberg and R. Ruh: *Thermal Expansion-1973*, edited by R. E. Taylor and G.L. Denman, AIP Conference Proceedings, vol. 17, AIP, NY, 1974, pp. 241-255.
89. H.B. Huntington: *Solid State Physics*, 1958, vol. 7, p. 342.
90. H.P. Kicher: *Thermal Expansion-1971*, edited by M.G. Graham and H.E. Hagy, AIP Conference Proceedings, vol. 3, AIP, NY, 1972, pp. 269-277.
91. G.N. Maniar and J.E. Bridge: *Metallography*, 1972, vol. 5, pp. 91-93.
92. W.E. Schoknecht, R.O. Simmons: *Thermal Expansion-1971*, edited by M.G. Graham and H.E. Hagy, AIP Conference Proceedings, vol. 3, AIP, NY, 1972, pp. 169-182.
93. ASTM E8-95a, "Standard Test Methods for Tension Testing of Metallic Materials", *Annual Book of ASTM Standards*, American Society for Testing and Materials, West Conshohocken, PA, 1995, vol. 03.01, pp. 56-76.
- ASTM E21-92, "Standard Test Methods for Elevated Temperature Tension Tests of Metallic Materials", *Annual Book of ASTM Standards*, American Society for Testing and Materials, West Conshohocken, PA, 1992, vol. 03.01, pp. 129-136.
94. ASTM E228-95 "Standard Test Method for Linear Thermal Expansion of Solid Materials with a Vitreous Silica Dilatometer", *Annual Book of ASTM Standards*, American Society for Testing and Materials, West Conshohocken, PA, 1995, vol. 1402, p. 129.
95. H.B. Aaron, D. Fainstein, and G.R. Kotler: *Journal of Applied Physics*, 1970, vol. 41, pp. 4404-4410.
96. V. O. Yesin, V. I. Danilyuk, and V. N. Porozkow: *Phys. Met. Metall.*, 1979, vol. 46(1), pp. 80-85.
97. R. E. Reed-Hill and R. Abbaschian: *Physical Metallurgy Principles*, 3rd ed., PWS-Kent Publishing Company, Boston, 1992, pp. 256-261.
98. D. A. Porter and K. E. Easterling: *Phase Transformation in Metals and Alloys*, 2nd ed., Chapman & Hall, NY, 1993, pp. 44-47, 116, 314-317.
99. D. V. Ragone: *Thermodynamics of Materials-2*, John Wiley & Sons, NY, 1995, pp. 98-101.

100. B. Chalmers: *Physical Metallurgy*, John Wiley & Sons, New York, 1962, p. 131.
101. B.W. Batterman: *J. Applied Physics*, 1957, vol. 28(11), pp. 1236-1241.
102. B.D. Agarwal and L.J. Broutman: *Analysis and Performance of Fiber Composites*, 2nd ed., John Wiley & Sons, Inc., New York, NY, 1990.
103. R. W. Hertzberg: *Deformation and Fracture Mechanics of Engineering Materials*, 3rd ed., John Wiley & Sons, Inc., NY, 1989, pp. 3-14.
104. G. Z. Voyiadjis and W. Huang: *Proceeding of the 13th Riso International Symposium on Materials Science: Modelling of Plastic Deformation and Its Engineering Applications*.
Editors: S. I Anderson, J. B. Bilde-Sorensen, N. Hansen, D. J. Jensen,
T. Leffers, H. Lilholt, T. Lorentzen, O. B. Pedersen, and B. Ralph, Riso National Laboratory, Roskilde, Denmark, 1992, pp. 491-496.
105. R. A. Mirshams, Z. X. Li, and P. Mohamadian: *Proc. Fourth Annual Historically Black Colleges and Universities/Private Sector Energy Research and Development Technology Transfer Symposium*, Greensboro, NC, 1996, U.S. DoE, Washington, D.C., 1996, pp. 99-102.
106. G. V. Samsonov: *Handbook of the Physicochemical Properties of the Elements*, IFI/Plenum Data Corp., NY, 1968, p. 389.
107. Z. R. Xu, K. K. Chawla, R. Mitra, and M. E. Fine: *Scripta Metall. et Mater.*, 1994, vol. 31(11), pp. 1525-1530.
108. M. D. F. Pinheiro and H. M. Rosenberg: *Journal of Polymer Science, Polymer Physics Edition*, 1980, vol. 18, pp. 217-225.

VITA

Ercan Balikci was born on May 10, 1967, in Ardahan, Turkey. After completing his bachelor study in 1988 in the Metallurgy division of Technical Educational Faculty in Marmara University, Istanbul, Turkey, he continued his graduate studies at the same place and received his Master of Science degree in Metal Education. Thereafter, he was awarded a scholarship in 1993 through a YOK (Higher Education Council of Turkey) program by the Turkish government, which enabled him to go to the United States of America for his doctoral studies. The aim of this YOK program was to train new faculties and scholars to be appointed in the recently founded state universities nationwide in Turkey. He began his doctoral studies in the Materials Science and Engineering Program, Mechanical Engineering Department, Louisiana State University, Baton Rouge, Louisiana, in June 1994, and is currently a doctoral candidate for the degree of Doctor of Philosophy to be awarded during the spring commencement, 1998.

DOCTORAL EXAMINATION AND DISSERTATION REPORT

Candidate: Ercan Balikci

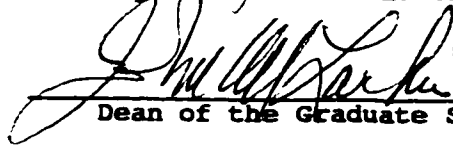
Major Field: Engineering Science

Title of Dissertation: Microstructure Evolution and Its Influence on Thermal Expansion and Tensile Properties of the Superalloy IN738LC at High Temperatures

Approved:

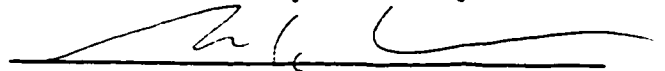
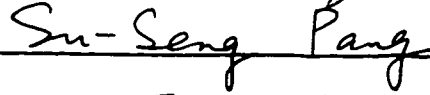
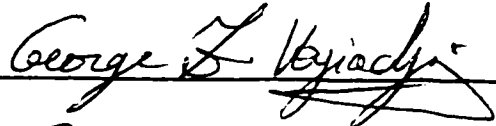


Major Professor and Chairman



Dean of the Graduate School

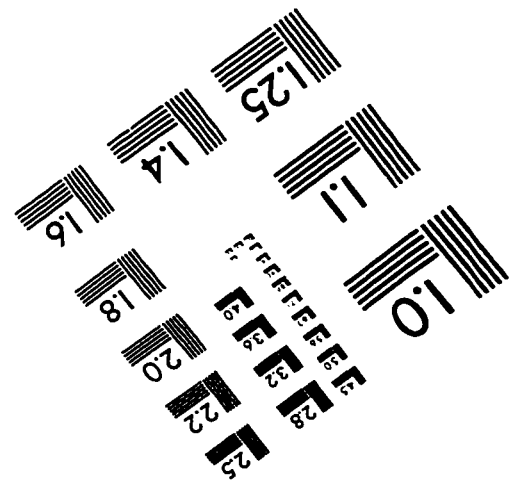
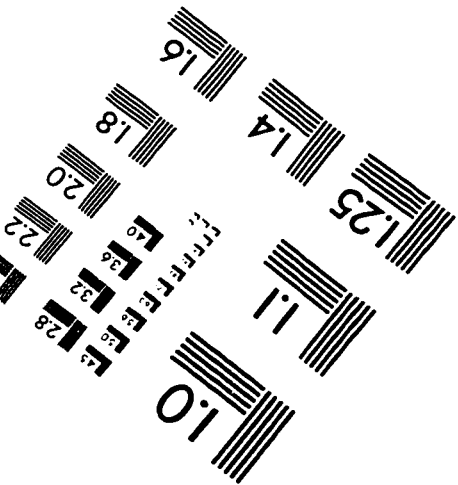
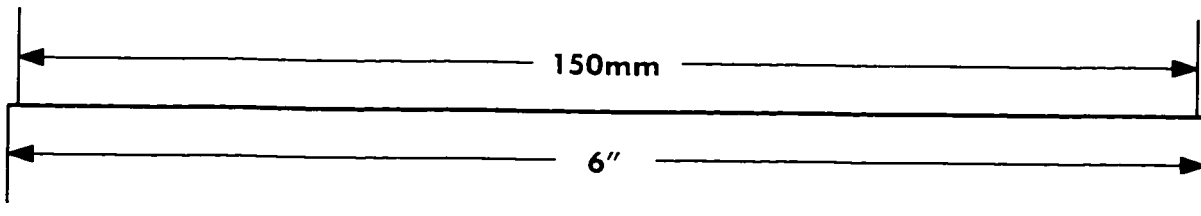
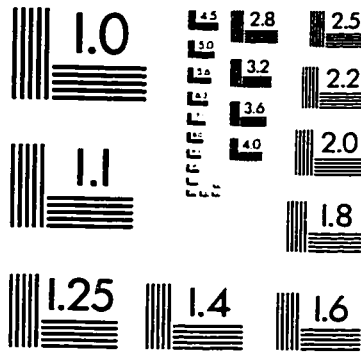
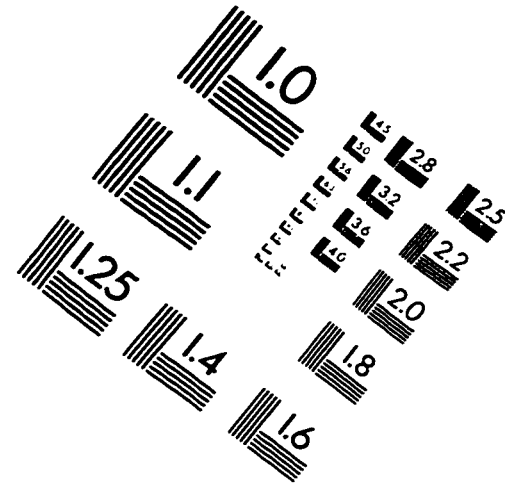
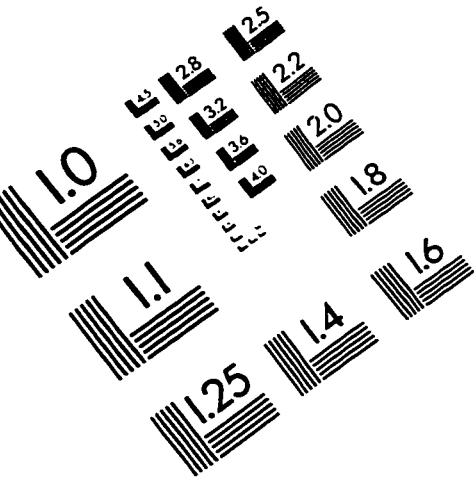
EXAMINING COMMITTEE:



Date of Examination:

9 April 1998

IMAGE EVALUATION TEST TARGET (QA-3)



APPLIED IMAGE, Inc
 1653 East Main Street
 Rochester, NY 14609 USA
 Phone: 716/482-0300
 Fax: 716/288-5989

© 1993, Applied Image, Inc., All Rights Reserved